

2014

Analytical Study of the Responses of Bottom Panels under Slamming Loads and Steel/Composite Hybrid Slamming Test Boat

Jian Lv
Lehigh University

Follow this and additional works at: <http://preserve.lehigh.edu/etd>



Part of the [Mechanical Engineering Commons](#)

Recommended Citation

Lv, Jian, "Analytical Study of the Responses of Bottom Panels under Slamming Loads and Steel/Composite Hybrid Slamming Test Boat" (2014). *Theses and Dissertations*. Paper 1549.

This Dissertation is brought to you for free and open access by Lehigh Preserve. It has been accepted for inclusion in Theses and Dissertations by an authorized administrator of Lehigh Preserve. For more information, please contact preserve@lehigh.edu.

**Analytical Study of the Responses of Bottom Panels
under Slamming Loads
and
Steel/Composite Hybrid Slamming Test Boat**

By
Jian Lv

Presented to the Graduate and Research Committee
of Lehigh University
in Candidacy for the Degree of
Doctor of Philosophy

In
Mechanical Engineering

Lehigh University

May, 2014

Approved and recommended for acceptance as a dissertation in partial fulfillment of the requirements for the degree of Doctor of Philosophy.

Date

Dissertation Advisor

Accepted Date

Committee Members:

Dr. Joachim L. Grenestedt, Dissertation Advisor/Committee Chairman
Professor
Department of Mechanical Engineering and Mechanics

Dr. D. Gary Harlow
Professor, Department Chair
Department of Mechanical Engineering and Mechanics

Dr. Herman F. Nied
Professor
Department of Mechanical Engineering and Mechanics

Dr. Shamim N. Pakzad
Assistant Professor
Department of Civil Engineering

Acknowledgements

I would like to express my appreciation to the faculty and staff of the Department of Mechanical Engineering and Mechanics. The faculty members have given me the tools with which to pursue my career in engineering. I would also like to thank the staff in our department office, and all those who have offered me kind help during my study and living in Lehigh University.

My deepest appreciation goes to Professor Joachim Grenestedt, my Ph.D. advisor, for introducing me to the field of my PhD study. None of my accomplishments could ever be made without his supports, inspiration and guidance during my years at Lehigh.

I would like to thank Professor Tulga M. Ozsoy who kindly offered me the teaching assistant opportunities and important financial supports for three semesters and I would also like to thank Professor Philip A. Blythe for his thoughtful discussion, insightful comments and suggestions.

I also owe thanks to all my PhD committee members: Dr. D. Gary Harlow, Dr. Herman F. Nied and Dr. Shamim N. Pakzad who gave me guidance and direction throughout my quest to obtain my PhD degree.

I have been immensely fortunate to be able to work with a group of great people. I am especially in debt to Mr. Willian Maroun for being always helpful on my research and my life in Lehigh. Many thanks to Dr. Jack Reany for his kind help when I first joined Lehigh Composites Lab. I also owe my gratitude to my colleagues Dr. Andrew Truxel, Robert Thodal and Jacob Patterson who often treat me with very tasty BBQ and nice beer.

Also, I would like to thank all my good friends I met in the U.S. including: Dr. Qian He, Dr. Wenyu Shi, Dr. Weihuan Zhao, Dr. Qian Wu, Dr. Zhiyang Yu, Dr. Guangyong Liu, Dr. Xin Zong, Dr. Hao Tian, Mr. Yibo Wang, Mr. Tianyi Luo, Mr. Fei Wang, Mr. Xiang Song, Mr. Xiao Liu, Mr. Peter Park, Mr. Feng Shi, Miss Baiou Shi, Miss Hankai Zhu, Miss Jie Yuan, Miss Yue Liu, Miss Zhiye Li, Miss Lihua Jiao, Miss Yilin Chen etc.

Most of all, I am extremely thankful to my beloved family, my parents and in laws. Specially, I feel deeply indebted to my wife Jia Guo and my son Yifeng Lv. Without their unconditional love, inexhaustible support and encouragement throughout the past five years, I could never go this far.

Table of contents

Abstract	1
Introduction.....	3
Chapter 1. Analytical Study of the Responses of Bottom Panels under Slamming Loads during the Initial Phase	9
1.1 Introduction	11
1.2 Simplified Analytical Model of Slamming, Two-Step Load on Beam	13
1.3 Nondimensionalization of the Problem	17
1.4 Solutions to the Equations	19
1.5 Alternative Pressure Distribution, the Point-Step Load	22
1.6 Convergence and Error Analysis	24
1.7 Range of Parameters for Slamming.....	26
1.8 Results and Discussion	28
1.9 Conclusions	39
Chapter 2. Analytical Study of the Responses of Bottom Panels to Slamming Loads during Two Phases.....	41
2.1 Introduction	42
2.2 Simplified Analytical Model of Slamming, Two-Step Load on Beam	46
2.2.1 Slamming Load Initial phase.....	48
2.2.2 Nondimensionalization of the Problem	50

2.2.3 Solutions for the Slamming Load Initial phase	50
2.2.4 Transverse Free Vibration Phase	52
2.3 Alternative Pressure Distribution, the Point-Step Load	56
2.4 Range of Parameters for Slamming	58
2.5 Results and Discussion	60
2.6 Conclusions	79
2.7 Acknowledgements	81

Chapter 3. Steel/Composite Hybrid Slamming Test Boat

Manufacturing	82
3.1 Introduction	82
3.2 Composite Panels Manufacturing	87
3.2.1 Constructions of Side Panels and Top Deck Panels	87
3.2.2 Bottom Construction	91
3.2.3 Bulkhead Panel Analysis, Design and Construction	96
3.3 Composite Panel Bonding	99

Chapter 4. Steel/Composite Hybrid Boat Test

4.1 Introduction	104
4.2 Instrumented Slamming Load Test Facility	107
4.3 Bottom Construction	109
4.4 Instrumentation and Data Acquisition	114
4.5 Experimental Methodology	117
4.6 Data Analysis	121

4.7 Results and Discussions	126
4.8 Conclusion.....	156
4.9 Acknowledgement.....	158
Chapter 5. Conclusions and Future Work.....	159
5.1 Contributions of the Dissertation.....	159
5.2 Future Work.....	161
Appendix.....	163
Appendix A	163
Appendix B.....	164
Appendix C.....	165
Appendix D	168
Appendix E.....	172
Bibliography.....	174
Vita	178

Abstract

This dissertation consists of three parts - analytical modeling of slamming on a simplified bottom structure (Papers 1-2), manufacturing of sandwich panels and installing them on the Numerette high-speed offshore research boat, and experimental evaluation of slamming using the Numerette (Paper 3). In the first part, the responses of boat hull bottom panels under slamming loads are studied analytically using a linear elastic Euler-Bernoulli beam as a representation of the cross section of a bottom panel. The slamming pressure is modeled as a high-intensity peak followed by a lower constant pressure, traveling at constant speed along the beam. The problem is solved using a Fourier sine integral transformation in space and a Laplace-Carson integral transformation in time. The response of the beam is solved analytically. Deflection and bending moment as functions of time and position for different slamming speeds, bending stiffnesses, etc. are given. The response during both the initial structural inertia phase and the subsequent free vibration phase are studied and compared. In particular the effect of slamming load traveling speed on structural response of the simplified bottom structure is investigated. It is found that rather large deflections and bending moments are encountered at certain speeds of the pressure, which suggests that bottom panels may benefit from tailoring their stiffness and mass properties such that loads are reduced. The importance of the high-intensity pressure peak often encountered during slamming is also studied.

In the second part some analysis of the structure plus manufacturing of sandwich panels for the Numerette craft is outlined.

In the third part, experimentally obtained data from slamming on the bottom of the Numerette is studied. By combining traditional steel with modern composite materials, a creative steel/composite hybrid ship structure concept is developed and adopted in the design and manufacturing of the test boat. This slamming load test facility is also an attempt to shed some light on a new concept of building high-speed crafts with hybrid ship structures. With this new concept, the high-speed craft could be superior in certain aspects to traditional steel ship designs. The eventual goal is to develop the technology required to build a destroyer size ship using the steel/composite hybrid concept.

Sea trials of the steel/composite hybrid boat were performed to evaluate the structural design of the steel/composite hybrid hull concept, as well as to investigate the response of bottom structures of high speed craft under slamming loads. A considerable amount of valuable data was collected with the onboard data acquisition system. Preliminary data analysis was accomplished. Typical strain and acceleration signals of bottom panels under real slamming loads were identified.

Finally the conclusions and future work are briefly summarized in the last chapter of this dissertation.

Introduction

Slamming, the impact between a hull structure and the water is a challenging problem considered for the structural design of the high-speed crafts. In rough seas, the marine craft may occasionally emerge from a wave and re-enter the wave with a heavy impact or slam as the hull structure comes in contact with the water. Some high-speed craft bottom slamming events are demonstrated in Figure 1.



Figure 1: Demonstration of high-speed craft slamming events

The craft with such excessive motions is subject to very rapidly developed hydrodynamic loads. The loading is dependent on sea-state, direction and speed of craft in relation to sea, as well as on the size and geometry of the craft bottom. These impact loads are of a transient nature. They can be defined as a severe impulsive hydrodynamic load with a short time constant relative to the periods associated with craft motions. A typical bottom slamming on a V-shaped bottom of high-speed crafts is illustrated in Figure 2 and a photo taken during drop tests of a wedge-formed cross section is given in Figure 3.

Typically, a bottom slamming event on a V-shaped hull starts with a high-intensity pressure peak and is followed by a lower and essentially constant residual pressure. This pressure distribution, $q(x,t)$, travels rapidly over the bottom from the keel towards the chine. The pressure peak magnitude and propagation speed critically depend on the impact velocity, V , and deadrise angle of the impacting body, β . Slamming pressures have been experimentally recorded to reach 8 MPa (e.g., Faltinsen[1]), but higher pressure are possible. The slamming event may excite the lower structural modes of the hull girder and abruptly change the vessel's rigid-body motion (Lewis et al [2]). Slammings also affect passengers, equipment and not least the craft itself. Severe slammings even cause damages to the hull (Yamamoto et al. [3]).

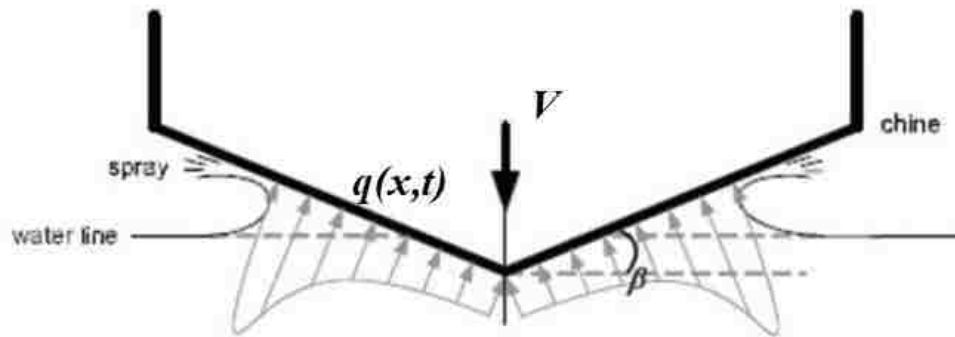


Figure 2: Schematic illustration of idealized V-shaped hull impact illustrating slamming pressure distribution ($q(x,t)$), impact velocity V , deadrise angle β and the spray of water.

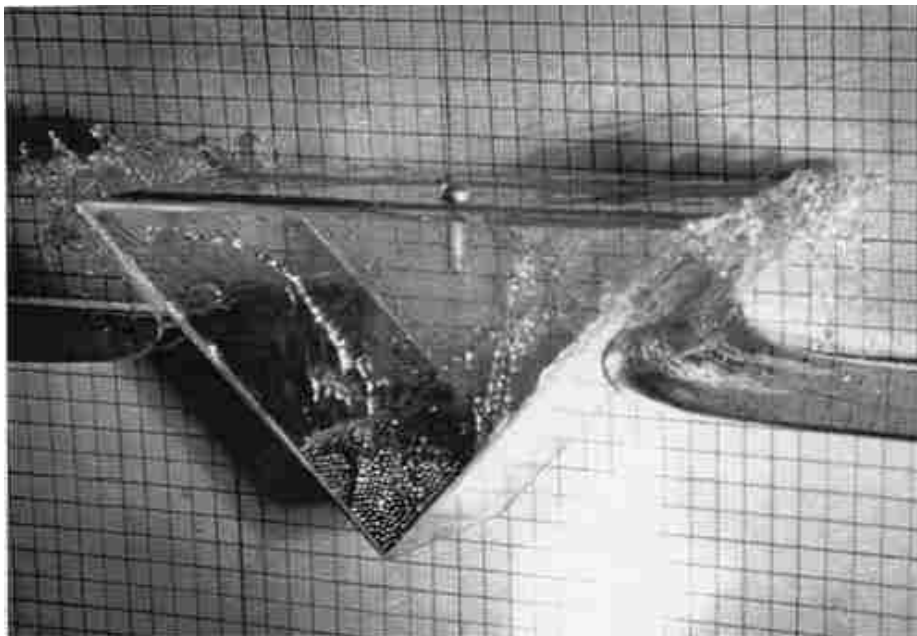


Figure 3: Drop test of a wedge (Adapted from Greenhow and Lin 1983 [4]).

Slamming is a complex event with many effects and mechanisms, including non-stationary flow, compressibility, inertia effects, air cushions and air entrapment, vibration induced cavitation and ventilation, etc. When local loads become very high or the structure is flexible, hydroelastic effects may also be important; the hull structure deforms in response to the slamming load, and the flow field is affected by this deformation. The hydroelastic effects associated with flow about an impacting body usually are highly non-linear. The effects mentioned above may combine and be coupled, depending on the structure and the particular slamming event. Much effort, both experimental and theoretical, has been devoted to showing some of the complexities of slamming and developing tools to interpret this complex phenomenon, including [5-18].

Designing high-speed craft is a challenging task. The designers have to consider extreme loads, fatigue, operability etc., and at the same time minimize structural weight in order to lower craft's operational cost and improve its performance. On the other hand, today's high-speed craft designs strongly rely upon semi-empirical design methods provided by DNV [19], ABS [20], Lloyds [21] or other classification societies, where slamming in essence is considered equivalent with a static uniformly distributed pressure on the bottom. The design pressures are considerably lower than experimentally measured peak pressures. Albeit simple to use, these semi-empirical design methods may be at the cost of accuracy, structural efficiency or even risk of damage. It is desirable to develop more refined and rational design methods which can accurately judge and predict the structural responses under non-uniform hydrodynamic

slamming loads. One component of this dissertation is the development of analytic models.

Von Karman [9] was a pioneering researcher in the field of bottom slamming. He developed an analytic model based on a momentum approach when studying seaplane water landings. His work was followed by many others. Wagner [10] studied two-dimensional water impact on solid bodies. His work was based on potential flow theory. Dobrovol'skaya [11] proposed an analytical method for a wedge entering water vertically at a constant speed, known as the similarity solution. More recently, Zhao and Faltinsen [12, 13] used a boundary element method and indicated a superposition of asymptotic expansions of high pressure at the spray root and a following lower pressure distribution. Faltinsen [13, 14] reported that hydroelastic effects are mainly relevant for local impacts when the deadrise angle is small and the duration of the impact is shorter or comparable to the structure's natural period. A conformal mapping technique was used by Mei et al. [15] to study the impact pressure on a two-dimensional body. Lu, He and Wu [16] developed a method for analyzing hydroelastic interaction between a structure and water by solving coupled equations with the boundary element method and the finite element method. Wet deck slamming was studied theoretically by Faltinsen [17] and Kvalsvold [18] using beam models. An initial structural inertia phase and a subsequent free vibration phase were identified. An asymptotic theory showed that the maximum bending stresses are proportional to an effective drop velocity but are not sensitive to the curvature of the wave surface or where waves hit the beam.

In general, a slamming event appears to consist of an initial slamming load arriving phase followed by a vibration phase. The real slamming on the bottom of a high speed craft running in rough seas is a highly random event. The angle between the bottom and the water surface as well as the impact velocity varies every second. Understanding the bottom response under various conditions is thus important. **The First Two Chapters** in this dissertation are focused on the attempts to shed some light on this complex V-shaped bottom slamming problem by analytically studying a simplified model of a bottom panel subjected to a non-uniform pressure distribution traveling at various speeds across the bottom. **The Third Chapter** introduces a slamming load test facility, Numerette, which is designed and manufactured by Professor Joachim L. Grenestedt and colleagues in the composites lab of Lehigh University. It serves as a slamming load test facility to better understand the slamming phenomenon. A new hybrid ship structure concept is also proposed and realized by combining traditional steel manufacturing with modern composite constructions with the goal to develop the technology for lightweight ship hulls which combine the ductility and stiffness of steel, with the weight reduction of composite panels. **The Forth Chapter** details the shakedown and sea trials of this 9m long, 1,900 kg hybrid steel and composite ship in seas. The boat test method and the data acquisition procedure are given in this section. The typical strain gage data under slamming loads detected on different positions of the boat is illustrated and analyzed. **Finally**, the work included in this dissertation is summarized and the contributions of the dissertation are concluded. Future work of this project is also expected in the final chapter.

Chapter 1.

Analytical Study of the Responses of Bottom Panels under Slamming Loads during the Initial Phase

Paper:

*SOME ANALYTICAL RESULTS FOR THE INITIAL PHASE OF BOTTOM
SLAMMING **

Jian Lv, Joachim L. Grenestedt

Abstract: The deformation of boat hull bottom panels during the initial phase of slamming is studied analytically using a linear elastic Euler-Bernoulli beam as a representation of the cross section of a bottom panel. The slamming pressure is modeled as a high-intensity peak followed by a lower constant pressure, traveling at constant speed along the beam. The problem is solved using a Fourier sine integral transformation in space and a Laplace-Carson integral transformation in time. Deflection and bending moment as functions of time and position for different speeds, bending stiffnesses, etc. are given. In particular the effect of slamming load traveling speed on structural response of the simplified bottom structure is investigated. It is found that rather large deflections and bending moments are encountered at certain speeds of the pressure, which suggests that bottom panels may benefit from tailoring

their stiffness and mass properties such that loads are reduced. This would vary with boat particulars and operation (deadrise angle, mass, speed, sea state, etc). The importance of the high-intensity pressure peak often encountered during slamming is also studied. It is seen that for relatively slow moving slamming loads the pressure peak has little influence. However, for faster moving loads its influence can be significant.

Keywords: Bottom slamming; Initial phase; Euler-Bernoulli beam; Two-step load, analytical method

*Published as “Some Analytical Results for the Initial Phase of Bottom Slamming” in
Maine Structures 34(2013) 88-104

1.1 Introduction

Some of the highest loads on high-speed boats are due to bottom slamming. Slamming pressures are very dynamic and vary significantly over the bottom. Typically slamming starts with a high-intensity pressure peak that travels rapidly over the bottom from the keel towards the chines. The pressure peak is usually followed by a lower and essentially constant pressure. The pressure peak magnitude and propagation speed depend heavily on the impact velocity and deadrise angle of the boat. Slamming peak pressures have been experimentally measured to reach 8 MPa or even more (e.g., Faltinsen [1]), which is close to the acoustic pressure (hammer pressure) for the vertical speeds studied. On the other hand current structural design criteria for high-speed craft treat slamming as static uniformly distributed pressures with considerably lower pressure magnitudes (e.g., DNV [19], ABS [20], Lloyds [21]). This raises the question whether the structures designed and manufactured by those criteria are conservative, over or under designed, or just plainly incorrectly designed. The present study tries to shed some light on this complex problem by analytically studying a simplified model of a bottom panel subjected to a non-uniform pressure distribution traveling at various speeds. More advanced studies, as well as correlation with experimentally measured slamming response using the Numerette research craft, are underway.

Early analytic research on slamming was done by von Karman [9] using a momentum approach, and by Wagner [10] using two-dimensional non-viscous incompressible flow. Cointe and Armand [11] studied the problem of an impacting cylinder and considered

nonlinearity of the local jet flow. Zhao and Faltinsen [12] and Faltinsen [13] improved the solution of Wagner using a boundary element method and indicated a superposition of asymptotic expansions of high pressure at the spray root and a following lower pressure distribution. Faltinsen [13, 14] reported that hydroelastic effects are mainly relevant for local impacts when the deadrise angle is small and the duration of the impact is shorter or comparable to the structure's natural period. A conformal mapping technique was used by Mei et al. [15] to study the impact pressure on a two-dimensional body. Wet deck slamming was studied theoretically by Faltinsen [17] using a hydroelastic beam model. An initial structural inertia phase and a subsequent free vibration phase were identified. An asymptotic theory showed that the maximum bending stresses are proportional to an effective drop velocity and are not sensitive to the curvature of the wave surface or where the waves hit the beam.

Simply stated, slamming appears to consist of an initial slamming load arriving phase followed by a vibration phase. In this paper the bottom response during the slamming load arriving phase is analytically studied. The boat bottom is modeled as a one-dimensional linear elastic Euler-Bernoulli beam. The slamming pressure is modeled as a high intensity peak followed by a lower constant pressure, traveling at constant speed along the beam.

Fluid-structure interactions are at this time ignored, or simply included as a constant added-mass term. Air entrapment which may have a large influence at lower deadrise angles is also ignored. The deformation is assumed to be sufficiently small that linear-

elastic beam theory is valid, and that the geometry of the deformed bottom is not significantly different from the undeformed one. The assumption that the load travels at constant speed across the beam in essence implies that the vertical velocity of the boat bottom is constant during the slamming event, which depending on boat particulars (geometry, mass, etc) may or may not be a reasonable assumption. The equations are solved by using a Fourier sine integral transformation in space and a Laplace-Carson integral transformation in time, as done by Fryba [22]. The structural response during the slamming load arriving phase is given. The effect of slamming load traveling speed on structural responses is presented.

1.2 Simplified Analytical Model of Slamming, Two-Step Load on Beam

Consider the system shown in Figure 1-1 in which a bottom panel is modeled as a simply supported Euler-Bernoulli beam subjected to the slamming load $q(x,t)$ which moves with constant velocity c from one end to the other. The model may be reasonably realistic for bottom panels which are long relative to their width, as is common in boat bottoms. Simply supported edges were chosen as a reasonable approximation of the bottom panels of the Numerette research craft. Its bottom consists of ten sandwich panels whose cores taper off and vanish by the edges, resulting in a single skin "collar" along the perimeter of each panel. The thin single skin collar is considerably more compliant in bending than the thick sandwich, thus modeling the edges as simply supported is presumably a decent approximation. It may or may not be a feasible

approximation for the edges of bottom panels in other boats. The deflection of the beam is $w(x,t)$, where x ($0 \leq x \leq L$) is the position within the beam and t ($0 \leq t \leq L/c$) is time. In Figure 1-1, L is the length of the beam and l_1 is the length of the high-intensity pressure peak. The analysis in this paper terminates at $t=L/c$ when the pressure peak reaches the right end of the beam (corresponding to the slamming pressure reaching the chine of the boat).

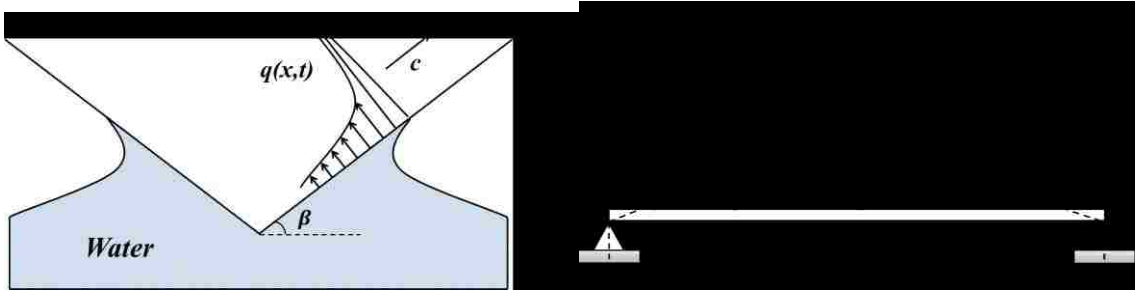


Figure 1-1: Left: cross-section of boat during slamming, showing the moving slamming pressure $q(x,t)$. Right: Simplified model where the bottom panel is represented by a beam and the slamming pressure $q(x,t)$ as two constant pressures, q_1 and q_2 , traveling at a constant speed c .

Using the Euler-Bernoulli beam assumptions the governing equation is

$$EI \frac{\partial^4 w(x,t)}{\partial x^4} + \mu^* \frac{\partial^2 w(x,t)}{\partial t^2} = q(x,t) \quad (1)$$

where EI is bending stiffness (assumed constant), $q(x,t)$ is load per unit length, μ^* is total mass (mass of beam plus some added mass of water) per unit length of the beam (also assumed constant). The added mass of a submerged bottom panel is usually assumed to correspond to the mass of a half cylinder of water with diameter L and

length d (in the present case d is the width of the beam). The total added mass is thus $\rho_w \pi L^2 d / 8$. If it is assumed that this mass is evenly distributed along the length of the present beam, then the added mass per unit length becomes $\rho_w \pi L d / 8$. This would be for a fully submerged panel, whereas at the beginning of the slamming event the bottom panel is essentially dry and there is no added mass term. For this reason a constant $k \in [0,1]$ was introduced, such that $\mu^* = \mu + k \rho_w \pi L d / 8$. For a fully submerged bottom panel $k=1$, whereas for a dry panel $k=0$; however in the analysis below k is assumed constant during the whole slamming event (from the time the keel touches the water surface to the time when the slamming pressure reaches the chine). It may be plausible to believe that the two cases $k=0$ and $k=1$ in some sense bound the behavior of a bottom panel.

In the present study the slamming load is simplified as a moving step load of the following form:

$$q(x,t) = q_1 [1 - H(x - ct)] - (q_1 - q_2) [1 - H(x - c(t - l_1/c))] \quad (2)$$

where q_1 is the load per unit length of the initial load peak, q_2 is the load per unit length of the residual load following the peak, and $H(x)$ is the Heaviside step function,

$$H(x) = \begin{cases} 0 & \text{for } x < 0 \\ 1 & \text{for } x \geq 0 \end{cases} \quad (3)$$

Since equation (1) is linear, superposition applies and the problem can be solved in two parts. The first set of equations is

$$EI \frac{\partial^4 w(x,t)}{\partial x^4} + \mu^* \frac{\partial^2 w(x,t)}{\partial t^2} = q_1 [1 - H(x - ct)] \quad (4)$$

The corresponding boundary conditions and the initial conditions for equation (4) are

$$w(0,t) = 0 \quad w(L,t) = 0 \quad (5)$$

$$\left. \frac{\partial^2 w(x,t)}{\partial x^2} \right|_{x=0} = 0 \quad \left. \frac{\partial^2 w(x,t)}{\partial x^2} \right|_{x=L} = 0$$

and

$$w(x,0) = 0 \quad \left. \frac{\partial w(x,t)}{\partial t} \right|_{t=0} = 0 \quad (6)$$

The second set of equations is

$$EI \frac{\partial^4 w(x,t)}{\partial x^4} + \mu^* \frac{\partial^2 w(x,t)}{\partial t^2} = -(q_1 - q_2) [1 - H(x - c(t - l_1/c))] \quad (7)$$

The corresponding boundary conditions and the initial conditions for equation (7) are

$$w(0,t) = 0 \quad w(L,t) = 0 \quad (8)$$

$$\left. \frac{\partial^2 w(x,t)}{\partial x^2} \right|_{x=0} = 0 \quad \left. \frac{\partial^2 w(x,t)}{\partial x^2} \right|_{x=L} = 0$$

and

$$w(x,t)|_{t=l_1/c} = 0 \quad \left. \frac{\partial w(x,t)}{\partial t} \right|_{t=l_1/c} = 0 \quad (9)$$

If $w(x,t)$ is the solution to the slamming problem, $w_1(x,t)$ is the solution to eqs. (4-6)

and $w_2(x,t)$ is the solution to eqs. (7-9), then

$$w(x,t) = w_1(x,t) + w_2(x,t) \quad (10)$$

1.3 Nondimensionalization of the Problem

In order to reduce the number of parameters the following dimensionless quantities are introduced

$$\begin{aligned} \bar{x} &= \frac{x}{L} & \bar{l}_1 &= \frac{l_1}{L} & \bar{w} &= \frac{w}{L} & \bar{q} &= \frac{L^3}{EI} q & \bar{t} &= t \sqrt{\frac{EI}{\mu^* L^4}} \\ \bar{c} &= c \sqrt{\frac{\mu^* L^2}{EI}} & \bar{M}(\bar{x}, \bar{t}) &= \frac{L}{EI} M(x,t) \end{aligned} \quad (11)$$

The dimensionless versions of eqs. (4-6) are

$$\frac{\partial^4 \bar{w}(\bar{x}, \bar{t})}{\partial \bar{x}^4} + \frac{\partial^2 \bar{w}(\bar{x}, \bar{t})}{\partial \bar{t}^2} = \bar{q}_1 [1 - H(\bar{x} - \bar{c}\bar{t})] \quad (12)$$

$$\bar{w}(0, \bar{t}) = 0 \quad \bar{w}(1, \bar{t}) = 0 \quad (13)$$

$$\left. \frac{\partial^2 \bar{w}(\bar{x}, \bar{t})}{\partial \bar{x}^2} \right|_{\bar{x}=0} = 0 \quad \left. \frac{\partial^2 \bar{w}(\bar{x}, \bar{t})}{\partial \bar{x}^2} \right|_{\bar{x}=1} = 0$$

and

$$\bar{w}(\bar{x}, 0) = 0 \quad \left. \frac{\partial \bar{w}(\bar{x}, \bar{t})}{\partial \bar{t}} \right|_{\bar{t}=0} = 0 \quad (14)$$

while the dimensionless versions of eqs. (7-9) are

$$\frac{\partial^4 \bar{w}(\bar{x}, \bar{t})}{\partial \bar{x}^4} + \frac{\partial^2 \bar{w}(\bar{x}, \bar{t})}{\partial \bar{t}^2} = -(\bar{q}_1 - \bar{q}_2) [1 - H(\bar{x} - \bar{c}(\bar{t} - \bar{l}_1/\bar{c}))] \quad (15)$$

$$\bar{w}(0, \bar{t}) = 0 \quad \bar{w}(1, \bar{t}) = 0 \quad (16)$$

$$\left. \frac{\partial^2 \bar{w}(\bar{x}, \bar{t})}{\partial \bar{x}^2} \right|_{\bar{x}=0} = 0 \quad \left. \frac{\partial^2 \bar{w}(\bar{x}, \bar{t})}{\partial \bar{x}^2} \right|_{\bar{x}=1} = 0$$

and

$$\bar{w}(\bar{x}, \bar{t}) \Big|_{\bar{t}=\bar{l}_1/\bar{c}} = 0 \quad \left. \frac{\partial \bar{w}(\bar{x}, \bar{t})}{\partial \bar{t}} \right|_{\bar{t}=\bar{l}_1/\bar{c}} = 0 \quad (17)$$

1.4 Solutions to the Equations

For equations (12-14), the solution $\bar{w}_1(\bar{x}, \bar{t})$ can be obtained by using a Fourier sine integral transformation in space and a Laplace-Carson integral transformation in time [22]. Multiplying eq. (12) by $\sin j\pi\bar{x}$, where j is an integer, and integrating with respect to \bar{x} between 0 and 1, using the boundary conditions (13) and relations (A1-A3) in Appendix A, the following is obtained:

$$j^4 \pi^4 W(j, \bar{t}) + \ddot{W}(j, \bar{t}) = \frac{\bar{q}_1}{j\pi} (1 - \cos j\pi\bar{c}\bar{t}) \quad j = 1, 2, 3, \dots \quad (18)$$

where $W(j, \bar{t})$ is the Fourier sine integral transform of the original $\bar{w}_1(\bar{x}, \bar{t})$,

$$W(j, \bar{t}) = \int_0^1 \bar{w}_1(\bar{x}, \bar{t}) \sin j\pi\bar{x} d\bar{x} \quad j = 1, 2, 3, \dots \quad (19)$$

$$\bar{w}_1(\bar{x}, \bar{t}) = 2 \sum_{j=1}^{\infty} W(j, \bar{t}) \sin j\pi\bar{x} \quad (20)$$

Set $a = j^2 \pi^2$ and $b = j\pi\bar{c}$, then equation (18) can be reorganized as follows

$$\ddot{W}(j, \bar{t}) + a^2 W(j, \bar{t}) = \frac{\bar{q}_1}{j\pi} (1 - \cos b\bar{t}) \quad j = 1, 2, 3, \dots \quad (21)$$

Next we apply the Laplace-Carson integral transformation on equation (21), i.e. multiply each term in eq. (21) by $e^{-s\bar{t}}$, integrate with respect to \bar{t} between 0 and ∞ , and multiply by s which is a variable in the complex plane. Using the initial conditions (14) and relations (B1-B3) in Appendix B, we can get

$$W^*(j, s) = \frac{\bar{q}_1}{j\pi} \frac{b^2}{(s^2 + a^2)(s^2 + b^2)} \quad (22)$$

where $W^*(j, s)$ is the Laplace-Carson transform of the original $W(j, \bar{t})$,

$$W^*(j, s) = s \int_0^{\infty} W(j, \bar{t}) e^{-s\bar{t}} d\bar{t} \quad (23)$$

Applying the inverse Laplace-Carson transformation on equation (22), using relations (B2) (B4), the solution is obtained,

$$W(j, \bar{t}) = \frac{\bar{q}_1}{j^5 \pi^5} \left[1 + \frac{1}{a^2 - b^2} (b^2 \cos a\bar{t} - a^2 \cos b\bar{t}) \right] \quad (24)$$

This solution is not valid if $a=b$, i.e. when $j = \pi\bar{c}$. However, this can be avoided by a slight change in \bar{c} , and therefore will be tacitly ignored.

With equation (20) and (24), we shall get the solution to eqs. (12-14), where $0 \leq \bar{t} \leq 1/\bar{c}$ and $0 \leq \bar{x} \leq 1$,

$$\bar{w}_1(\bar{x}, \bar{t}) = \frac{2\bar{q}_1}{\pi^5} \sum_{j=1}^{\infty} \frac{1}{j^5} \left[1 + \frac{1}{a^2 - b^2} (b^2 \cos a\bar{t} - a^2 \cos b\bar{t}) \right] \sin j\pi\bar{x}, \quad a = j^2\pi^2, \quad b = j\pi c \quad (25)$$

The solution to the second set of equations, eqs. (15-17), is obtained by a time shift and scaling,

$$\bar{w}_2(\bar{x}, \bar{t}) = \begin{cases} 0 & (0 \leq \bar{t} \leq \frac{\bar{l}_1}{c}) \\ \frac{2(\bar{q}_2 - \bar{q}_1)}{\pi^5} \sum_{j=1}^{\infty} \frac{1}{j^5} \left[1 + \frac{1}{a^2 - b^2} (b^2 \cos a(\bar{t} - \frac{\bar{l}_1}{c}) - a^2 \cos b(\bar{t} - \frac{\bar{l}_1}{c})) \right] \sin j\pi\bar{x} & (\frac{\bar{l}_1}{c} \leq \bar{t} \leq \frac{1}{c}) \end{cases} \quad (26)$$

Thus, the final solution for a moving step load is

$$\bar{w}(\bar{x}, \bar{t}) = \begin{cases} \frac{2\bar{q}_1}{\pi^5} \sum_{j=1}^{\infty} \frac{1}{j^5} \left[1 + \frac{1}{a^2 - b^2} (b^2 \cos a\bar{t} - a^2 \cos b\bar{t}) \right] \sin j\pi\bar{x} & (0 \leq \bar{t} \leq \frac{\bar{l}_1}{c}) \\ \frac{2}{\pi^5} \sum_{j=1}^{\infty} \frac{1}{j^5} \left[\bar{q}_2 + \frac{\bar{q}_1}{a^2 - b^2} (b^2 \cos a\bar{t} - a^2 \cos b\bar{t}) - \frac{\bar{q}_1 - \bar{q}_2}{a^2 - b^2} \left(b^2 \cos a(\bar{t} - \frac{\bar{l}_1}{c}) - a^2 \cos b(\bar{t} - \frac{\bar{l}_1}{c}) \right) \right] \sin j\pi\bar{x} & (\frac{\bar{l}_1}{c} \leq \bar{t} \leq \frac{1}{c}) \end{cases} \quad (27)$$

With the deflection known other quantities of interest, like the bending moment or the shear forces in the beam, are easily obtained. In particular, the bending moment is

$$M = -EI \frac{\partial^2 w(x, t)}{\partial x^2}, \quad \bar{M} = -\frac{\partial^2 \bar{w}(\bar{x}, \bar{t})}{\partial \bar{x}^2} \quad (28)$$

and thus

$$\bar{M}(\bar{x}, \bar{t}) = \begin{cases} \frac{2\bar{q}_1}{\pi^3} \sum_{j=1}^{\infty} \frac{1}{j^3} \left[1 + \frac{1}{a^2 - b^2} (b^2 \cos a\bar{t} - a^2 \cos b\bar{t}) \right] \sin j\pi\bar{x} & (0 \leq \bar{t} \leq \frac{\bar{l}_1}{c}) \\ \frac{2}{\pi^3} \sum_{j=1}^{\infty} \frac{1}{j^3} \left[\bar{q}_2 + \frac{\bar{q}_1}{a^2 - b^2} (b^2 \cos a\bar{t} - a^2 \cos b\bar{t}) \right. \\ \left. - \frac{\bar{q}_1 - \bar{q}_2}{a^2 - b^2} \left(b^2 \cos a(\bar{t} - \frac{\bar{l}_1}{c}) - a^2 \cos b(\bar{t} - \frac{\bar{l}_1}{c}) \right) \right] \sin j\pi\bar{x} & (\frac{\bar{l}_1}{c} \leq \bar{t} \leq \frac{1}{c}) \end{cases} \quad (29)$$

In the next section a slightly different pressure profile will be discussed.

1.5 Alternative Pressure Distribution, the Point-Step Load

As mentioned measurements of bottom pressures in high-speed boats indicate that there is a high pressure peak spreading rapidly over the bottom, followed by a considerably lower pressure over a large area of the bottom. The pressure peak was represented by the pressure (times width) q_1 above. The importance of the pressure peak can be further studied by representing it by a moving point-load, F_D , followed by a constant pressure. This will be called the "Point-Step Load" in the remainder of the paper. The normalized slamming load $\bar{q}(\bar{x}, \bar{t})$ can then be expressed as

$$\bar{q}(\bar{x}, \bar{t}) = \bar{F}_D \delta(\bar{x} - c\bar{t}) + \bar{q}_r [1 - H(\bar{x} - c\bar{t})] \quad (30)$$

where $\delta(x)$ is a Dirac pulse and \bar{q}_r is a residual pressure following the point load. In order to compare this load with the two-step load, the point-load load is set equal to the total load of the initial peak, and the total load when the slamming reaches the right end of the beam is made the same for the two different loads; thus

$$\bar{F}_D = \bar{q}_1 \bar{l}_1 \quad \bar{q}_r = \bar{q}_2 (1 - \bar{l}_1) \quad (31)$$

The governing equation for this load is

$$\frac{\partial^4 \bar{w}_I(\bar{x}, \bar{t})}{\partial \bar{x}^4} + \frac{\partial^2 \bar{w}_I(\bar{x}, \bar{t})}{\partial \bar{t}^2} = \bar{F}_D \delta(\bar{x} - \bar{c}\bar{t}) + \bar{q}_r [1 - H(\bar{x} - \bar{c}\bar{t})] \quad (32)$$

together with the boundary and initial conditions, eqs. (13-14). The problem is solved in a similar fashion as for the two-step load, and with the help of (A4), (B4) and (B5) the solution becomes:

$$\begin{aligned} \bar{w}_I(\bar{x}, \bar{t}) = & 2\pi \bar{F}_D \bar{c} \sum_{j=1}^{\infty} \frac{j}{a^2 - b^2} \left(\frac{1}{b} \sin b\bar{t} - \frac{1}{a} \sin a\bar{t} \right) \sin j\pi\bar{x} \\ & + \frac{2\bar{q}_r}{\pi^5} \sum_{j=1}^{\infty} \frac{1}{j^5} \left[1 + \frac{1}{a^2 - b^2} (b^2 \cos a\bar{t} - a^2 \cos b\bar{t}) \right] \sin j\pi\bar{x} \end{aligned} \quad (33)$$

$$\begin{aligned} \bar{M}_I(\bar{x}, \bar{t}) = & 2\pi^3 \bar{F}_D \bar{c} \sum_{j=1}^{\infty} \frac{j^3}{a^2 - b^2} \left(\frac{1}{b} \sin b\bar{t} - \frac{1}{a} \sin a\bar{t} \right) \sin j\pi\bar{x} \\ & + \frac{2\bar{q}_r}{\pi^3} \sum_{j=1}^{\infty} \frac{1}{j^3} \left[1 + \frac{1}{a^2 - b^2} (b^2 \cos a\bar{t} - a^2 \cos b\bar{t}) \right] \sin j\pi\bar{x} \end{aligned} \quad (34)$$

With the definition of the point load and the residual pressure of eq. (31), the total load at the time the slamming reaches the right end of the beam is the same for this load as for the two-step load. However, at any other time the total force is higher for the present pressure distribution.

1.6 Convergence and Error Analysis

In this section the errors introduced by terminating the infinite series solutions of eqs. (27) and (29) are studied. With some rearrangement of eq. (25) the following is obtained,

$$\begin{aligned}
 |\bar{w}_1(\bar{x}, \bar{t})| &\leq \left| \frac{2\bar{q}_1}{\pi^5} \sum_{j=1}^{\infty} \frac{1}{j^5} \right| + \left| \frac{2\bar{q}_1 \bar{c}^{-2}}{\pi^5} \sum_{j=1}^{\infty} \left| \frac{1}{j^5 (j^2 \pi^2 - \bar{c}^{-2})} \right| \right| + \left| \frac{2\bar{q}_1}{\pi^3} \sum_{j=1}^{\infty} \left| \frac{1}{j^3 (j^2 \pi^2 - \bar{c}^{-2})} \right| \right| \\
 &\leq \left| \frac{2\bar{q}_1}{\pi^5} \sum_{j=1}^{J_1-1} \frac{1}{j^5} \right| + \left| \frac{2\bar{q}_1 \bar{c}^{-2}}{\pi^5} \sum_{j=1}^{J_1-1} \left| \frac{1}{j^5 (j^2 \pi^2 - \bar{c}^{-2})} \right| \right| + \left| \frac{2\bar{q}_1}{\pi^3} \sum_{j=1}^{J_1-1} \left| \frac{1}{j^3 (j^2 \pi^2 - \bar{c}^{-2})} \right| \right| \\
 &\quad + \left| \frac{2\bar{q}_1 (1 + \bar{c}^{-2})}{\pi^5} \sum_{j=J_1}^{\infty} \frac{1}{j^5} \right| + \left| \frac{2\bar{q}_1}{\pi^3} \sum_{j=J_1}^{\infty} \frac{1}{j^3} \right|
 \end{aligned} \tag{35}$$

where J_1 is an integer equal or greater than $\sqrt{1 + \bar{c}^{-2}} / \pi$ (so $j^2 \pi^2 - \bar{c}^{-2} \geq 1$). Since a p -series with $p > 1$ is convergent, the solution $\bar{w}_1(\bar{x}, \bar{t})$ is also convergent (except if $j = \pi \bar{c}$, which as mentioned previously is disregarded).

For numerical calculations a truncated series is used,

$$\bar{w}_1^c(\bar{x}, \bar{t}) = \frac{2\bar{q}_1}{\pi^5} \sum_{j=1}^{J_1-1} \frac{1}{j^5} \left[1 + \frac{1}{a^2 - b^2} (b^2 \cos a\bar{t} - a^2 \cos b\bar{t}) \right] \sin j\pi\bar{x} \tag{36}$$

with an error limited by

$$\begin{aligned}
|error|_d &= \left| \frac{2\bar{q}_1}{\pi^5} \sum_{j=J_1}^{\infty} \frac{1}{j^5} \left[1 + \frac{1}{a^2 - b^2} (b^2 \cos a\bar{t} - a^2 \cos b\bar{t}) \right] \sin j\pi\bar{x} \right| \\
&\leq \left| \frac{2\bar{q}_1(1+c^{-2})}{\pi^5} \sum_{j=J_1}^{\infty} \frac{1}{j^5} \right| + \left| \frac{2\bar{q}_1}{\pi^3} \sum_{j=J_1}^{\infty} \frac{1}{j^3} \right|
\end{aligned} \tag{37}$$

Since

$$\sum_{j=J_1}^{\infty} \frac{1}{j^5} < \int_{J_1-1}^{\infty} \frac{1}{x^5} dx = \frac{1}{4(J_1-1)^4} \quad \text{and} \quad \sum_{j=J_1}^{\infty} \frac{1}{j^3} < \int_{J_1-1}^{\infty} \frac{1}{x^3} dx = \frac{1}{2(J_1-1)^2} \tag{38}$$

the error estimate becomes

$$|error|_d < \left| \frac{\bar{q}_1(1+c^{-2})}{2\pi^5(J_1-1)^4} \right| + \left| \frac{\bar{q}_1}{\pi^3(J_1-1)^2} \right| \tag{39}$$

Similarly, for the bending moment $\bar{M}_1 = -\frac{\partial^2 \bar{w}_1(\bar{x}, \bar{t})}{\partial \bar{x}^2}$, we can get the following result

$$\bar{M}_1^c(\bar{x}, \bar{t}) = \frac{2\bar{q}_1}{\pi^3} \sum_{j=1}^{J_2-1} \frac{1}{j^3} \left[1 + \frac{1}{a^2 - b^2} (b^2 \cos a\bar{t} - a^2 \cos b\bar{t}) \right] \sin j\pi\bar{x} \tag{40}$$

where J_2 is an integer equal or greater than $\left(1 + \sqrt{1 + 4\pi^2 c^{-2}}\right) / 2\pi^2$. An upper bound of

the error of the bending moment $\bar{M}_1^c(\bar{x}, \bar{t})$ is

$$|error|_m < \left| \frac{\bar{q}_1}{\pi^3(J_2 - 1)^2} \right| + \left| \frac{2\bar{q}_1\bar{c}^2}{3\pi^3(J_2 - 1)^3} \right| + \left| \frac{2\bar{q}_1}{\pi(J_2 - 1)} \right| \quad (41)$$

1.7 Range of Parameters for Slamming

Slamming calculations will in this paper be performed for parameters that are relevant for boats and ships. The speed that the slamming load travels over the bottom, c , can be estimated by

$$c = \frac{V\pi}{2 \tan \beta} \cdot \frac{1}{\cos \beta} = \frac{V\pi}{2 \sin \beta} \quad (42)$$

where V is the vertical velocity of a 2D wedge dropped in water and β is the deadrise angle of the bottom, e.g., Faltinsen [14]. It will be assumed that deadrise angles of the boats of interest are in the range 5° to 45° , and the vertical velocity in the range 1 m/s to 10 m/s. Drop tests with these parameters have been performed in [1], [6] and [42]. Using these values the speed that the slamming load travels over the bottom, c , is estimated by eq. [42] to vary from 2 m/s to 200 m/s. Peak pressure and duration were deduced from among other sources the drop tests of [1], [14] and [42]. The peak pressure range and peak duration in Table 1-1 appears to cover the majority of such tests. The ratio of q_1/q_2 is naturally not clearly defined from experiments since real slamming loads differs from the two-step load presently assumed. However, for the

purpose of presenting results the pressure ratio q_1/q_2 was assumed to be in the range of 2~20.

Table 1-1 Range of parameters studied

Parameters	Traveling load speed c [m/s]	Peak pressure [kPa]	ratio of q_1/q_2	Duration of slamming load peak [ms]
Value Ranges	2~200	10~8,000	2~20	0.01~2

Table 1-2 Range of interest of the dimensionless parameters

Parameters	Traveling load speed \bar{c}	Peak pressure \bar{q}_1	Ratio of \bar{q}_1 / \bar{q}_2	Peak load length \bar{l}_1
Value Ranges	0.01~320	$10^{-3} \sim 10^5$	2~20	$2 \times 10^{-5} \sim 0.4$

Regarding bottom stiffness, the range can be estimated to vary from that of a very soft bottom panel such as a one meter wide 3 mm thick aluminum plate ($E=70$ GPa, density 2700 kg/m^3), to a stiff bottom such as a one meter wide sandwich panel with two 15 mm thick carbon fiber skins ($E=100$ GPa, density 1500 kg/m^3) on each side of a 70 mm thick high density foam core (negligible stiffness, density 250 kg/m^3). This results in a bending stiffness (EI) ratio of the soft bottom to the stiff bottom of approximately

3×10^{-5} . With this ratio, the ranges of interest of the dimensionless parameters given in Table 1-2 are obtained (from eq. (11)). The length l_1 was estimated as traveling load speed times duration of the pressure peak, resulting in the normalized length \bar{l}_1 of Table 1-2 if the length of the beam is 1 m.

In the next section dynamic deflection \bar{w} and bending moment \bar{M} will be presented. They will be normalized by the maximum static deflection \bar{w}_{ms} and the maximum static bending moment \bar{M}_{ms} that result if the beam is statically subjected to a two-step load with the same properties as the dynamic load (i.e., as in Figure 1-1). Let $\bar{x} = a$ be the right edge of the pressure pulse \bar{q}_1 . Then

$$\bar{w}_{ms} = \max_{0 < a < 1, 0 < x < 1} |\bar{w}_s| \quad \bar{M}_{ms} = \max_{0 < a < 1, 0 < x < 1} |\bar{M}_s| \quad (43)$$

where \bar{w}_s and \bar{M}_s are the normalized static deflection and bending moment, respectively; please see Appendix C for more details.

1.8 Results and Discussion

A sample calculation will reveal some of the features of dynamically loaded bottom panels. Consider a simply supported beam subjected to a moving slamming load with the following parameters: $\bar{c} = 5$, $\bar{q}_1/\bar{q}_2 = 5$, $\bar{l}_1 = 0.01$. The deflections at four instances

($\bar{t} = \frac{1}{4c}, \frac{1}{2c}, \frac{3}{4c}$ and $\frac{1}{c}$) are shown in Figure 1-2, and the bending moments are shown in

Figure 1-3.

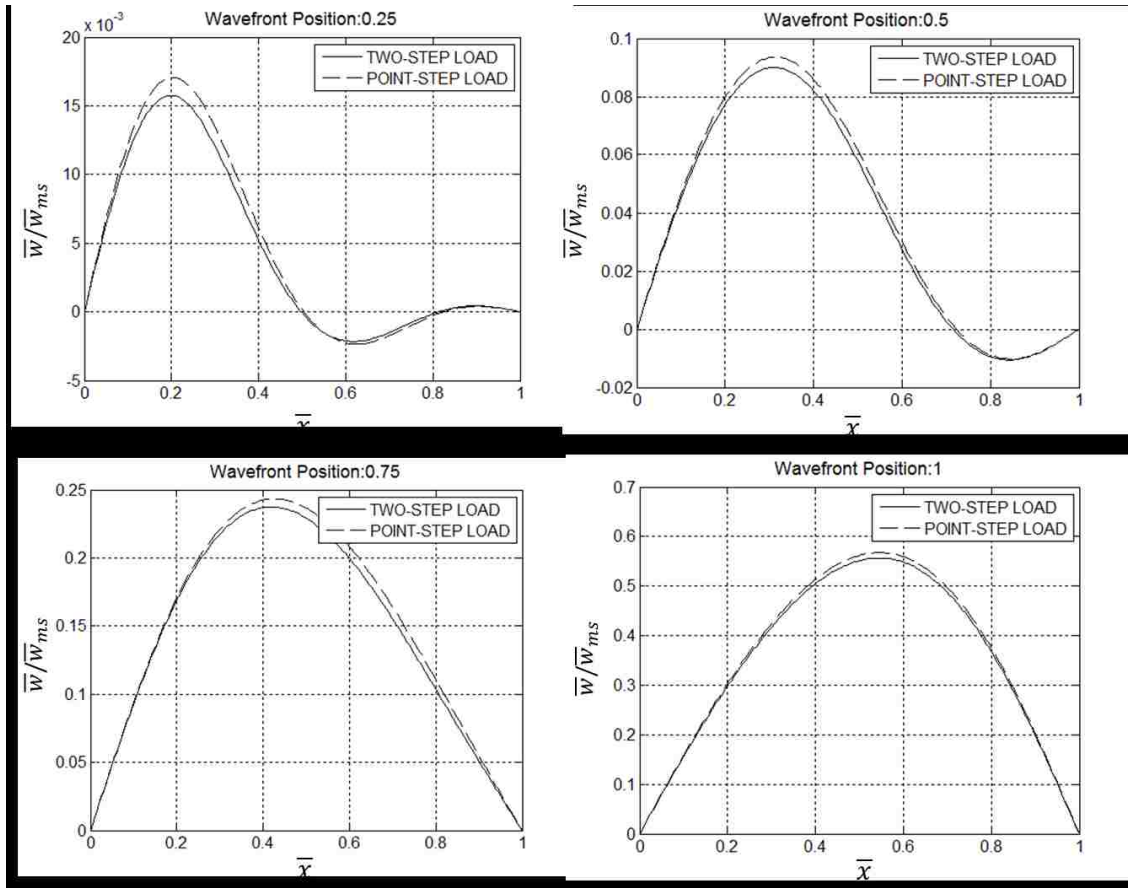


Figure 1-2: Deflection ratio \bar{w}/\bar{w}_{ms} of the beam under moving slamming load with $\bar{c} = 5$, $\bar{q}_1/\bar{q}_2 = 5$, $\bar{l}_1 = 0.01$

The vertical axes represent the deflection ratio \bar{w}/\bar{w}_{ms} and the bending moment ratio \bar{M}/\bar{M}_{ms} , respectively. In this example the Point-Step Load predicts slightly higher deflection and bending moment of the beam in most instances, as would be expected. In this case the maximum deflection reaches approximately 55% of the maximum static

deflection. The fact that the load is moving thus reduced the maximum deflection in this case. This is not generally true as will be seen shortly.

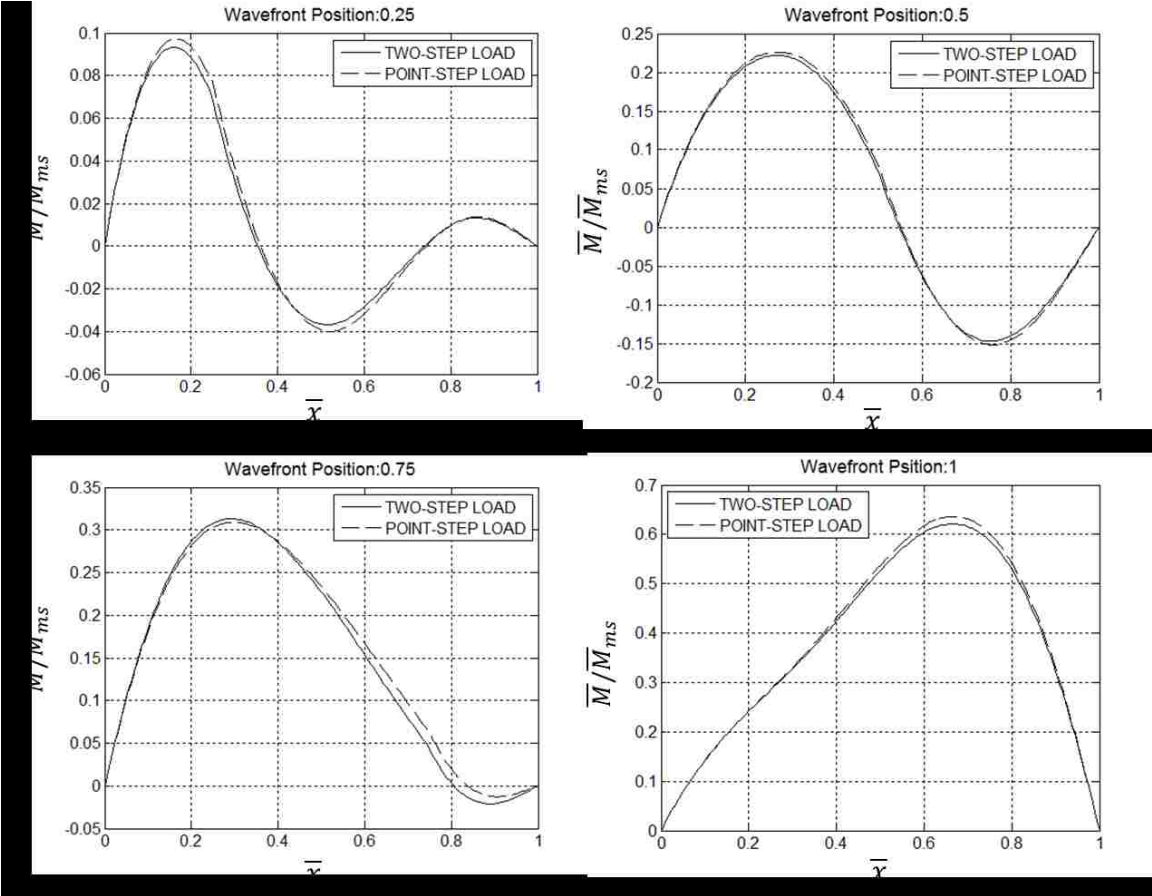


Figure 1-3: Bending moment ratio \bar{M} / \bar{M}_{ms} of the beam under moving slamming load with $\bar{c} = 5$, $\bar{q}_1 / \bar{q}_2 = 5$, $\bar{l}_1 = 0.01$

The effects of the slamming load traveling speed on structural responses are sketched in Figures 1-4 and 1-5 when $\bar{l}_1 = 0.01$. They show the maximum absolute value of the dynamic deflection and bending moment,

$$\bar{w}_{md} = \max_{0 < t < 1/c, 0 < x < 1} |\bar{w}| \quad \bar{M}_{md} = \max_{0 < t < 1/c, 0 < x < 1} |\bar{M}| \quad (44)$$

normalized by the maximum static deflection, \bar{w}_{ms} , and the maximum static bending moment, \bar{M}_{ms} , respectively. Note that \bar{w}_{md} and \bar{M}_{md} depend on \bar{c} , while \bar{w}_{ms} and \bar{M}_{ms} do not. The results in Figures 1-4 and 1-5 demonstrate an important phenomenon of the structural response during the slamming load arriving phase. When the dimensionless slamming load moving speed is relatively low, the maximum dynamic deflection and moment are close to their static counterparts, as expected. However, for the present case with $\bar{l}_1 = 0.01$, when \bar{c} increases to around 2 the maximum dynamic deflection is approximately 50% higher than the maximum static deflection. The same is true for the bending moment, the dynamic bending moment is approximately 50% higher than the static one. There is a form of resonance occurring in the structure. Considerable vibrations are occurring during the slamming load arriving phase when \bar{c} is relatively low. From equations (1) and (8) the eigenfrequencies of a simply supported

Euler-Bernoulli beam can be easily found: $\omega_i = \frac{\pi^2 i^2}{L^2} \sqrt{\frac{EI}{\mu^*}}$, ($i = 1, 2, 3, \dots$). If we define a

characteristic velocity as $c_i = \frac{L\omega_i}{2\pi}$, then the dimensionless characteristic velocity will

be $\bar{c}_i = \frac{\pi i^2}{2}$. The first three dimensionless characteristic velocities are 1.6, 6.3 and 14.1.

The two lower graphs in Figures 1-4 and 1-5 indicate that when $\bar{l}_1 = 0.01$ the most severe structural response occurs when the propagation speed \bar{c} is slightly higher than

the first characteristic velocity. Faltinsen [11] also pointed out that maximum strains occur during the free vibration phase and mainly the lowest eigenmode is of importance at the time scale when maximum strains occur.

Presumably due to inertia effects, at higher propagation speed \bar{c} the maximum deflection and bending moment, \bar{w}_{md} and \bar{M}_{md} , decrease rapidly. When \bar{c} is larger than the third characteristic velocity, 14.1, the maximum structure response ratios, $\bar{w}_{md} / \bar{w}_{ms}$ and $\bar{M}_{md} / \bar{M}_{ms}$, are rather small. This is referred to as the inertia phase by Faltinsen [11], and implies that the slamming force is essentially balanced by structural inertia forces. After the inertia phase, the structure starts to vibrate with an initial velocity obtained at the end of the inertia phase. For \bar{c} larger than 40, the maximum dynamic deflection and bending moment at the end of the slamming load arriving phase is less than 10% of the corresponding maximum static values.

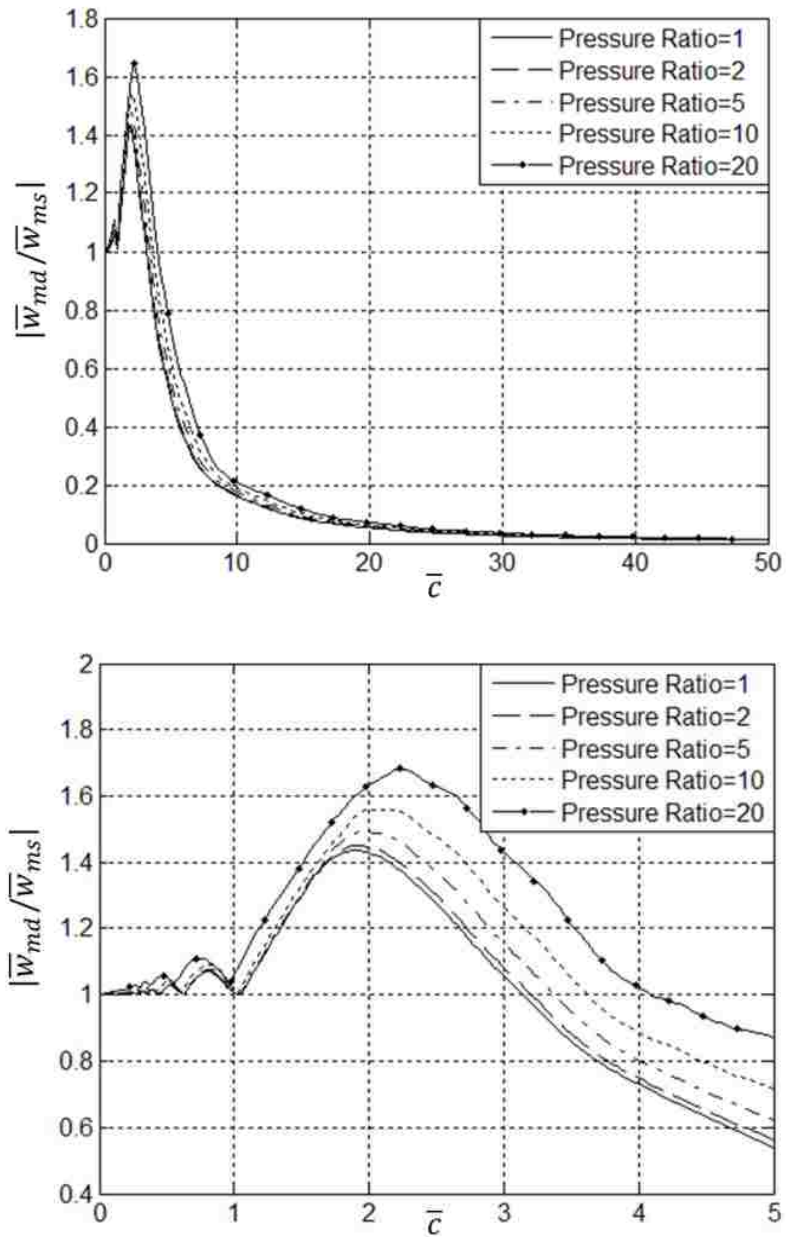


Figure 1-4: Maximum deflection ratio versus speed of the slamming load for five different pressure ratios \bar{q}_1/\bar{q}_2 when $\bar{l}_1 = 0.01$. The lower graph is a zoomed-in version of the upper graph.

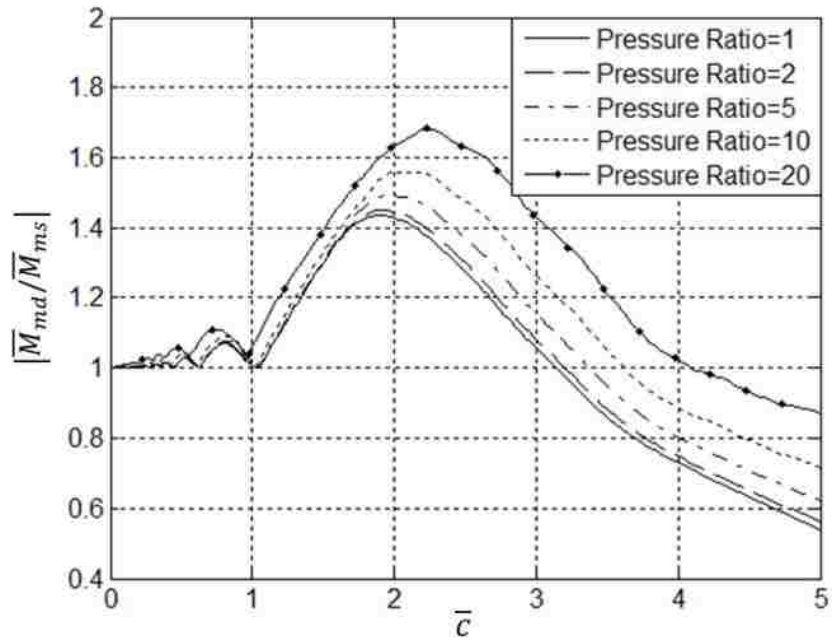
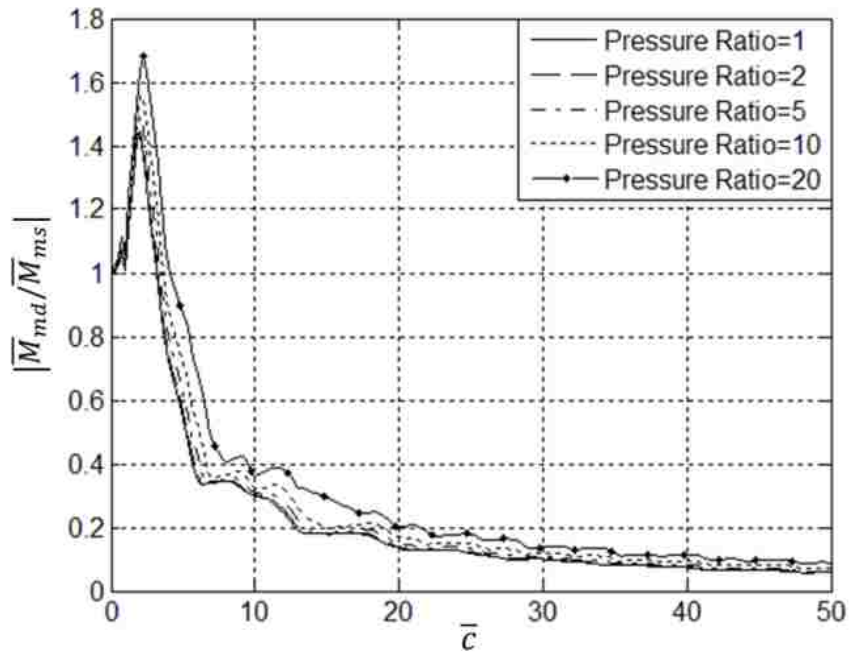


Figure 1-5: Maximum bending moment ratio versus speed of the slamming load for five different pressure ratios $\overline{q}_1/\overline{q}_2$ when $\overline{l}_1 = 0.01$. The lower graph is a zoomed-in version of the upper graph.

Some effect of varying the peak pressure ratio, \bar{q}_1/\bar{q}_2 , is also illustrated in Figures 1-4 and 1-5. With $\bar{l}_1 = 0.01$, increasing the pressure ratio from 1 to 20 leads to higher deflection and bending moment ratios, $\bar{w}_{md}/\bar{w}_{ms}$ and $\bar{M}_{md}/\bar{M}_{ms}$. In other words, a slamming load with the same peak pressure but higher pressure ratio will result in a more severe structural response compared with the corresponding static response.

An effect of peak load length, \bar{l}_1 , is shown in Figures 1-6 and 1-7 for $\bar{q}_1/\bar{q}_2 = 5$. Three different \bar{l}_1 were used, 0.001, 0.01 and 0.1. The deflections and bending moments were normalized by their static equivalents as before in this paper. The figures indicate that both the normalized maximum deflection and dynamic bending moment increase with increasing peak load length, \bar{l}_1 . Hence, slamming load with long duration of the peak pressure appears to generate more deflection and bending moment compared with the static equivalents.

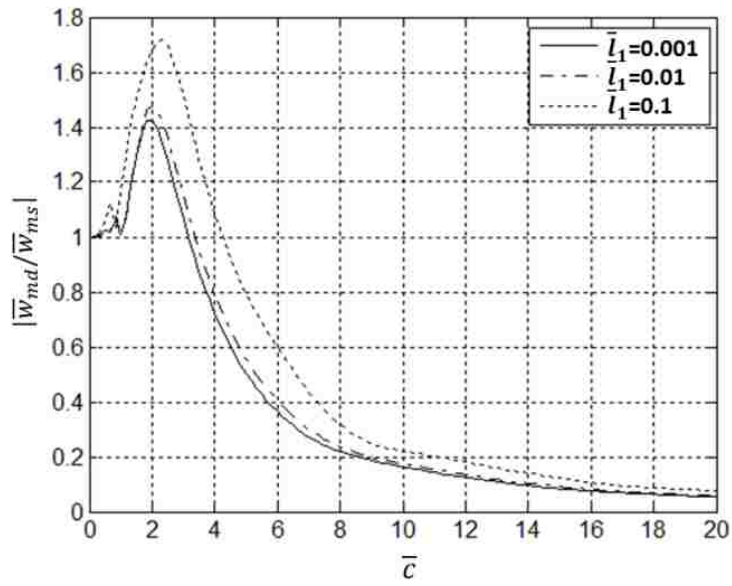


Figure 1-6: Maximum deflection ratio versus speed of the slamming load for three different \bar{l}_1 , when $\bar{q}_1/\bar{q}_2 = 5$

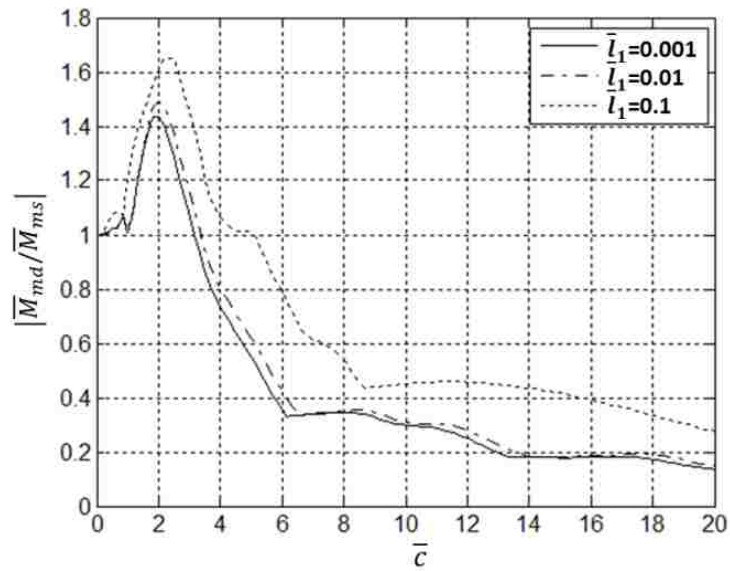


Figure 1-7: Maximum bending moment ratio versus speed of the slamming load for three different \bar{l}_1 , when $\bar{q}_1/\bar{q}_2 = 5$

Some further insight into slamming can be gained by studying the influence of the total force of the initial peak pressure. The Point-Step load outlined previously was used for this purpose, i.e., a point load F_D preceding a constant pressure q_r . The maximum dynamic deflection and the maximum dynamic bending moment were calculated for different point loads F_D . In this case the deflection was normalized by the static deflection of a beam loaded by a distributed pressure q_r only, i.e., by $\bar{w}_s = \left| 5\bar{q}_r / 384 \right|$. Likewise, the dynamic bending moment was normalized by $\bar{M}_s = \left| \bar{q}_r / 8 \right|$. The results are presented in Figures 1-8 and 1-9 where deflection and bending moment are plotted versus $F_D / q_r L$.

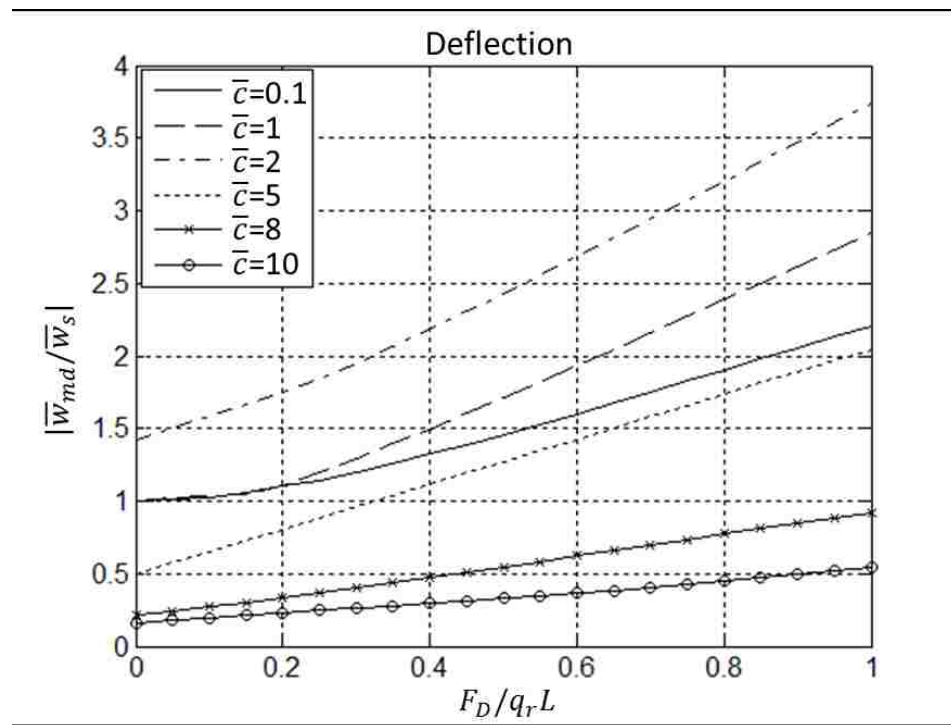


Figure 1-8: Maximum deflection versus point force ratio, normalized by maximum deflection from static evenly distributed load

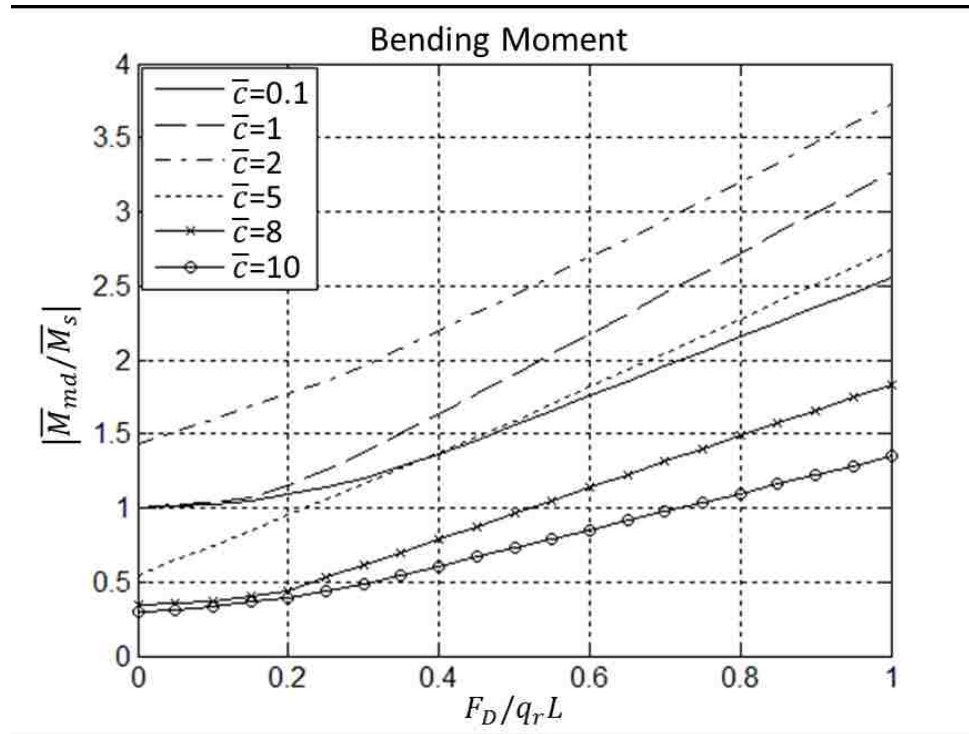


Figure 1-9: Maximum bending moment versus point force ratio, normalized by maximum moment from static evenly distributed load q_r .

Figure 1-8 and 1-9 show that the maximum deflection and bending moment of the structure increase monotonously with increasing point force ratio, $F_D/q_r L$, as expected. Further, as previously seen when \bar{c} is close to the first characteristic velocity, 1.6, the maximum deflection and the maximum bending moment of the structure are the largest. After this high deflection and high bending moment phase, \bar{w}_{md} and \bar{M}_{md} decrease with increasing speed of the slamming load. Further, the figures indicate that reasonably small point loads have only little effect on the structural response when the slamming load travels slowly. For example, the increase in deflection and bending moment is just a few percent (relative to \bar{w}_s and \bar{M}_s) for $F_D/q_r L = 0.1$ and $\bar{c} = 0.1$ or

$\bar{c} = 1$. However, at higher speeds, such as $\bar{c} = 2$ or $\bar{c} = 5$, the increase is quite considerable. For $\bar{c} = 2$ the increase in deflection and bending moment over \bar{w}_s and \bar{M}_s is approximately 12 % while for $\bar{c} = 5$ the deflection increased 31% and the bending moment 38% in spite of the fact that the total load is only 10 % higher because of the point load.

1.9 Conclusions

The initial phase of slamming was studied using a simplified beam model subjected to moving loads. At slow speed of the moving load the maximum dynamic deflection and the maximum dynamic bending moment do not differ much from their static counterparts, but when the speed approaches a characteristic speed of the panel the maximum deflection and bending moment increase on the order of 50 % . At speeds above a few times the characteristic speed, the maximum deflection and bending moment decrease below the static values (during the initial phase under study). Both keep decreasing monotonically as the speed increases. This suggests that bottom panels could be tailored to avoid large deflections and bending moments. In particular panel stiffnesses could be avoided for which the characteristic speed of the panel is near the propagation speed of the slamming load. Granted, this may be difficult, or even impossible, to achieve for any speed and any sea state for a particular boat. Nevertheless, it may be possible to design a boat's bottom such that the effects of the most severe condition (speed, sea state) are reduced. It should further be noted that the

speed and the pressure of the moving load depend on deadrise angle of the hull; for example reducing the deadrise angle would increase the speed of the slamming load (which may be beneficial) but also the pressure (which would not be beneficial). More analyzes using more refined models would be required to gain a better understanding of the potential of tailoring bottom panels for slamming.

The leading edge of the slamming pressure is typically characterized by a high pressure peak. If the force in this peak is on the order of 10% of the total force on the bottom panel, then at slow slamming load propagation speeds (less than, say, half the characteristic speed of the panel) this pressure peak does not increase maximum deflection or maximum bending moment significantly. However, at higher speeds (on the order of three times the characteristic speed) the maximum deflection and maximum bending moment increase 30-40% due to this pressure peak (compared to the response from a static evenly distributed load with no pressure peak), which is very significant.

Chapter 2.

Analytical Study of the Responses of Bottom Panels to Slamming Loads during Two Phases

*Paper: Analytical Study of the Response of Bottom Panels to Slamming loads **

Jian Lv, Joachim L. Grenestedt*

*Submitted to *Ocean Engineering*

Abstract: The responses of boat hull bottom panels under slamming loads are studied analytically using a linear elastic Euler-Bernoulli beam as a representation of the cross section of a bottom panel. The slamming pressure is modeled as a high-intensity peak followed by a lower constant pressure, traveling at constant speed along the beam. The slamming response essentially consists of an initial slamming load arriving phase, followed by a vibration phase. The response of the beam is solved analytically. Deflection and bending moment as functions of time and position for different slamming speeds, bending stiffnesses, etc. are given. The response during the two phases are studied and compared. The maximum deflection and bending moment occur approximately when the time it takes for the slamming load to traverse the beam is comparable to the lowest natural period of the beam. At higher slamming speeds the response is less, and the responses do not peak out until after the slam has traversed the beam (i.e., it occurs during the vibration phase). The importance of the leading high-

intensity pressure peak often encountered during slamming is also studied. It is seen that a high peak pressure does not necessarily lead to a large structural response, whereas the total load of the peak of the slam does influence the structural significantly. For relatively slow moving slamming loads, this influence is limited. However, for faster moving loads it can be substantial.

Keywords: Bottom slamming; Analytical method; Euler-Bernoulli beam; Structural response; Effects of slamming load traveling speed; Vibration Phase

2.1 Introduction

The slamming between water and the bottom structure of a ship may induce critical loads or even structural damage. Slamming pressures have been experimentally measured to reach 8 MPa or even more (e.g., Faltinsen[1]). Typically, a slamming event starts with a high-intensity pressure peak and is followed by a lower and essentially constant residual pressure. This pressure distribution travels rapidly over the bottom from the keel towards the chine. The pressure peak magnitude and propagation speed critically depend on the impact velocity and deadrise angle of the impacting body. When local loads become very high or the structure is flexible, hydroelastic effects may also be important; the hull structure deforms in response to the slamming load, and the flow field is affected by this deformation.

Slamming is a complex phenomenon with many effects and mechanisms, including non-stationary flow, compressibility, inertia effects, air cushions and air entrapment, vibration induced cavitation and ventilation, etc. These effects may combine and be coupled, depending on the structure and the particular slamming event. A number of experimental studies show some of the complexities of slamming, including [5-8].

On the other hand, today's high-speed craft designs strongly rely upon semi-empirical design methods provided by DNV [19], ABS [20], Lloyds [21] and other classification societies, where slamming in essence is considered equivalent with a static uniformly distributed pressure on the bottom. The design pressures are considerably lower than experimentally measured peak pressures. Albeit simple to use, these semi-empirical design methods may be at the cost of accuracy, structural efficiency or even risk of damage. It is desirable to develop more refined and rational design methods which can accurately judge and predict the structural responses under non-uniform hydrodynamic slamming loads. One component of this work is the development of analytic models.

Von Karman [9] was a pioneering researcher in the field of bottom slamming. He developed an analytic model based on a momentum approach when studying seaplane water landings. His work was followed by many others. Wagner [10] studied two-dimensional water impact on solid bodies. His work was based on potential flow theory. Dobrovol'skaya [11] proposed an analytical method for a wedge entering water vertically at a constant speed, known as the similarity solution. More recently, Zhao and Faltinsen [12,13] used a boundary element method and indicated a superposition of

asymptotic expansions of high pressure at the spray root and a following lower pressure distribution. Faltinsen [13,14] reported that hydroelastic effects are mainly relevant for local impacts when the deadrise angle is small and the duration of the impact is shorter or comparable to the structure's natural period. A conformal mapping technique was used by Mei et al. [15] to study the impact pressure on a two-dimensional body. Lu, He and Wu [16] developed a method for analyzing hydroelastic interaction between a structure and water by solving coupled equations with the boundary element method and the finite element method. Wet deck slamming was studied theoretically by Faltinsen [17] and Kvals vold [18] using beam models. An initial structural inertia phase and a subsequent free vibration phase were identified. An asymptotic theory showed that the maximum bending stresses are proportional to an effective drop velocity but are not sensitive to the curvature of the wave surface or where waves hit the beam.

In general, a slamming event appears to consist of an initial slamming load arriving phase followed by a vibration phase. The real slamming on the bottom of a high speed craft running in rough seas is a highly random event. The angle between the bottom and the water surface as well as the impact velocity vary every second. Understanding the bottom response under various conditions is thus important. This paper is an attempt to shed some light on this complex problem by analytically studying a simplified model of a bottom panel subjected to a non-uniform pressure distribution traveling at various speeds across the bottom.

In this research, the boat bottom is modeled as a one-dimensional linear elastic Euler-Bernoulli beam. The slamming pressure is modeled during the initial phase as a high intensity peak followed by a lower constant pressure, traveling at constant speed along the beam. When this load reaches the end (chine) of the beam, all load is removed. The beam then continues its deformation as free vibration. The assumption that the load travels at constant speed across the beam in essence implies that the vertical velocity of the boat bottom is constant during the slamming event. Fluid-structure interactions are ignored in this paper, but an added mass term is included in an approximate manner.

The calculations will in the near future be compared to experimental measurements from the Numerette research craft. Since the composite sandwich bottom panels of the Numerette are quite stiff, it appears reasonable to assume that linear-elastic beam theory is valid and that the geometry of the deformed bottom is not significantly different from the undeformed one. Stenius's [40] experimental results indicate that the influence of geometrical nonlinearities on the center deflection is small for stiff glass fiber / foam core sandwich panels.

For the present calculations, inertia effect of the water is simply included as a constant added-mass term. Air entrapment which may have a large influence at lower deadrise angles is ignored. It is assumed that the slamming event consists of an initial slamming load arriving phase followed by a vibration phase. The initial phase was analyzed analytically in a previous paper [41]. The equations for the initial phase were solved using a Fourier sine integral transformation in space and a Laplace-Carson integral

transformation in time, as done by Fryba [22]. In the present paper the response during the vibration phase, when loads on the beam are neglected, is obtained by solving an eigenvalue problem using separation of variables. The structural response during the vibration phase is presented and compared with the response during the initial phase. Multiple figures show the effect of the slamming load traveling speed on structural response, as well as the effect of the high-intensity pressure peak typical encountered during slamming.

2.2 Simplified Analytical Model of Slamming, Two-Step Load on Beam

The wedge-shaped bottom section of the vessel is partially modeled as a flexible simply supported Euler-Bernoulli beam. Since the lower vibration modes are typically dominant [1], it is most likely sufficient to consider only pure bending of the beam (Euler-Bernoulli kinematics), ignoring shear deformation and rotary inertia (Timoshenko kinematics). Simply supported edges were chosen as a reasonable approximation of the bottom panels of the Numerette research craft; its bottom consists of ten sandwich panels whose cores taper off and vanish by the edges, resulting in a fairly compliant single skin "collar" along the perimeter of each panel. The thin single skin collar is considerably more compliant in bending than the thick sandwich and modeling the edges as simply supported is presumably a decent approximation. Faltinsen [1] also indicated that an Euler beam may be a satisfactory model to investigate the structural response under slamming load. The transient slamming load

$q(x,t)$ is presently modeled as a two-step load with two constant pressures, q_1 and q_2 , which move with constant velocity c from one end to the other (Fig.2-1). The deflection of the beam is $w(x,t)$, where x ($0 \leq x \leq L$) is the position within the beam and t is time. In Figure 2-1, L is the length of the beam and l_1 is the length of the high-intensity pressure peak.

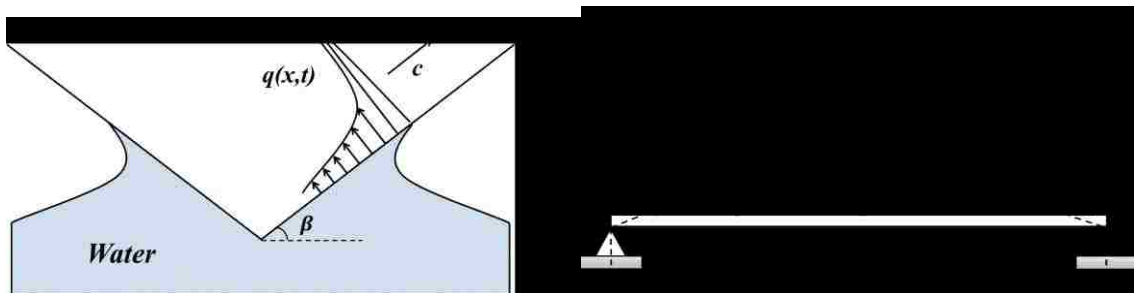


Figure 2-1: Left: cross-section of boat during slamming, showing the moving slamming pressure $q(x,t)$. Right: Simplified model where the bottom panel is represented by a beam and the slamming pressure $q(x,t)$ as two constant pressures, q_1 and q_2 , traveling at a constant speed c .

It is assumed that the slamming event can be separated into two phases: the slamming load initial phase and the subsequent elastic (free) vibration phase. When the speed of the slamming load is high, a large slamming load will cause high acceleration of the bottom during the initial phase but due to the short time that the load is applied it results in only small deflections but potentially significant transverse velocities at the end of this first phase. The time scale may be short relative to the subsequent vibration phase. The behavior in the second phase is vibration with initial conditions obtained from the first phase. It is a periodic event with a characteristic time scale on the order of the longest natural period of the structure. The slamming load initial phase was analyzed in

[41] using two different loads, the "Two-Step Load" and the "Point-Step Load". The deflection and the velocity of the beam at the end of the first phase are briefly reviewed in the following sections. They will be used as the initial conditions for the subsequent vibration phase. By using the method of separation of variables, with the initial conditions in the form of a Fourier sine series, the free vibration problem was solved.

2.2.1 Slamming Load Initial phase

For the slamming load initial phase, the governing equation is [41]

$$EI \frac{\partial^4 w(x,t)}{\partial x^4} + \mu^* \frac{\partial^2 w(x,t)}{\partial t^2} = q(x,t) \quad (45)$$

where EI is bending stiffness (assumed constant), $q(x,t)$ is load per unit length of the beam, μ^* is total mass (mass of beam plus some added mass of water) per unit length of the beam (also assumed constant). The bending stiffness equals Young's modulus E times moment of inertia I for a homogeneous beam, while for non-homogeneous beams the bending stiffness " EI " is an integral over the cross section of the beam. The added mass of a submerged bottom panel is usually assumed to correspond to the mass of a half cylinder of water with diameter L and length d (in the present case d is the width of the beam). The total added mass is thus $\rho_w \pi L^2 d / 8$, where ρ_w is the density of water. If it were assumed that this mass is instead evenly distributed along the length of the present beam, then the added mass per unit length would be $\rho_w \pi L d / 8$. This would be for a fully submerged panel, whereas at the beginning of the slamming event the bottom

panel is essentially dry and there is no added mass from water. For this reason, a constant $k \in [0,1]$ was introduced so that $\mu^* = \mu + k\rho_w \pi L d / 8$. For a fully submerged bottom panel $k=1$, whereas for a dry panel $k=0$; however in the analysis below, k is assumed constant during the whole slamming event (from the time the keel touches the water surface to the time when the water reaches the chine). It may be plausible to believe that the two cases $k=0$ and $k=1$ in some sense bound the behavior of a bottom panel.

The slamming load is simplified as a moving step load of the following form:

$$q(x,t) = q_1[1 - H(x-ct)] - (q_1 - q_2)[1 - H(x-c(t-l_1/c))] \quad (46)$$

where q_1 is the load per unit length of the initial load peak, q_2 is the load per unit length of the residual load following the peak, and H is the Heaviside step function,

$$H(x) = \begin{cases} 0 & \text{for } x < 0 \\ 1 & \text{for } x \geq 0 \end{cases} \quad (47)$$

The corresponding boundary conditions and the initial conditions for equation (45) are

$$w(0,t) = 0 \quad w(L,t) = 0 \quad (48)$$

$$\left. \frac{\partial^2 w(x,t)}{\partial x^2} \right|_{x=0} = 0 \quad \left. \frac{\partial^2 w(x,t)}{\partial x^2} \right|_{x=L} = 0$$

and

$$w(x,0) = 0 \quad \left. \frac{\partial w(x,t)}{\partial t} \right|_{t=0} = 0 \quad (49)$$

2.2.2 Nondimensionalization of the Problem

In order to reduce the number of parameters the following dimensionless quantities are introduced

$$\begin{aligned} \bar{x} &= \frac{x}{L} & \bar{l}_1 &= \frac{l_1}{L} & \bar{w} &= \frac{w}{L} & \bar{q} &= \frac{L^3}{EI} q & \bar{t} &= t \sqrt{\frac{EI}{\mu^* L^4}} \\ \bar{c} &= c \sqrt{\frac{\mu^* L^2}{EI}} & \bar{M}(\bar{x}, \bar{t}) &= \frac{L}{EI} M(x, t) \end{aligned} \quad (50)$$

The dimensionless versions of eqs. (45-49) are

$$\frac{\partial^4 \bar{w}(\bar{x}, \bar{t})}{\partial \bar{x}^4} + \frac{\partial^2 \bar{w}(\bar{x}, \bar{t})}{\partial \bar{t}^2} = \bar{q}_1 [1 - H(\bar{x} - \bar{c}\bar{t})] - (\bar{q}_1 - \bar{q}_2) [1 - H(\bar{x} - \bar{c}(\bar{t} - \bar{l}_1/\bar{c}))] \quad (51)$$

$$\bar{w}(0, \bar{t}) = 0 \quad \bar{w}(1, \bar{t}) = 0 \quad (52)$$

$$\left. \frac{\partial^2 \bar{w}(\bar{x}, \bar{t})}{\partial \bar{x}^2} \right|_{\bar{x}=0} = 0 \quad \left. \frac{\partial^2 \bar{w}(\bar{x}, \bar{t})}{\partial \bar{x}^2} \right|_{\bar{x}=1} = 0$$

and

$$\left. \bar{w}(\bar{x}, \bar{t}) \right|_{\bar{t}=0} = 0 \quad \left. \frac{\partial \bar{w}(\bar{x}, \bar{t})}{\partial \bar{t}} \right|_{\bar{t}=0} = 0 \quad (53)$$

2.2.3 Solutions for the Slamming Load Initial phase

By using a Fourier sine integral transformation in space and a Laplace-Carson integral transformation in time [22], the analytical solution to the equations (51) (52) (53) can be obtained [41]:

$$\bar{w}(\bar{x}, \bar{t}) = \begin{cases} \frac{2\bar{q}_1}{\pi^5} \sum_{j=1}^{\infty} \frac{1}{j^5} \left[1 + \frac{1}{a^2 - b^2} (b^2 \cos a\bar{t} - a^2 \cos b\bar{t}) \right] \sin(j\pi\bar{x}) & (0 \leq \bar{t} \leq \frac{\bar{l}_1}{c}) \\ \frac{2}{\pi^5} \sum_{j=1}^{\infty} \frac{1}{j^5} \left[\bar{q}_2 + \frac{\bar{q}_1}{a^2 - b^2} (b^2 \cos a\bar{t} - a^2 \cos b\bar{t}) \right. \\ \left. - \frac{\bar{q}_1 - \bar{q}_2}{a^2 - b^2} \left(b^2 \cos a\left(\bar{t} - \frac{\bar{l}_1}{c}\right) - a^2 \cos b\left(\bar{t} - \frac{\bar{l}_1}{c}\right) \right) \right] \sin(j\pi\bar{x}) & (\frac{\bar{l}_1}{c} \leq \bar{t} \leq \frac{1}{c}) \end{cases} \quad (54)$$

where $a = j^2\pi^2$ and $b = j\pi c$. Note that there is a typographical error in the corresponding equation in [41]. The deflection and the transverse velocity of the beam at the end of the slamming load initial phase (at $\bar{t} = \bar{t}_1 = 1/\bar{c}$) are

$$\begin{aligned} \bar{w}_{initial} = & \frac{2}{\pi^5} \sum_{j=1}^{\infty} \frac{1}{j^5} \left[\bar{q}_2 + \frac{\bar{q}_1}{a^2 - b^2} (b^2 \cos a\bar{t}_1 - a^2 \cos b\bar{t}_1) \right. \\ & \left. - \frac{\bar{q}_1 - \bar{q}_2}{a^2 - b^2} \left(b^2 \cos a\left(\bar{t}_1 - \frac{\bar{l}_1}{c}\right) - a^2 \cos b\left(\bar{t}_1 - \frac{\bar{l}_1}{c}\right) \right) \right] \sin(j\pi\bar{x}) \end{aligned} \quad (55)$$

$$\begin{aligned} \bar{v}_{initial} = & \frac{2}{\pi^5} \sum_{j=1}^{\infty} \frac{ab}{j^5} \left[\frac{\bar{q}_1}{a^2 - b^2} (a \cdot \sin b\bar{t}_1 - b \cdot \sin a\bar{t}_1) \right. \\ & \left. - \frac{\bar{q}_1 - \bar{q}_2}{a^2 - b^2} \left(a \cdot \sin b\left(\bar{t}_1 - \frac{\bar{l}_1}{c}\right) - b \cdot \sin a\left(\bar{t}_1 - \frac{\bar{l}_1}{c}\right) \right) \right] \sin(j\pi\bar{x}) \end{aligned} \quad (56)$$

These become the initial conditions for the subsequent transverse free vibration phase.

2.2.4 Transverse Free Vibration Phase

The equation of motion that describes the free transverse vibration of a beam with added mass, ignoring damping, is

$$EI \frac{\partial^4 w(x,t)}{\partial x^4} + \mu^* \frac{\partial^2 w(x,t)}{\partial t^2} = 0 \quad (57)$$

By utilizing Eq. (50), the dimensionless equation is

$$\frac{\partial^4 \bar{w}(\bar{x}, \bar{t})}{\partial \bar{x}^4} + \frac{\partial^2 \bar{w}(\bar{x}, \bar{t})}{\partial \bar{t}^2} = 0 \quad (58)$$

Using the method of separation of variables, a solution can be assumed of the form

$$\bar{w}(\bar{x}, \bar{t}) = \phi(\bar{x})T(\bar{t}) \quad (59)$$

which when entered into Eq.(58) leads to

$$\frac{1}{\phi(\bar{x})} \frac{\partial^4 \phi(\bar{x})}{\partial \bar{x}^4} = -\frac{1}{T(\bar{t})} \frac{\partial^2 T(\bar{t})}{\partial \bar{t}^2} = \omega^2 \quad (60)$$

This is a constant since the left hand is a function of x only and the right hand is a function of t only. If this constant were negative, periodic solutions would not be obtained, but rather the time dependence would be exponentially increasing or

decreasing, neither of which is presently of interest. The constant will thus be positive and is here expressed as ω^2 , where ω is the eigenfrequency. Eq.(50) becomes

$$\frac{d^4 \phi(\bar{x})}{d\bar{x}^4} - \beta^4 \phi(\bar{x}) = 0 \quad (61)$$

$$\frac{d^2 T(\bar{t})}{d\bar{t}^2} + \omega^2 T(\bar{t}) = 0 \quad (62)$$

where $\beta^4 = \omega^2$.

The general solutions of Eqs. (51) and (52) are

$$\phi(\bar{x}) = C_1 \sin(\beta\bar{x}) + C_2 \cos(\beta\bar{x}) + C_3 \sinh(\beta\bar{x}) + C_4 \cosh(\beta\bar{x}) \quad (63)$$

and

$$T(\bar{t}) = C_5 \sin(\omega\bar{t}) + C_6 \cos(\omega\bar{t}) \quad (64)$$

where $C_1 \sim C_6$ are as yet undetermined constants. The homogeneous boundary conditions (52) yield four algebraic equations, with the solution $C_2=C_3=C_4=0$, and the characteristic equation:

$$\sin(\beta) = 0 \quad (65)$$

with the solution $\beta_j = j\pi$, or $\omega_j = \pi^2 j^2$, for $j=1,2,3\dots$. Without loss of generality $C_1=1$. The general solution for the transverse vibration is a superposition of all eigenmodes:

$$\bar{w}(\bar{x}, \bar{t}) = \sum_{j=1}^{\infty} \phi_j(\bar{x}) T_j(\bar{t}) = \sum_{j=1}^{\infty} [(C_5)_j \sin(\pi^2 j^2 \bar{t}) + (C_6)_j \cos(\pi^2 j^2 \bar{t})] \sin(j\pi\bar{x}) \quad (66)$$

The constants $(C_5)_j$ and $(C_6)_j$ are determined from the initial conditions Eq. (55-56). Note that the time \bar{t} ($\bar{t} \in [0, 1/\bar{c}]$) in Eq. (54) describes a moment during the slamming load initial phase, while the \bar{t} in Eq. (66) describes a moment during the vibration phase. When the \bar{t} in Eq. (54) equals $1/\bar{c}$ which is the moment when the initial phase ends and the vibration phase starts, the corresponding time in Eq. (66) is $\bar{t} = 0$. The constants are solved from the initial conditions,

$$\bar{w}(\bar{x}, \bar{t} = 0) = \sum_{j=1}^{\infty} (C_6)_j \sin(j\pi\bar{x}) = \bar{w}_{Initial} \quad (67)$$

$$\left. \frac{\partial \bar{w}(\bar{x}, \bar{t})}{\partial \bar{t}} \right|_{\bar{t}=0} = \sum_{j=1}^{\infty} \pi^2 j^2 (C_5)_j \sin(j\pi\bar{x}) = \bar{v}_{Initial} \quad (68)$$

and result in

$$(C_5)_j = \frac{2ab}{j^7 \pi^7} \left[\frac{\bar{q}_1}{a^2 - b^2} (a \cdot \sin b\bar{t}_1 - b \cdot \sin a\bar{t}_1) \right]$$

$$-\frac{\bar{q}_1 - \bar{q}_2}{a^2 - b^2} \left(a \cdot \sin b \left(\bar{t}_1 - \frac{\bar{l}_1}{c} \right) - b \cdot \sin a \left(\bar{t}_1 - \frac{\bar{l}_1}{c} \right) \right) \right] \quad (69)$$

$$(C_6)_j = \frac{2}{j^5 \pi^5} \left[\bar{q}_2 + \frac{\bar{q}_1}{a^2 - b^2} (b^2 \cos a \bar{t}_1 - a^2 \cos b \bar{t}_1) \right. \\ \left. - \frac{\bar{q}_1 - \bar{q}_2}{a^2 - b^2} \left(b^2 \cos a \left(\bar{t}_1 - \frac{\bar{l}_1}{c} \right) - a^2 \cos b \left(\bar{t}_1 - \frac{\bar{l}_1}{c} \right) \right) \right] \quad (70)$$

Substituting Eq. (69) and (70) in Eq. (66), the deflection of the beam during the vibration phase is obtained. With the deflection known other quantities of interest, like the bending moment or the shear forces in the beam, are easily obtained. In particular the bending moment is

$$M = -EI \frac{\partial^2 w(x, t)}{\partial x^2}, \quad \bar{M} = -\frac{\partial^2 \bar{w}(\bar{x}, \bar{t})}{\partial \bar{x}^2} \quad (71)$$

Substituting Eq. (66) in Eq. (71), the following is obtained

$$\bar{M}(\bar{x}, \bar{t}) = \sum_{j=1}^{\infty} j^2 \pi^2 \left[(C_5)_j \sin(\pi^2 j^2 \bar{t}) + (C_6)_j \cos(\pi^2 j^2 \bar{t}) \right] \sin(j \pi \bar{x}) \quad (72)$$

The solution is periodic in time with the period is $2/\pi$.

2.3 Alternative Pressure Distribution, the Point-Step Load

As mentioned previously measurements of bottom pressures in high-speed boats indicate that there is a high pressure peak spreading rapidly over the bottom, followed by a considerably lower pressure over a large area of the bottom. The pressure peak was represented by the pressure (times width) q_1 above. An alternative representation of slamming is a moving point-load, F_D , followed by a constant pressure. This will be called the "Point-Step Load" in the remainder of the paper. The normalized slamming load $\bar{q}(\bar{x}, \bar{t})$ can then be expressed as

$$\bar{q}(\bar{x}, \bar{t}) = \bar{F}_D \delta(\bar{x} - \bar{c}\bar{t}) + \bar{q}_r [1 - H(\bar{x} - \bar{c}\bar{t})] \quad (73)$$

where $\delta(x)$ is a Dirac pulse and \bar{q}_r is a residual pressure following the point load. The solution to the initial phase of slamming using the "Point-Step Load" is given in [41]. The initial conditions for the vibration phase, which are the deflection and the transverse velocity of the beam at the end of the slamming load initial phase, when $\bar{t} = \bar{t}_1$, are

$$\begin{aligned} \bar{w}^p_{initial} = & 2\pi \bar{F}_D \bar{c} \sum_{j=1}^{\infty} \frac{j}{a^2 - b^2} \left(\frac{1}{b} \sin b\bar{t}_1 - \frac{1}{a} \sin a\bar{t}_1 \right) \sin j\pi \bar{x} \\ & + \frac{2\bar{q}_r}{\pi^5} \sum_{j=1}^{\infty} \frac{1}{j^5} \left[1 + \frac{1}{a^2 - b^2} (b^2 \cos a\bar{t}_1 - a^2 \cos b\bar{t}_1) \right] \sin j\pi \bar{x} \end{aligned} \quad (74)$$

$$\begin{aligned} \bar{v}^p_{Initial} = & 2\pi \bar{F}_D \bar{c} \sum_{j=1}^{\infty} \frac{j}{a^2 - b^2} (\cos bt_1 - \cos at_1) \sin j\pi \bar{x} \\ & + \frac{2\bar{q}_r}{\pi^5} \sum_{j=1}^{\infty} \frac{1}{j^5} \left[\frac{ab}{a^2 - b^2} (a \sin bt_1 - b \sin at_1) \right] \sin j\pi \bar{x} \end{aligned} \quad (75)$$

By using Eq. (66) and the above initial conditions, the free vibration constants for the "Point-Step Load" problem become

$$(C_5)_j^p = 2\bar{F}_D \bar{c} \frac{1}{\pi(a^2 - b^2)j} (\cos bt_1 - \cos at_1) + \frac{2\bar{q}_r}{\pi^7 j^7} \left[\frac{ab}{a^2 - b^2} (a \sin bt_1 - b \sin at_1) \right] \quad (76)$$

$$(C_6)_j^p = 2\pi \bar{F}_D \bar{c} \frac{j}{a^2 - b^2} \left(\frac{1}{b} \sin bt_1 - \frac{1}{a} \sin at_1 \right) + \frac{2\bar{q}_r}{\pi^5 j^5} \left[1 + \frac{1}{a^2 - b^2} (b^2 \cos at_1 - a^2 \cos bt_1) \right] \quad (77)$$

Substituting Eq. (76) and (77) in Eqs. (66) and (71), the free vibration deflection and bending moment become

$$\bar{w}^p(\bar{x}, \bar{t}) = \sum_{j=1}^{\infty} \left[(C_5)_j^p \sin(\pi^2 j^2 \bar{t}) + (C_6)_j^p \cos(\pi^2 j^2 \bar{t}) \right] \sin(j\pi \bar{x}) \quad (78)$$

$$\bar{M}^p(\bar{x}, \bar{t}) = \sum_{j=1}^{\infty} j^2 \pi^2 \left[(C_5)_j^p \sin(\pi^2 j^2 \bar{t}) + (C_6)_j^p \cos(\pi^2 j^2 \bar{t}) \right] \sin(j\pi \bar{x}) \quad (79)$$

These expressions are used for presenting various results later in the paper.

2.4 Range of Parameters for Slamming

Slamming calculations will in this paper be performed for parameters that are relevant for boats and ships. The speed at which the slamming load travels over the bottom, c , can be estimated by

$$c = \frac{V\pi}{2 \tan \beta} \cdot \frac{1}{\cos \beta} = \frac{V\pi}{2 \sin \beta} \quad (80)$$

where V is the vertical velocity of a 2D wedge dropped in water and β is the deadrise angle of the bottom, e.g., Faltinsen [14]. It will be assumed that deadrise angles of the boats of interest are in the range 5° to 45° , and the vertical velocity in the range 1 m/s to 10 m/s. Drop tests with these parameters have been performed in [1], [6] and [42]. Using these values the speed that the slamming load travels over the bottom, c , is estimated by eq. (80) to vary from 2 m/s to 200 m/s. Peak pressure and duration were estimated from among other sources the drop tests of [1], [6] and [42]. The peak pressure range and peak duration in Table 2-1 appear to cover the majority of such tests. The ratio of p_1/p_2 is naturally not clearly defined from experiments since real slamming loads differ from the two-step load presently assumed. However, for the purpose of presenting results the pressure ratio p_1/p_2 was assumed to be in the range of 2~20.

Regarding bottom stiffness, the range can be estimated to vary from that of a very soft bottom panel such as a one meter wide 3 mm thick aluminum plate ($E=70$ GPa, density 2700 kg/m^3), to a stiff bottom such as a one meter wide sandwich panel with two 15

mm thick carbon fiber skins ($E=100$ GPa, density 1500 kg/m³) on each side of a 70 mm thick high density foam core (negligible stiffness, density 250 kg/m³). This results in a bending stiffness (EI) ratio of the soft bottom to the stiff bottom of approximately 3×10^{-5} . With this ratio, the ranges of interest of the dimensionless parameters given in Table 2-2 are obtained (from eq. (50)). The length l_1 was estimated as traveling load speed times duration of the pressure peak, resulting in the normalized length \bar{l}_1 of Table 2-2 if the length of the beam is 1 m.

Table 2-1: Range of parameters studied

Parameters	Traveling load speed c [m/s]	Peak pressure [kPa]	ratio of p_1/p_2	Duration of slamming load peak [ms]
Value Ranges	2~200	10~8,000	2~20	0.01~2

Table 2-2: Range of interest of the dimensionless parameters

Parameters	Traveling load speed \bar{c}	Peak pressure \bar{q}_1	Ratio of \bar{q}_1/\bar{q}_2	Peak load length \bar{l}_1
Value Ranges	0.01~320	$10^{-3} \sim 10^5$	2~20	$2 \times 10^{-5} \sim 0.4$

In the next section dynamic deflection \bar{w} and bending moment \bar{M} will be presented. They will be normalized by the maximum static deflection \bar{w}_{ms} and the maximum static bending moment \bar{M}_{ms} that result if the beam is statically subjected to a two-step load with the same properties as the dynamic load (i.e., as in Figure 2-1). Let $\bar{x} = a$ be the right edge of the pressure pulse \bar{q}_1 . Then

$$\bar{w}_{ms} = \max_{0 < a < 1, 0 < x < 1} |\bar{w}_s| \quad \bar{M}_{ms} = \max_{0 < a < 1, 0 < x < 1} |\bar{M}_s| \quad (81)$$

where \bar{w}_s and \bar{M}_s are the normalized static deflection and bending moment, respectively; more details can be found in [41].

2.5 Results and Discussion

Figures 2-2 and 2-3 show the results of a sample calculation with the parameters $\bar{c} = 5$, $\bar{q}_1 / \bar{q}_2 = 5$, $\bar{l}_1 = 0.01$. The beam deflection and bending moment at three instances are shown. The vertical axes represent the deflection \bar{w} / \bar{w}_{ms} and the bending moment \bar{M} / \bar{M}_{ms} , respectively. The plots (a) in Fig. 2 and Fig. 3 show the initial deflection and bending moment of the beam at the beginning of the vibration phase. The plots (b) and (c) show the deflection and bending moment of the beam when the maxima and the minima occur. In this case, the maximum deflection during the vibration phase reaches 98% of the maximum static deflection and the maximum bending moment reaches 109% of the maximum static value. In this particular case, the maxima occur during the

vibration phase of the slamming (as opposed to during the initiation phase). Since damping was omitted, the solution during the vibration phase is a sum of periodic functions. In practice, this is not true since the vibration in water tend to be highly damped. In the remainder of the paper only the response that occurs within the first period of the lowest structural eigenfrequency after the load has reached the end of the beam will be considered; response after this time will be assumed to have drastically decreased due to damping.

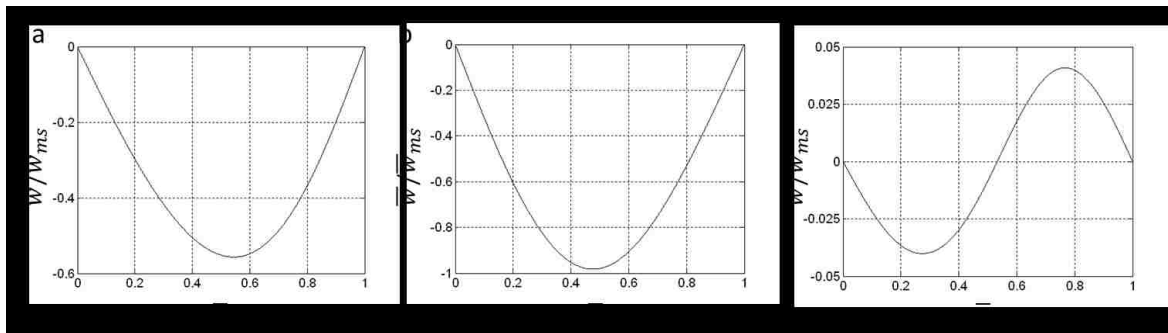


Figure 2-2: Deflection ratio \bar{w}/\bar{w}_{ms} during the vibration phase when $\bar{c} = 5$, $\bar{q}_1/\bar{q}_2 = 5$, $\bar{l}_1 = 0.01$. (a) Initial deflections of the beam, (b) Deflections of the beam when the maximum deflection occurs (at $t=0.10$), (c) Deflections of the beam when the minimum of the maximum deflections occurs (at $t=0.26$).

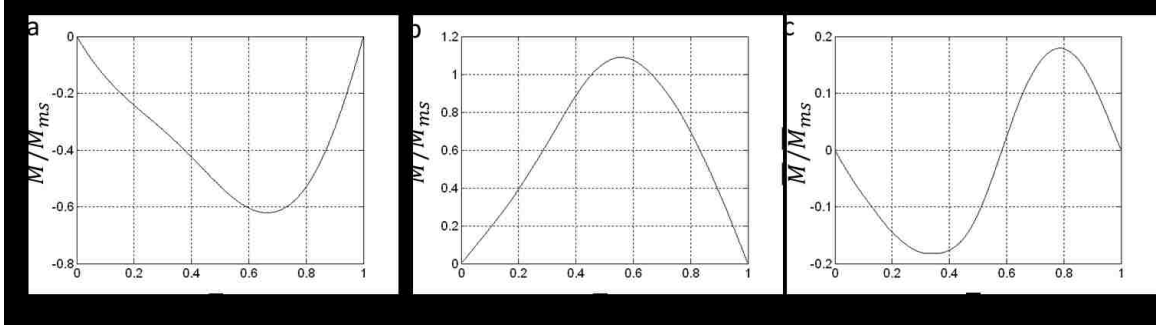


Figure 2-3 : Bending moment ratio \bar{M} / \bar{M}_{ms} during the vibration phase when $\bar{c} = 5$, $\bar{q}_1 / \bar{q}_2 = 5$, $\bar{l}_1 = 0.01$. (a) Initial bending moments of the beam, (b) Bending moments of the beam when the maximum bending moment occurs (at $t=0.42$), (c) Bending moments of the beam when the minimum of the maximum bending moments occurs (at $t=0.25$).

Figures 2-4 and 2-5 show the effects of the slamming load traveling speed on structural response. The vertical axes are the deflection ratio $\bar{w}_{md} / \bar{w}_{ms}$ and the bending moment ratio $\bar{M}_{md} / \bar{M}_{ms}$, respectively. Here, \bar{w}_{md} and \bar{M}_{md} are the maximum dynamic deflection and bending moment for any location and any time during the vibration phase (within the first period of the lowest eigenfrequency of the beam after the load reaches its end, i.e. within the normalized time $2/\pi$ after the load reaches the end of the beam (see below); the response is assumed to decrease so rapidly due to the damping of the water that the response at later times is of little relevance). As seen in the figures $\bar{w}_{md} / \bar{w}_{ms}$ and $\bar{M}_{md} / \bar{M}_{ms}$ depend strongly on the slamming load traveling speed, \bar{c} . When the normalized slamming load traveling speed, \bar{c} , is around 2, the maximum dynamic deflection during the vibration phase is approximately 55% higher than the static one and the maximum dynamic bending moment during the vibration phase is approximately 60% higher than the static one. There is a form of resonance occurring in

the structure. The analysis for the initial phase shows a similar phenomenon [41]. From equations (45) and (48) the eigenfrequencies of a simply supported Euler-Bernoulli

beam can be calculated: $\omega_i = \frac{\pi^2 i^2}{L^2} \sqrt{\frac{EI}{\mu^*}}$, ($i = 1, 2, 3, \dots$). The normalized period of the

lowest eigenfrequency is $2/\pi$, which was used above. If we define a characteristic

velocity as $c_i = \frac{L\omega_i}{2\pi}$, then the dimensionless characteristic velocities are $\bar{c}_i = \frac{\pi i^2}{2}$. The

first three dimensionless characteristic velocities are 1.6, 6.3 and 14.1. Figures 2-4 and

2-5 show that the most severe structural responses occur when \bar{c} is in the neighborhood

of 2.2-2.4, which is slightly higher than the first characteristic velocity, $\bar{c}_1 = 1.6$. This in

essence agrees with Faltinsen [17] who suggested that mainly the lowest eigenmode is

of importance as far as the maximum strains in the bottom are concerned.

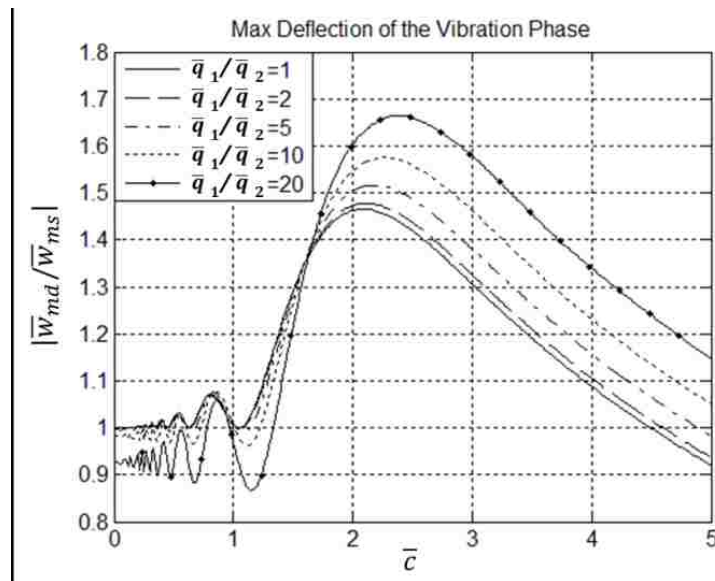
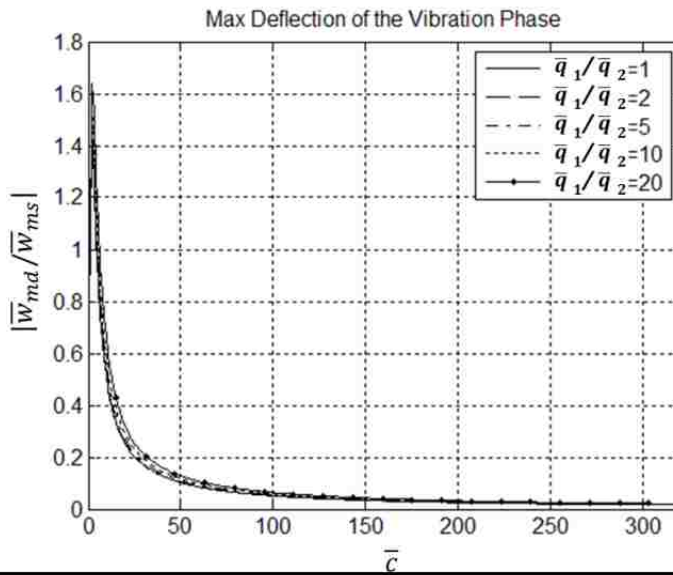


Figure 2-4: Maximum deflection ratio during the vibration phase, versus speed of the slamming load for five different pressure ratios \bar{q}_1/\bar{q}_2 when $\bar{l}_1 = 0.01$. The bottom figure is a zoomed-in version of the upper one.

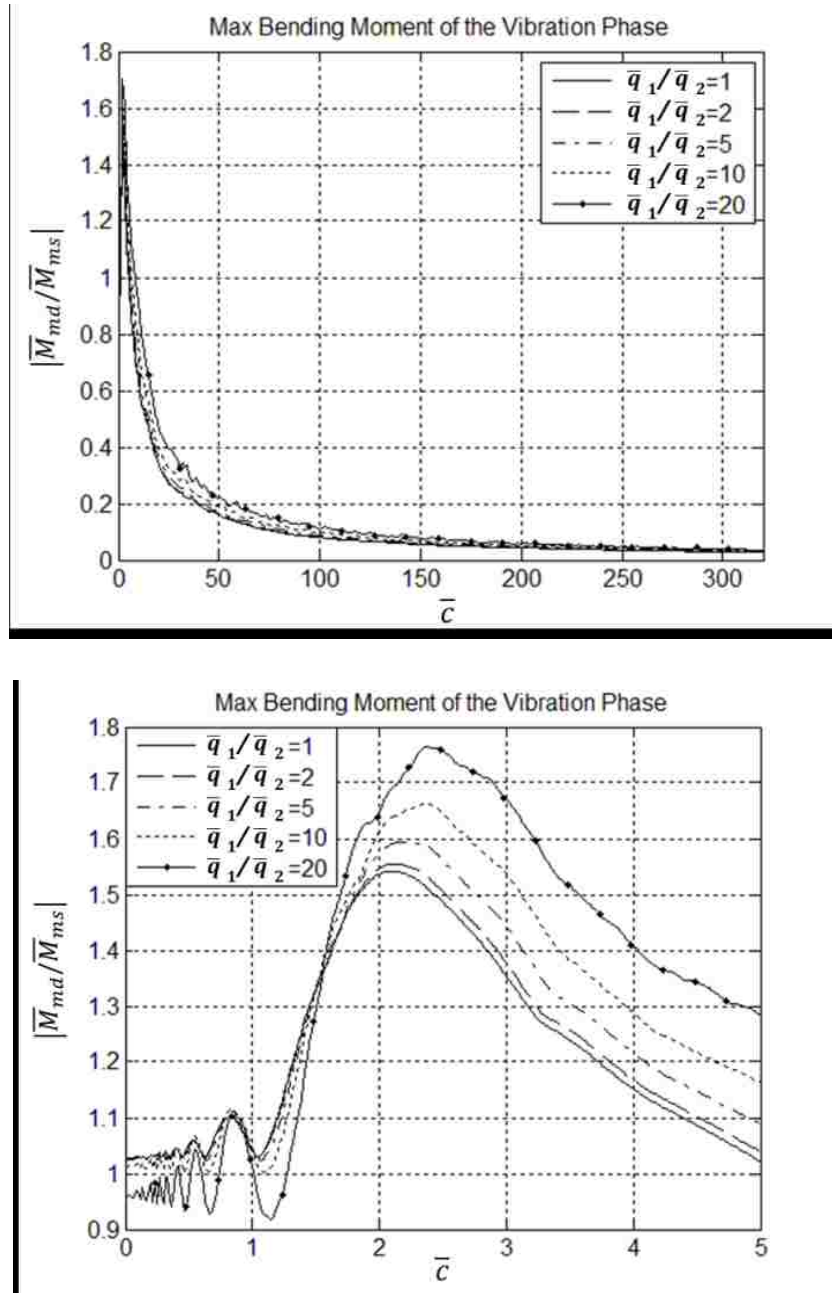


Figure 2-5: Maximum bending moment ratio during the vibration phase, versus speed of the slamming load for five different pressure ratios $\overline{q}_1/\overline{q}_2$ when $\overline{l}_1 = 0.01$. The right figure is a zoomed-in version of the left one.

With increasing propagation speed \bar{c} , beyond approximately 2.4, the maximum deflection and bending moment, \bar{w}_{md} and \bar{M}_{md} , decrease rather rapidly. When \bar{c} is larger than the second characteristic velocity, $\bar{c}_2 = 6.3$, the ratios $\bar{w}_{md} / \bar{w}_{ms}$ and $\bar{M}_{md} / \bar{M}_{ms}$ start to decrease below unity. In other words, the maximum dynamic structural responses during the vibration phase become less than the corresponding maximum static ones, when the slamming load travels faster than the second characteristic velocity (with a few exceptions). When \bar{c} is larger than the third characteristic velocity, 14.1, the ratios $\bar{w}_{md} / \bar{w}_{ms}$ and $\bar{M}_{md} / \bar{M}_{ms}$ are rather small (less than, say, half of the static equivalents). This is in the so-called structural inertia phase (Faltinsen [17], Kvalsvold [18]), where the slamming force is essentially balanced by structural inertia during the initial phase of the slam. Thus, the deformation during the slam itself is rather small, but the slam has induced transverse velocities in the panel which can result in considerable deformation after the slamming load has subsided. For \bar{c} larger than, say, 55, the maximum dynamic deflection and bending moment are less than 20% of the corresponding maximum static values.

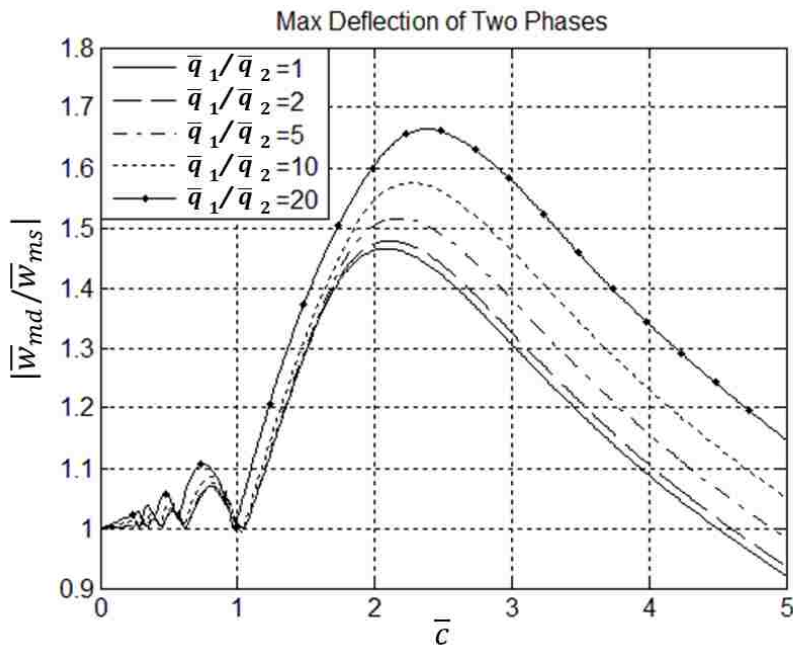
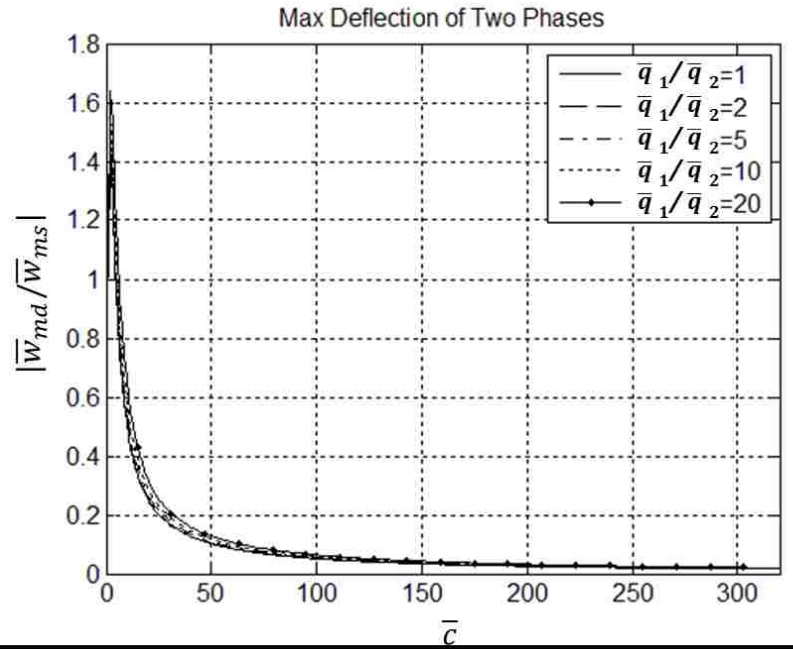


Figure 2-6: Maximum deflection ratio for both phases (initial and vibration phases) versus speed of the slamming load for five different pressure ratios \bar{q}_1 / \bar{q}_2 when $\bar{l}_1 = 0.01$. The bottom figure is a zoomed-in version of the upper one.

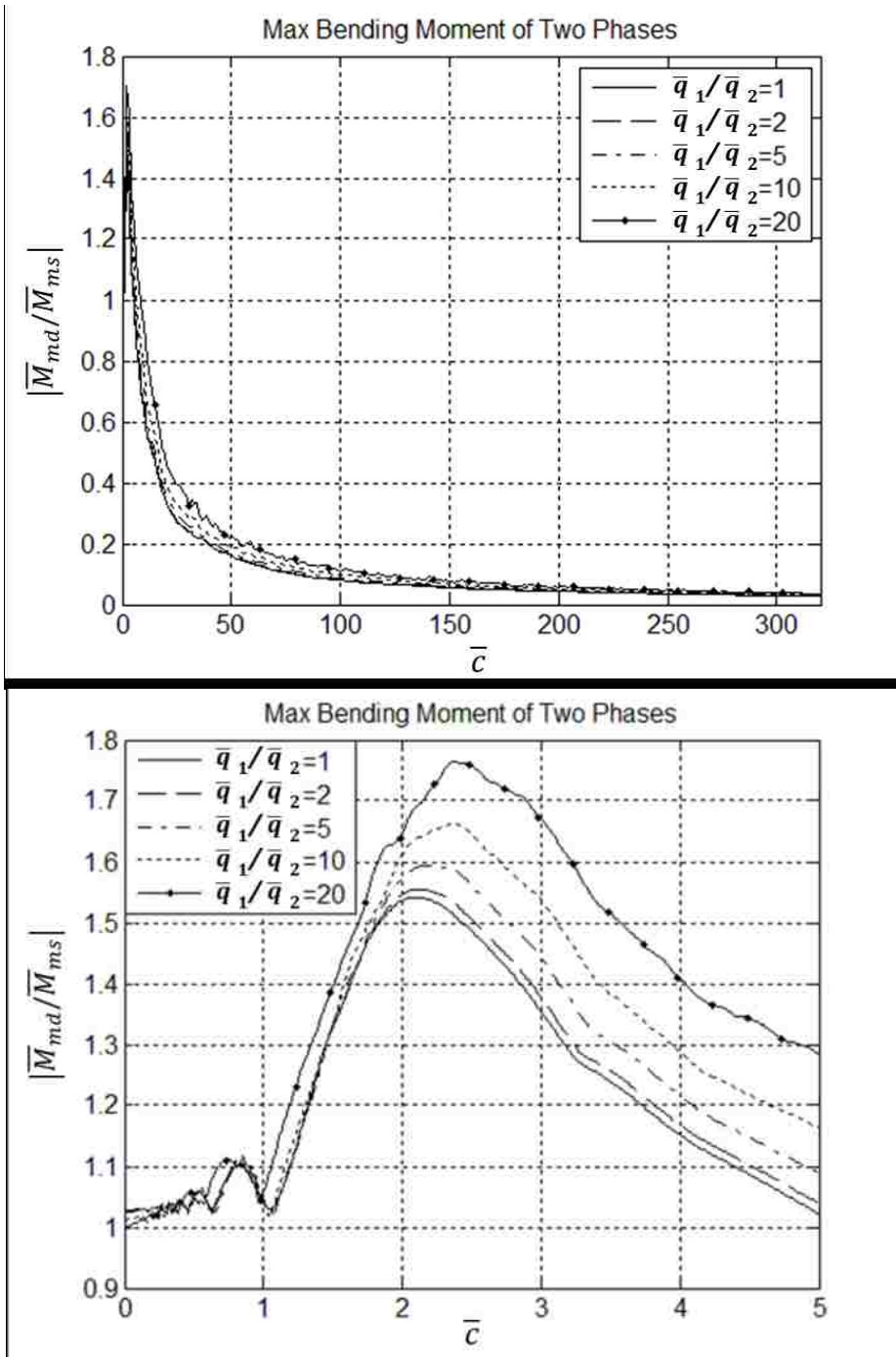


Figure 2-7: Maximum bending moment ratio for both phases versus speed of the slamming load for five different pressure ratios $\overline{q}_1/\overline{q}_2$ when $\overline{l}_1 = 0.01$. The bottom figure is a zoomed-in version of the upper one.

Figures 2-6 and 2-7 summarize the effects of the slamming load traveling speed on structural response for both the initial phase and the subsequent vibration phase. When \bar{c} is slightly higher than the first characteristic velocity the structure experiences the most severe structural response, while the dynamic response drops below the static ditto at slamming load traveling speed near, or above, the second characteristic velocity. After that, the maximum structural response decreases rapidly with increasing slamming load traveling speed. When $\bar{q}_1 / \bar{q}_2 = 5$ and $\bar{l}_1 = 0.01$, the time (from the beginning of the initial slam) when the maximum deflection and the maximum bending moment occur is approximately $\bar{t} = 1/\bar{c}$ for $\bar{c} < 2$ (i.e., the maxima occur just when the load reaches the right end of the beam). For higher \bar{c} the maxima occur later (approximately at $\bar{t} = 0.6 / \bar{c} + 0.17$ for $\bar{c} > 2$).

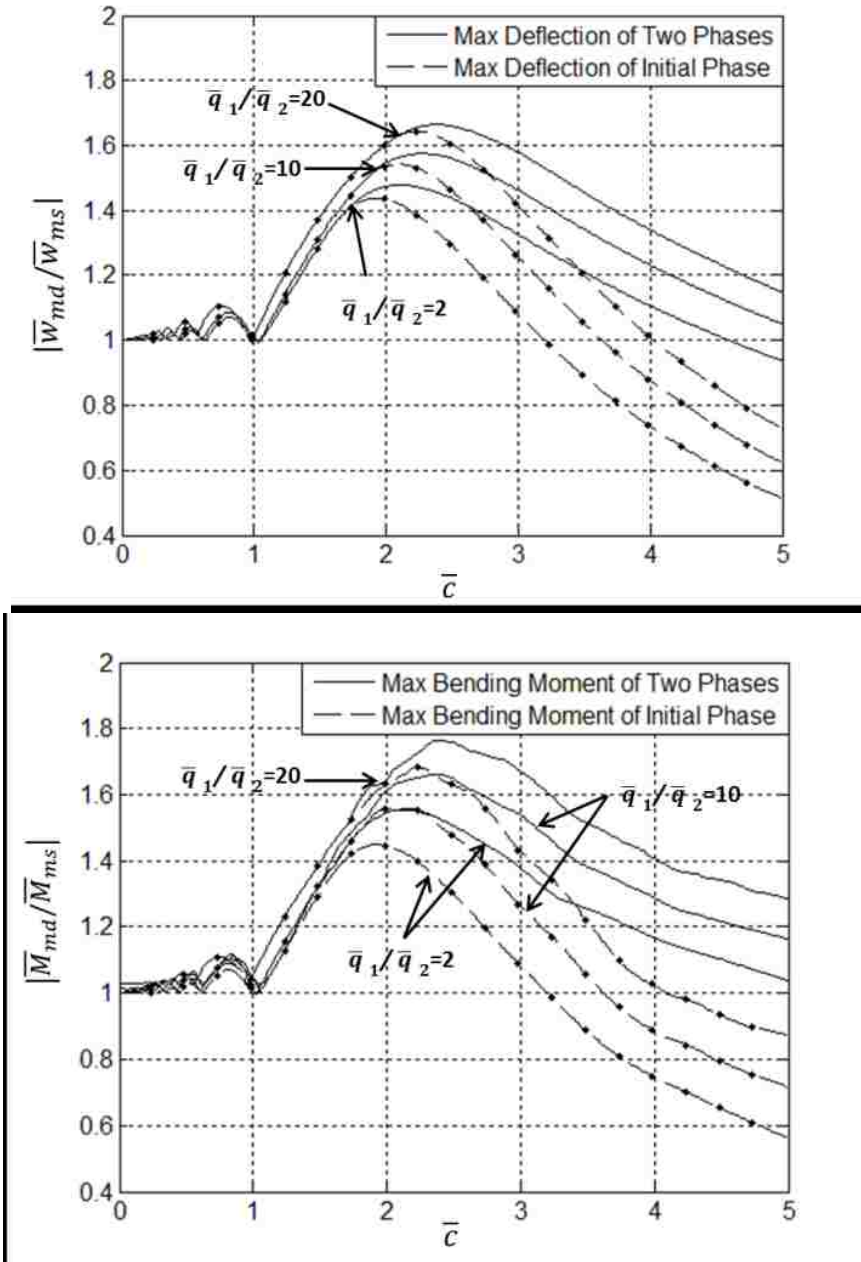


Figure 2-8: Maximum deflection and bending moment for the initial phase, as well as for the two phases together, for three different pressure ratios \bar{q}_1/\bar{q}_2 when $\bar{l}_1 = 0.01$.

Figure 2-8 shows the maximum structural response during the initial phase as well as during the whole slamming event (i.e., the initial and vibration phases). As can be seen, when \bar{c} is relatively small (less than the first characteristic velocity $\bar{c}_1 = 1.6$), the maximum deflection and the maximum bending moment occur during the initial slamming load phase, while with increasing \bar{c} the maximum structural responses occurs during the vibration phase. When \bar{c} is very small, the behavior of the structure is essentially quasistatic and the dynamic responses, \bar{w}_{md} and \bar{M}_{md} , are close to the maximum static responses, \bar{w}_{ms} and \bar{M}_{ms} . With the increase of \bar{c} , the behavior of the structure is more and more dynamic. When \bar{c} is close to the first characteristic velocity, presumably there is a form of resonance in the structure. Since the slamming load traveling speed is not too fast, the structure has sufficient time to reach its maximum response during the initial phase. However, for higher \bar{c} the system does not have time to reach its maximum deformation until the load has passed. When the velocity of the slamming load, c , is considerably higher than the first characteristic velocity c_1 , then the beam does not have time to deflect very much before the load has passed; however, an impulse has been imparted on the beam. This impulse scales as qL^2/c , and the rate of deformation of the beam, \dot{w} , then scales as $qL/(\mu^*c)$. The maximum deflection, which occurs after the load has passed, scales as $qL^3 / (c\sqrt{\mu^*EI})$ and the normalized maximum dynamic deflection scales as $\bar{w}_{md} \sim \bar{q} / \bar{c}$. This explains why beyond the resonance region, the faster the slamming load travels the less the structure responds.

Some effect of varying the peak pressure ratio, \bar{q}_1 / \bar{q}_2 , is also illustrated in Figures 2-8. With $\bar{l}_1 = 0.01$, increasing the pressure ratio from 2 to 20 leads to higher deflection and bending moment ratios, $\bar{w}_{md} / \bar{w}_{ms}$ and $\bar{M}_{md} / \bar{M}_{ms}$. In particular, the larger the fraction of the total load that is in the peak, the larger the structural dynamic response (relative to the corresponding static response).

An effect of peak load length, \bar{l}_1 , is shown in Figure 2-9 for $\bar{q}_1 / \bar{q}_2 = 5$. Three different \bar{l}_1 were used, 0.001, 0.01 and 0.1. The deflections and bending moments are normalized by their static equivalents. The figures indicate that both the normalized maximum deflection and the normalized maximum bending moment increase with increasing peak load length, \bar{l}_1 . This increase is apparent during both the initial and the vibration phases. Hence, a slamming load with long duration of the peak pressure appears to generate more deflection and bending moment compared to the static equivalents. Thus, just as in Fig. 8, the larger the fraction of the total load that is in the peak, the larger the structural dynamic response (relative to the corresponding static response).

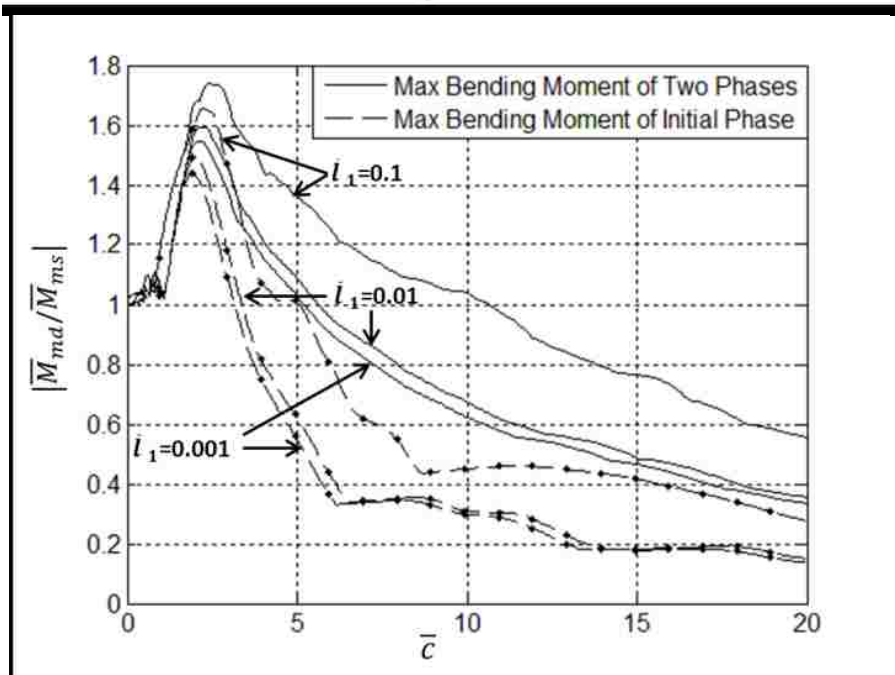
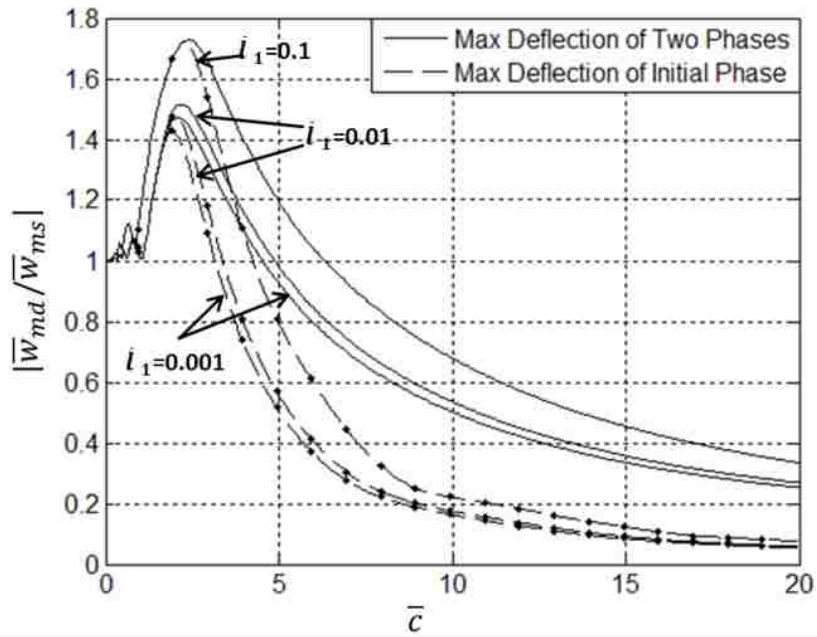


Figure 2-9: Maximum deflection and bending moment ratios during the initial phase as well as during the two phases. Results with three different \bar{l}_1 are presented when $\bar{q}_1/\bar{q}_2 = 5$.

Some further insight into the effect of load in the initial peak can be gained using the Point-Step load outlined previously. This load consists of a point load F_D followed by a constant pressure q_r . The maximum dynamic deflection and the maximum dynamic bending moment were calculated for different point loads F_D . In this case, the deflection was normalized by the static deflection of a beam loaded by an evenly distributed equivalent pressure q_{eq} only, i.e., by $\bar{w}_{eq} = |5\bar{q}_{eq}/384|$, where $q_{eq} = (F_d + q_r L)/L$. Likewise, the dynamic bending moment was normalized by $\bar{M}_{eq} = |\bar{q}_{eq}/8|$. The results are presented in Figures 2-10 where deflection and bending moment are plotted versus $F_D/q_r L$. It is seen that the maximum structural deflection and the maximum bending moment during the two slamming phases mainly increase with increasing point force ratio $F_D/q_r L$, except for lower speeds \bar{c} . Note that when the slamming load traveling speed is very low ($\bar{c}=0.1$), the behavior of the beam is almost quasi static. The ratios $\bar{w}_{md}/\bar{w}_{eq}$ and $\bar{M}_{md}/\bar{M}_{eq}$ then initially decrease before increasing with increasing point force ratio, $F_D/q_r L$, just as in a statically loaded beam. Further, as previously seen when \bar{c} is approximately 2 (close to the first characteristic velocity, 1.6), the maximum deflection and the maximum bending moment of the structure are substantially larger.

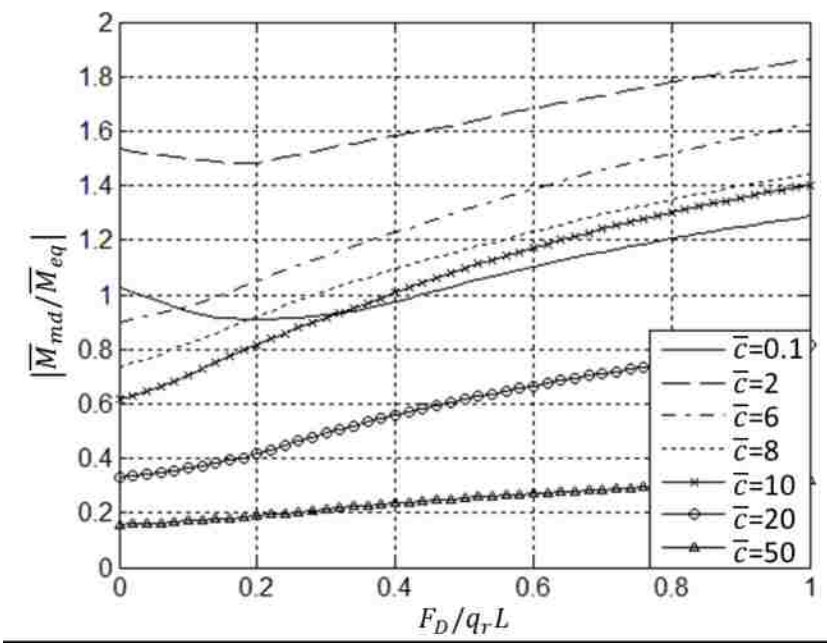
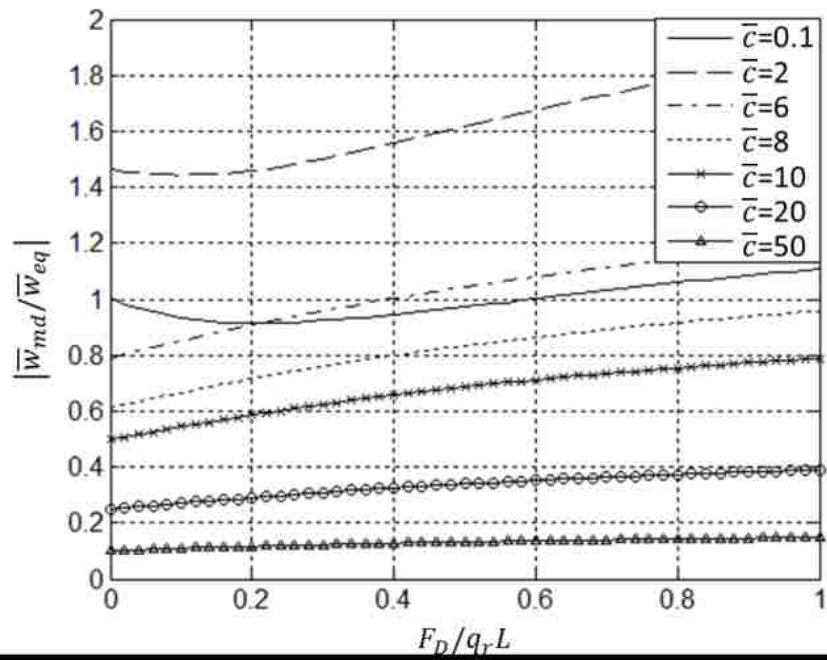


Figure 2-10: Maximum deflection ratio and bending moment ratio from the two phases versus point force ratio, normalized by maximum deflection and bending moment from static evenly distributed load q_{eq} .

Figure 2-10 shows that point loads have rather limited effects on the structural response when the slamming load travels slowly. For example, at $\bar{c} = 2$ the increases in deflection and bending moment is about 3-6% for $F_D / q_r L = 0.4$ compared with $F_D = 0$ (when normalized by \bar{w}_{eq} and \bar{M}_{eq}). However, at higher speeds such as $\bar{c} = 10$ or $\bar{c} = 20$, the behavior of the beam becomes more dynamic and the increase is quite considerable. For $\bar{c} = 10$ the increases in deflection and bending moment are 32% and 63%, respectively, when $F_D / q_r L = 0.4$ compared with $F_D = 0$. For $\bar{c} = 20$ the deflection increased 30% and the bending moment increased 68% when $F_D / q_r L = 0.4$ compared with $F_D = 0$.

Figs. 2-8 and 2-9 indicate that the larger the fraction of the total load that is in the peak, the larger the structural response when compared to the corresponding static ditto (at least for $\bar{c} > \bar{c}_1$). Fig. 2-10 shows this relation in more detail. Now, Fig. 2-11 shows the influence of the shape of the peak when the load in the peak $(\bar{q}_1 - \bar{q}_2)\bar{l}_1$ as well as the total load $(\bar{q}_1\bar{l}_1 + \bar{q}_2(1 - \bar{l}_1))$ are constant. The responses are here normalized by the responses of a beam statically loaded by an evenly distributed pressure with the same total load (thus, loaded with $q_{eq} = (q_1 l_1 + q_2(L - l_1)) / L$, or $q_{eq} = (F_d + q_r L) / L$ in the case of a point-step load). Fig. 2-11 indicates that as long as the ratio of the force in the peak to the total force is constant, a load with a low pressure ratio \bar{q}_1 / \bar{q}_2 applied over a larger distance \bar{l}_1 leads to a more severe response

than a load with a higher pressure ratio applied over a shorter distance. Kvalsvold and Faltinsen have studied this effect in a hydroelastic slamming analysis and reached the same conclusion [18]. They pointed out that high peak pressure does not necessarily mean large stresses in the structure and very large pressure peaks may be too concentrated in space and time to have a considerable influence on the maximum bending stresses.

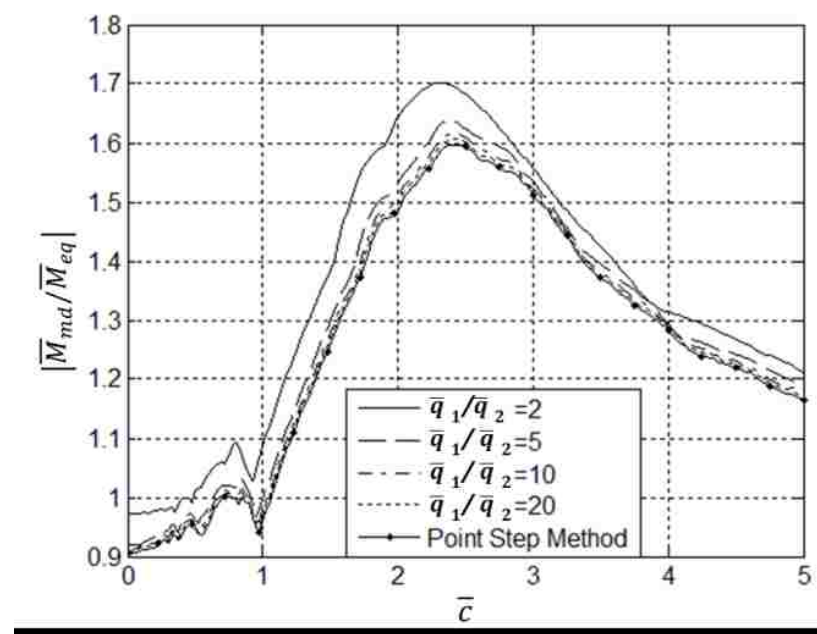
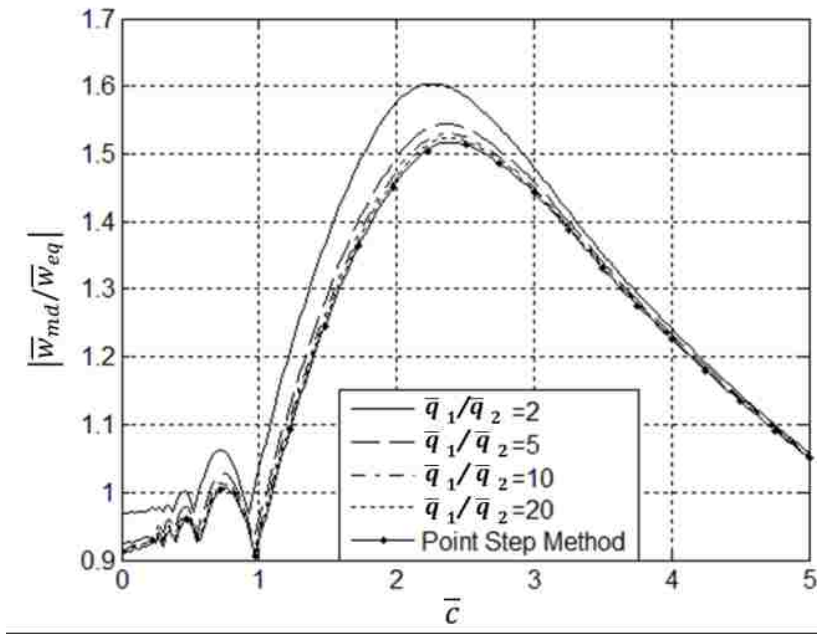


Figure 2-11: Maximum deflection ratio and bending moment ratio from the two phases versus speed of the slamming load when the total load on the beam is the same (at the time the load reaches the end of the beam). Five different pressure peak profiles are considered, including "point-step" load.

2.6 Conclusions

Deflections and bending moments due to water slamming against the bottom of a vessel were calculated using a simplified beam model subjected to moving loads. The effect of slamming load travelling speed on structural response was investigated. When the traveling speed is very low, the behavior of the structure is quasistatic and the dynamic responses are close to their static counterparts. But when the speed approaches the first characteristic speed of the panel, the maximum deflection and bending moment increase considerably. The increase of deflections and bending moments could be more than 65% and 75%, respectively. With a further increase of the slamming load traveling speed, the maximum structural responses decrease rapidly. The maximum structural responses occur during the slamming load initial phase when the slamming load travelling speed is under a certain speed in the neighborhood of the first characteristic speed. At higher speeds of the load, the maxima occur during the vibration phase.

The results show that the lowest natural frequency of the bottom panel plays a key role in the structural response. If the time it takes for the slamming load to traverse the bottom panel is near the period of the lowest eigenfrequency, then the structural response (deflection, bending moment) is large. It indicates that it may be possible to tailor bottom panels to avoid large deflections and bending moments. In particular, panel stiffnesses could be avoided for which the characteristic speed of the panel is near the propagation speed of the slamming load. Granted, this may be difficult or even impossible to achieve for any speed and any sea state for a particular boat. Nevertheless,

it may be possible to design a boat's bottom such that the effects of the most severe condition (speed, sea state) are reduced. It should further be noted that the speed and the pressure of the moving load depend on deadrise and roll angles of the hull; for example reducing the deadrise angle would increase the speed of the slamming load (which may be beneficial) but also the pressure (which would not be beneficial). More analyses using more refined models would be required to gain a better understanding of the potential of tailoring bottom panels for slamming.

This study also sheds some light on the effects of the shape of the peak pressure on structural responses. From an experimental point of view, the pressures are sensitive to the contact angle between water and the bottom panel and the peak pressures tend to be difficult to accurately measure. There are often large uncertainties in the peak pressures from experimental measurements. However, as indicated a high pressure peak does not necessarily lead to large structural response. The results from the Point-Step load method demonstrate that the maximum structural deflection and bending moment are not sensitive to the peak pressure magnitude of a slamming load. When the total load on the structure and the residue pressure of a slamming load are the same, a slamming load with a point force causes less response of the structure than a slamming load with a finite peak pressure but longer peak length. However, the larger the fraction of the total load that is in the peak, the larger the structural response when compared to the corresponding static ditto.

The results presented in this study may be enlightening, but the validity and implications need to be verified. More advanced studies, as well as correlations with experimentally measured slamming response using the Numerette research craft, are underway.

2.7 Acknowledgements

This work is supported by the Office of Naval Research through Grants N00014-11-1-0506 and N00014-13-1-0616.

Chapter 3. Steel/Composite Hybrid Slamming Test Boat

Manufacturing

3.1 Introduction

Slamming is very dynamic in nature and is one of the most critical phenomena from the viewpoint of structural design of high-speed crafts. However, today's high-speed craft designs strongly rely upon semi-empirical design methods where slamming in essence is considered equivalent with a static uniformly distributed pressure on the bottom. The simplified modeling of this actual non-uniform, transient, dynamic and coupled loading disregards a large number of effects and restricts the ability to design an optimized structure that can make full use of the properties of materials. In order to optimize vessels, better knowledge about the response of bottom panels to real slamming conditions is desired. The development of the present Slamming Load Test Facility, Numerette, is a step in this direction. This facility, which in essence is a high speed craft with removable bottom panels and replaceable bottom geometry, is highly instrumented and operated at high speed in various sea states.

Composite materials are widely used in the structures of high performance marine vessels today because of their high strength to weight ratios, fatigue and corrosion resistance, high strain limits, excellent thermal and sound isolation. For example, the Visby Class corvette is a sandwich-construction built of carbon fiber reinforced plastic

and it is one of the largest all composite structures ever built [23]. In order to use composite materials on bigger ships, there is interest in combining composites with steel in a hybrid ship, with the goal to be able to obtain a structure which draws on the advantages of both materials [24]. Since steels are recognized for their high stiffness, ductility, isotropy, weldability and the relative ease and familiarity of their use for both design and manufacture, by combining traditional steel with modern composite materials, a hybrid ship structure could be superior in certain aspects to traditional steel ship designs. This slamming load test facility is also an attempt to shed some light on a new concept of building high-speed crafts with steel/composite hybrid ship structures.

Several different hybrid ship structures have already been proposed. One concept is to use lightweight composite structures for the bow and stern, where the bending loads are low, and to use more traditional steel construction to take the higher bending loads in the ship's center section [25, 26]. Another concept, called MACH (Modular Advanced Composite Hull form), was developed for lifting bodies and utilizes a steel "rib-cage" which has relatively small panels attached to it [27]. The Numerette has similarities with the latter. One major difference between the present concept and the MACH concept is the size of the steel truss as well as composite panels. The presently considered hulls consist of major steel longerons and very large composite panels, whereas the MACH concept utilizes much smaller composite panels and many more steel members. The Numerette's steel truss was designed to carry bending loads, whereas the composite skins were designed to carry shear and water pressure loads. The steel truss could be fabricated and the ship could be pre-outfitted before the composite

panels were attached. This allows very good access and it vastly simplifies outfitting. Further, the majority of the most highly loaded items could be mounted to the steel truss, which would be considerably easier than mounting to composite panels. The joints between the composite panels and the steel truss could further be designed such that some of the panels would be blown out in a controlled fashion to release pressure from an internal blast.



Figure 3-1: Slamming load test facility boat

Under the guide of this new concept, a 9 meter long, 1.9 meter wide hybrid slamming load test facility boat was designed and manufactured by Grenestedt and co-workers

[28-39], Figure 3-1. This hybrid boat was made with a welded AL-6XN superaustenitic non-magnetic stainless steel frame and composite sandwich panels. The stainless steel truss was made with bulkheads every 1.9 m, a small keel, two large bottom longerons, two small chine longerons and two small deck longerons. The steel truss (Figure 3-2 and Figure 3-3) was designed and manufactured by Grenestedt and co-workers.

The truss is closed out with composite sandwich panels. The composite panels were made by vacuum infusing, including 10 bottom panels, 10 side panels, 7 deck panels, 19 bulkhead panels and 4 hatches. Carbon fiber, glass fiber, PVC foam core and vinyl ester and epoxy resin were used during the panel manufacturing process.

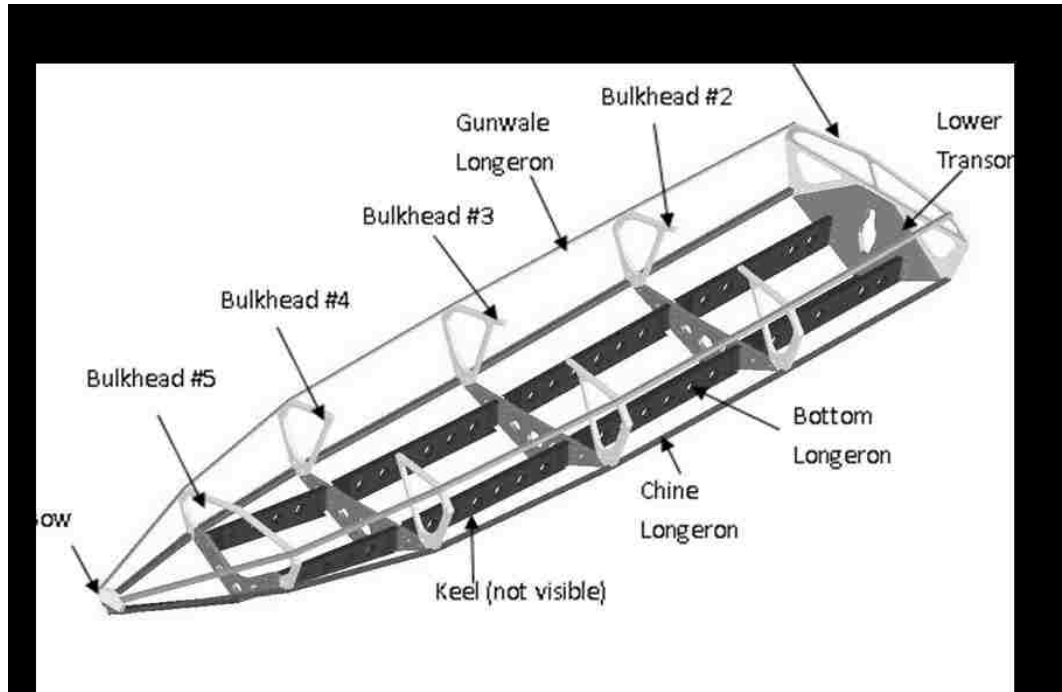


Figure 3-2: Steel framework of craft.

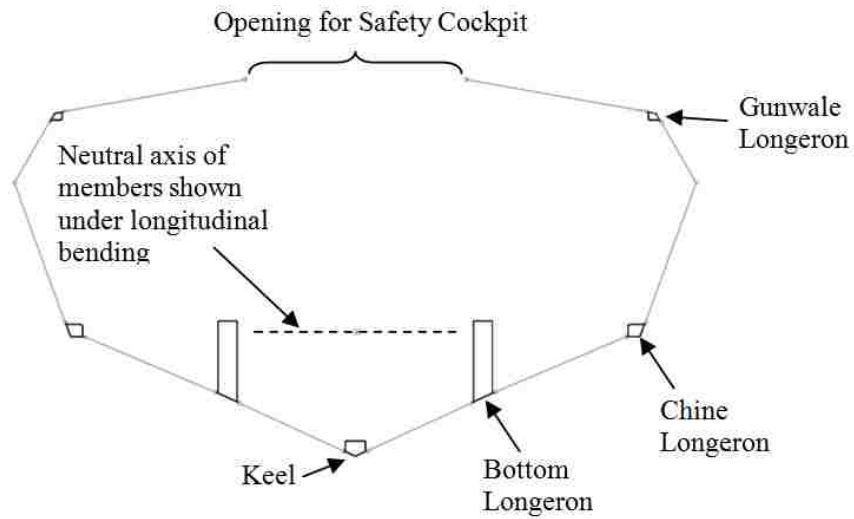


Figure 3-3: Transverse cross section taken to the fore of the 3rd bulkhead

3.2 Composite Panels Manufacturing

As mentioned previously, the boat consists of 50 composite panels, including 10 bottom panels, 10 side panels, 7 deck panels, 19 bulkhead panels and 4 hatches. All composite panels were made by 5-axis CNC routing of foam cores, and vacuum infusing vinyl ester or epoxy resin into glass or carbon fiber skins onto foam cores.

3.2.1 Constructions of Side Panels and Top Deck Panels

An example of the manufacturing of a composite panel is shown in Figure 3-4 and 3-5. Two foam cores were milled to the designed dimensions using a Hendrick 5-axis CNC router and the edges were beveled 45°. The foam cores were slightly smaller than the openings in the truss frame so that the two skins could come together completely where the panels were bonded to the frame. Both sides of the foam core initially were scored with a grid to help the resin flow. The scores were 2mm wide by 2 mm deep and the score spacing was 25 mm. This scoring will be referred as the standard foam prep in the future text. The foam core and resin channel designs were created in CAD models of the foam core and tool paths were generated. The G-code was verified by using the Vericut software to check for faults in the coding. The foam was held flat to the router table using the table's integrated vacuum system. To further ensure a flat surface and well defined depths of the resin channels, the foam was first planed flat with the router. Two finished foam core pieces are shown in Figure 3-4.

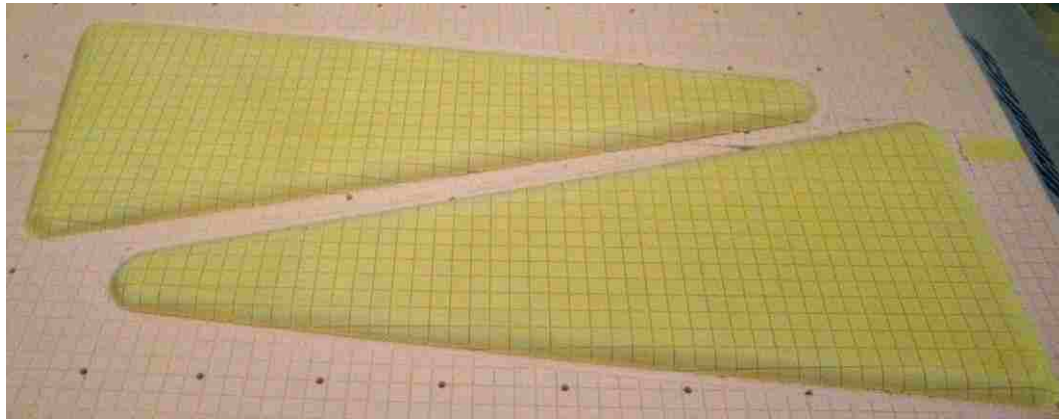


Figure 3-4: Machined foam cores for conventional sandwich panels.

Figure 3-5 shows a photo from a composite panel's vacuum infusion. In this case, two side composite panels for bay 5 were laid up on the infusion table. All side panels share the same layup which is as follow. One layer of carbon fiber (0° , 90°) by JB Martine, which is the outer skin. One layer of Hexcel 7725 glass fiber (0° , 90°). A Divinycell H80 foam core from Diab with the thickness of 12.7mm. One layer of DB240 glass fiber ($\pm 45^\circ$) as the inner skin. The 0° direction of all fabrics was parallel with the keel of the boat. On top of the inner skin, two layers of DB240 reinforcement strips were laid along the edges of the foam. The whole set-up was covered with a peel ply. A resin transfer medium was placed on top of the panels near the resin port, from where the resin was infused. The resin transfer medium covered approximate 1/3 of the panel. In order to reduce the risk of air leaks further, the breather was placed around panels. Finally a vacuum bag was placed on top to seal the panels and the whole assembly was evacuated of air for over 8 hours. For each experiment the vacuum pump was regulated at around -90 kPa of gauge pressure.

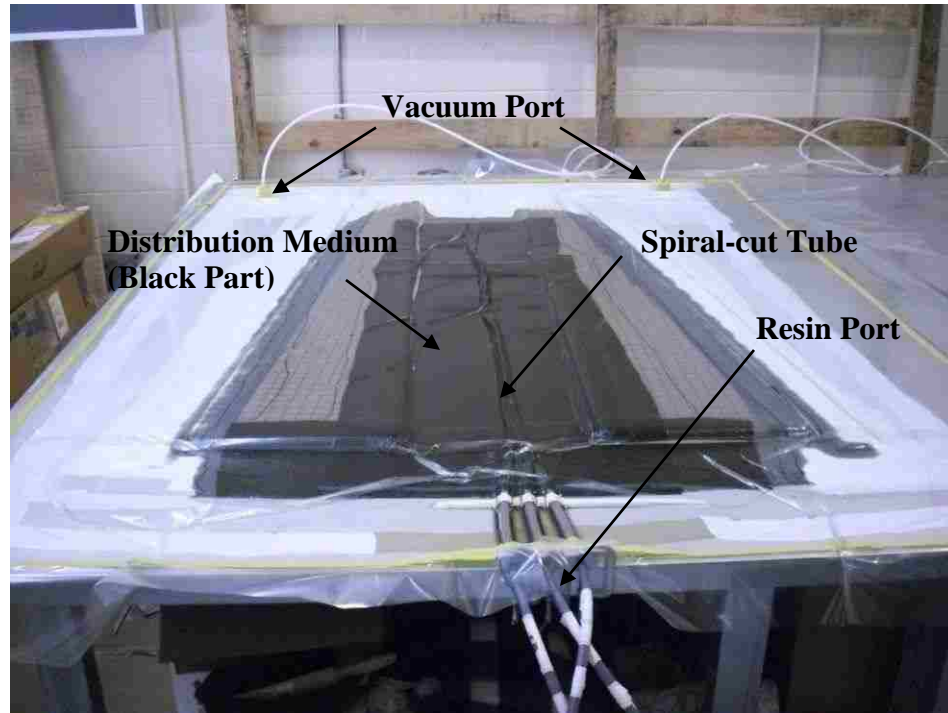


Figure 3-5: Composite panel set-up covered with a sealed vacuum bag

The resin was mixed according to Dow's specifications (1.5% Methyl Ethyl Ketone Peroxide (MEKP), 0.2% Cobalt Naphthenate (CoNap) of 15% concentration, 0.025% Dimethylaniline (DMA), and 0.13% 2,4-Pentanedione (2,4-P)), and was degassed prior to the infusion until the majority of bubbles had vanished (approximately 5 min). The resin was drawn into the mold by vacuum. It took approximately 20 minutes to infuse two panels. After the infusion had completed the resin port was closed off and the pressure under the vacuum bag was allowed to equalize. The vacuum pressure was then slowly reduced using a vacuum regulator to reduce the chances of the vinyl ester boiling. The vacuum port was left open until the resin had cured. When the resin had fully cured,

the panels were demolded and cut with a waterjet cutter or by hand to the required dimensions.

Seven deck panels were manufactured in a similar way. The layup details of deck panels are the following: one layer of carbon fiber DBL 700 on the top, 12.7 mm thick H80 foam core, one layer of DBL 700 on the bottom, plus two reinforcing layers of DBL700 around the edge of the foam core. The manufacturing of the biggest panel on the boat is demonstrated in the Figure 3-6, which is the deck panel between bulkheads 3 and 4.



Figure 3-6: Manufacturing of the biggest composite panel on the boat.

3.2.2 Bottom Construction

Bottom panels are Fiber-reinforced plastic (FRP) sandwich panels manufactured by vacuum infusing Ashland 8084 vinyl ester resin into thin glass fiber or carbon fiber skins on each side of a polymer foam core. All foam cores of the bottom panels are 18-mm-thick Divinycell H250 foam with infusion grooves on both sides. The foam cores were routed slightly smaller than the opening in the steel frame and the edges were beveled 30°. The skins come together at the end of the foam core where the panel was bonded to the steel frame.

For the present research, strains on the outer skin of the bottom panels in bays 2, 3, and 4 were to be measured. The strain gages could not be attached to the outer skin using traditional methods due to hydrodynamic smoothness requirements and the harsh environment, so foil strain gages were embedded in the bottom panels, Figure 3-7. Foil strain gages by Vishay Inc. were located on the outer surface of the foam core. The strain gages were bonded to flat thin fiberglass plates. The plates were made of a single layer of Hexcel 7725 glass fiber fabric infused with vinyl ester, and cut into Paddle-like shapes. Figure 3-8 shows the paddles ready to be bonded to the foam core. The leads of the strain gages were set in a zigzag pattern to protect them from potential damage under high strains. The paddles were aligned and bonded in place using 3M's DP 125 two part epoxy.

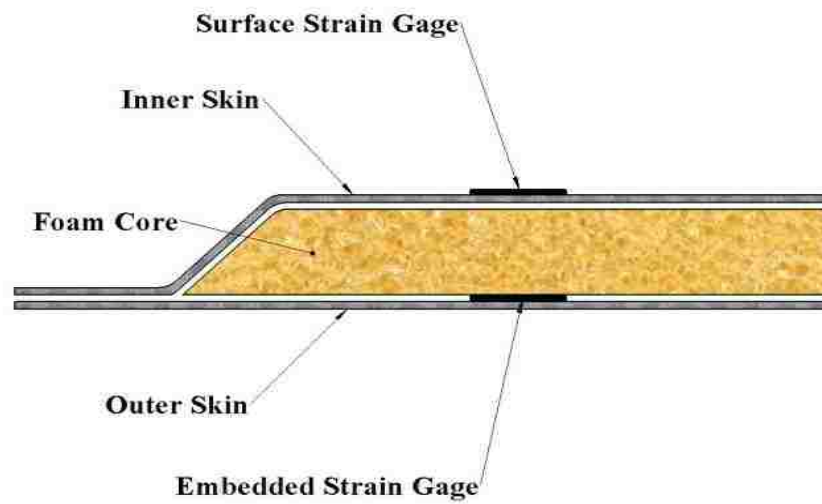


Figure 3-7: Bottom composite sandwich panel with embedded strain gages



Figure 3-8: Strain gage paddles bonded to PVC foam core

Signal wires connecting the strain gages with the data acquisition system were run through 6.4mm wide channels machined in the foam core from the strain gages to the

corner of the panel. The wires exited the foam core through protective silicon tubing. The channels were routed at a depth near the neutral axis of the sandwich panel to reduce strain in the wires during panel bending. Once the wires were positioned, all channels were covered with filler pieces routed out of the same H250 foam. The wires, filler pieces and tubing were bonded to the core with the wires running out of the corner of the foam core, Figure 3-9.

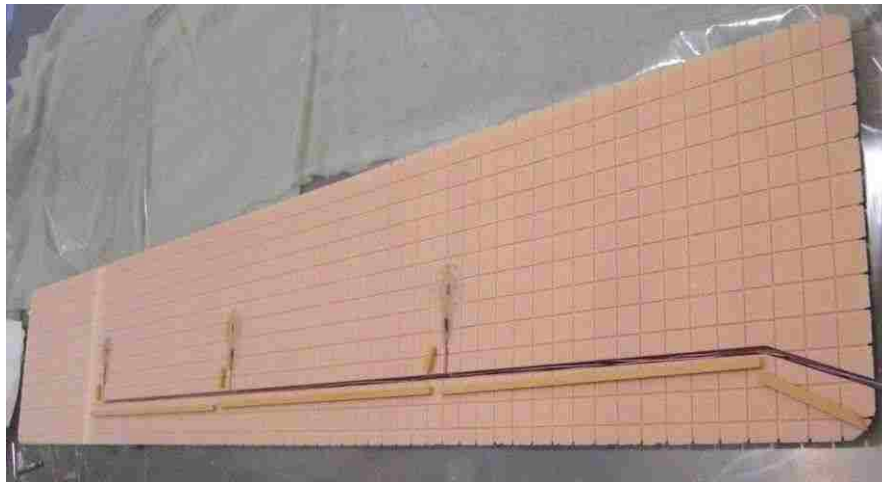


Figure 3-9: Wires routed through the channels to the edge of the foam core and through the protective tubing.

All bottom sandwich panels were manufactured on curved-surface molds, which are lightweight, inexpensive and compatible with vinyl ester. These molds were manufactured using a CNC router to cut Styrofoam undersized, which was then coated with epoxy tooling paste and CNC routed when cured. After the finished surfaces of tooling paste on the mold were sealed with a thin coat of epoxy, the sandwich panels were laid up.

To allow for analysis and comparison of bottom panel layups, a variety of layups were used on the 10 panels, see Table 3-1. The panels differed in material, layer count and fiber orientation. For example the port bottom panel in Bay 1 was manufactured as follows: three layers of DB240 glass fiber reinforcement for the outer (flat) sandwich skin were placed on the mold. All fibers were laid at $\pm 45^\circ$, where the 0° direction was parallel with the keel of the boat. The foam was placed on the fiber reinforcements with the beveled side up. Two layers of DB240 were laid on top of the foam with the same layup orientation as the first three layers. Two layers of DB240 reinforcement strips were laid along the four edges of the foam, also with the fibers at $\pm 45^\circ$. All panels were vacuum infused with vinyl ester resin and left under vacuum to cure at room temperature for 24 hours before demolding.

Table 3-1: Bottom panel layup details

	Port	Starboard
Bay 1	DB240 ($\pm 45^\circ$) 2 top layers Foam core 3 bottom layers 0° parallel	DB240 ($\pm 45^\circ$) 2 top layers Foam core 3 bottom layers 0° parallel
Bay 2	DBL700($0^\circ, \pm 45^\circ$) 2 top layers Foam core 3 bottom layers 1 layer L(X) 440-C10 (0°) 0° perpendicular	DBL700($0^\circ, \pm 45^\circ$) 2 top layers Foam core 3 bottom layers 1 layer L(X) 440-C10 (0°) 0° parallel
Bay 3	DBL700 ($0^\circ, \pm 45^\circ$) 2 top layers Foam core 3 bottom layers 1 layer L(X) 440-C10 (0°) 0° perpendicular	DB240 ($\pm 45^\circ$) 2 top layers Foam core 3 bottom layers 1 layer L(X) 440-C10 (0°) 0° parallel
Bay 4	DBL700($0^\circ, \pm 45^\circ$) 2 top layers Foam core 3 bottom layers 1 layer L(X) 440-C10 (0°) 0° parallel	DBL700($0^\circ, \pm 45^\circ$) 2 top layers Foam core 3 bottom layers 1 layer L(X) 440-C10 (0°) 0° perpendicular
Bay 5	DBL700($0^\circ, \pm 45^\circ$) 2 top layers Foam core 3 bottom layers 0° perpendicular	DBL700($0^\circ, \pm 45^\circ$) 2 top layers Foam core 3 bottom layers 0° parallel

3.2.3 Bulkhead Panel Analysis, Design and Construction

When the boat operates in severe sea conditions at a high speed, high loads will be transferred from hull panels into the keel, chine and longeron, then into the lower bulkheads and freeboards. The loads transferred into the lower bulkheads are then transferred into the upper bulkheads and then into the freeboards. The FE analysis shows that the upper bulkheads are subjected to significant stresses which could cause damages to the structure. Composite bulkhead panels were designed and manufactured in order to improve the strength of the structure.

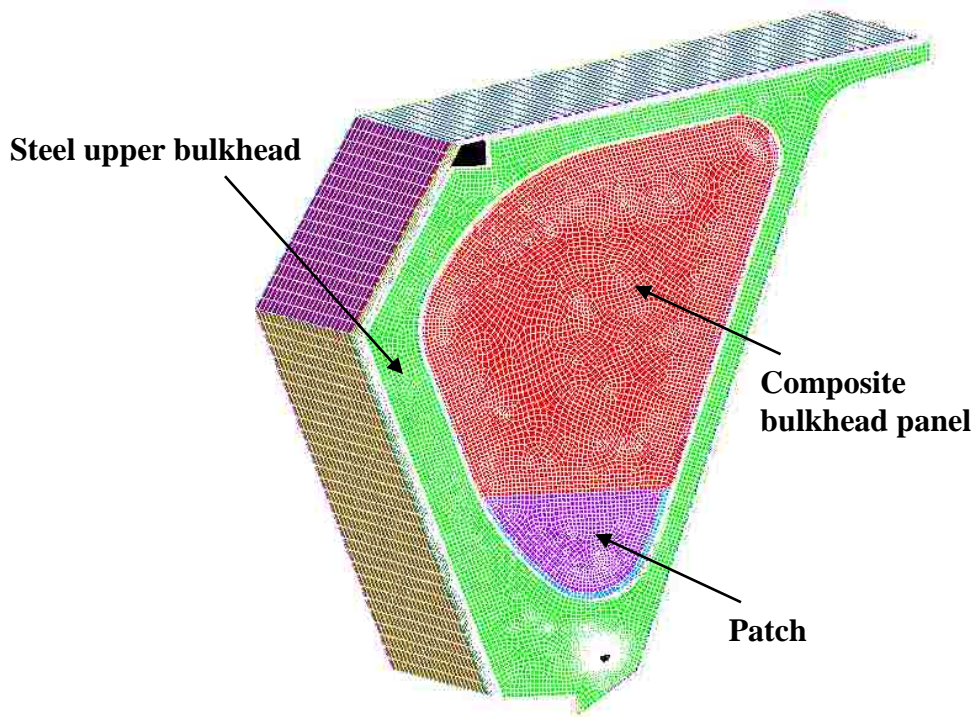


Figure 3-10: Finite element model of the composite panel in the upper bulkhead.

The design of the carbon fiber bulkhead panel is based on the FE model analysis, Figure 3-10. The model was built in ANSYS. Shell elements were used exclusively, with sandwich shell elements used for the sandwich panels. The load introduction was simulated in the FE model by placing a point force at the center of a stiff plug located in the mounting lug. Since the lower part of the bulkhead was the high stress area, a composite patch was designed to improve the strength of that local structure without increasing the weight of the whole panel unduly. Considering that the composite material is anisotropic, different combinations of the fiber orientation were tested in the FE analysis in order to optimize the design of the panel. A buckling analysis was also performed with this FE model. The resulting stresses in the steel upper bulkhead panel, Figure 3-11, were greatly reduced (in comparison with the model without the composite reinforcement panel).

Only one kind of fabric, the carbon fiber reinforcement Hexell 282, was used to build the composite bulkhead panels. The layup of bulkhead panels is listed as following: one patch layer at 65 degrees, one patch layer at 45 degrees, then one complete layer at 65 degrees and another complete layer at 45 degrees. This made up one skin. A Divinycell H100 foam core from Diab with the thickness of 9.5mm (9.5mm H100 for all bulkheads except for the bulkheads next to the firewall which are built with 12.7 mm H80) was placed on top, and then another skin identical to the first one but mirrored. Two reinforcing layers were placed around the edge of the foam core.

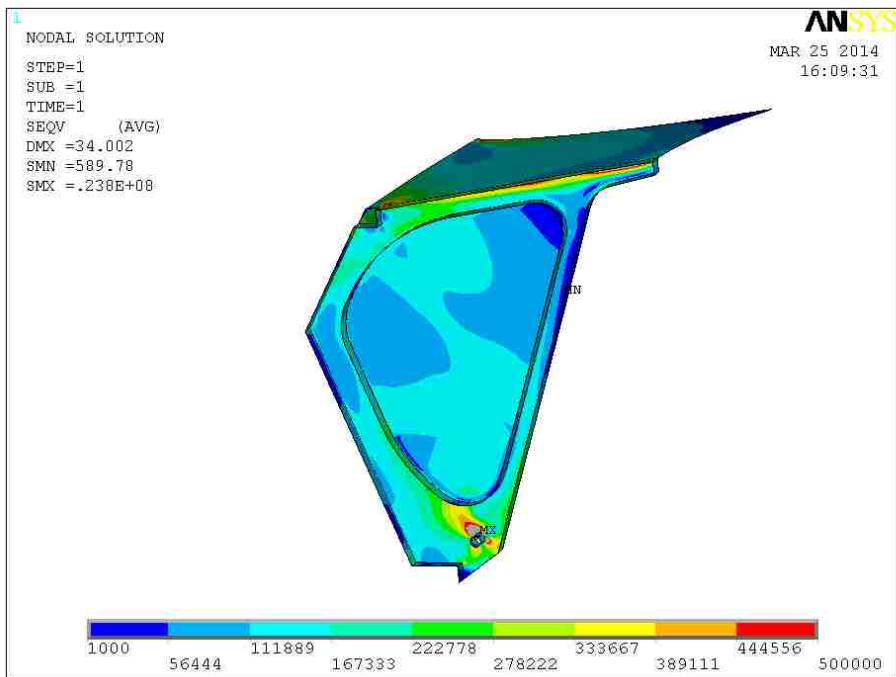


Figure 3-11: Resulting von Mises stress in the steel upper bulkhead.



Figure 3-12: Demolded composite bulkhead panel and the bonded panel

An example of a demolded panel and an installed panel are shown in the Figure 3-12. Twelve similar composite bulkhead panels were made.

Additionally, a collision composite bulkhead panel and a firewall panel were designed and manufactured. The manufacturing of the collision bulkhead panel and the installed panel are shown in Figure 3-13. Three stiffener beams were designed and co-infused with the panel. An opening was left for access and a hatch was designed and made to cover it.



Figure 3-13: Manufacturing of the collision bulkhead panel and the panel installed

3.3 Composite Panel Bonding

All composite panels were bonded to the stainless steel truss with ProSet 176/276 epoxy adhesive. Bonding strength tests were carried out on a MTI modified Instron universal test machine to ensure sufficient bonding strength between the steel truss and the composite panels. The bonding area on the outside steel frame is about 40mm wide.

Bonding surface preparation is very important for the joint's performance. The stainless steel bonding surface was sanded with sanding discs on a heavy duty grinder, thoroughly cleaned with acetone, and then silane treated before bonding. The panel bonding surface was also carefully sanded using different grit size sand papers and then solvent cleaned. ProSet 176/276 toughened epoxy adhesive was used to bond the panels to the steel truss. The epoxy adhesive was applied, using a pneumatic gun with a static mixing nozzle, to the steel truss and the panel and evenly spread over the bonding surfaces. An extra bead of epoxy was applied down the middle of the bonding surface to assure a sufficient bond line thickness and to make sure excess epoxy forced out any air when the panel was mounted to the truss. bulkhead panels were bonded to the truss first, Figure 3-14.



Figure 3-14: Assembly of bulkhead panels and side panels

Then freeboard panels and deck panels were installed on the steel truss. They were fixed with wood pieces and clamps, Figure 3-15. After the epoxy was sufficiently cured between the panel and steel truss, the fixture and adhesives remaining on the truss were removed.



Figure 3-15: Bonding of a side panel

In order to fit the curvature of the boat, flat freeboard panels and deck panels have to be bent before bonding. The inner side of the panels was scored and strip of the inner skin was removed to allow bending, Figure 3-16. After the panel was bonded, a reinforcement fiber cloth was wet laminated to the inner surface. The resin was squeegeed into the reinforcement fiber cloth between clear plastic films, then transferred to the sandwich panels and rolled onto them. Usually a peel ply is put on top of the cloth. An example is shown in Figure 3-17.



Figure 3-16: Scores on the inner side of a bonded side panel.



Figure 3-17: Reinforcement fiber cloth wet laminated to a panel.

After all bulkhead panels, freeboard panels and deck panels were installed, the hull was lifted and turned upside down using a rotisserie, Figure 3-18. Then the bottom panels were bonded to the steel truss one by one and in a similar manner to the freeboard panels.



Figure 3-18: The hull before and after rotation.

When all composite panels were bonded to the steel truss and the engine mounting, stern drive mounting and the cockpit installations were finished, the main structure of the steel/composite hybrid slamming test boat was complete.

Chapter 4. Steel/Composite Hybrid Boat Test

Paper: Hydrodynamic Responses of Composite Hull Panels Subjected to Atlantic Slamming Loads

Robert Thodal, Joachim L. Grenestedt, Jian Lv

Abstract: The highest loads on bottoms of fast craft are due to slamming, or hydrodynamic impact. Slamming is not only affected by bottom geometry, speeds, and wave shapes, but also by hydro-elastic effects. In order to study slamming an instrumented slamming load test facility was designed and built. The facility loosely resembles a dedicated high-speed offshore boat, but it has a faceted hull consisting of ten separate bottom panels, each with a unique construction. At the same lengthwise location, bottom panels on starboard and port have different layups, thicknesses, fibers, etc. After over 30 hours running in calm water and rough water, the strain data recorded from panel embedded strain gauges was collected and analyzed. The results demonstrate some of the effects that composite bottom panel stiffness has on slamming loads.

4.1 Introduction

Slamming impact is an important phenomenon in high-speed ship and ocean engineering. Slamming can result in large transient hydrodynamic impact loads on the

hull, leading to violent motions, onboard equipment damage, and even local structural damage. Hence, slamming loads are very important in the structural design of all high-speed vessels and need to be investigated.

Pioneering research on hydroelasticity in panel-water impacts was started with the work of von Karman in 1929. The research that followed can be categorized as theoretical, numerical or experimental studies. Many effective theoretical methods based on a solid background of experimental data were developed decades ago, e.g. Savitsky and Allen. The recent fundamental theoretical and experimental work presented by Faltinsen, Kvalsvold and Haugen have investigated wave impact on horizontal or nearly horizontal one-beam and three-beam models. A review of some of the major developments can be found in Faltinsen. Numerical modeling research work presented recently has utilized non-linear boundary element methods, computational fluid dynamics and explicit finite element analysis.

Experimental research is also well-reported in the literature. Many of these experiments involve vessel drop tests. Most of these drop test experiments have used essentially rigid models to investigate slamming pressure distributions. The water entry velocity of the hull in vessel experiments was primarily controlled by the drop height and the mass of the specimen. However when a drop test specimen hits the water, it is difficult to control the hull motion in a way that accurately simulates real vessel slamming. Considering that the velocity, pressure, and strain profiles depend on the overall behavior of the vessel and the position of the panel, the real vessel test is regarded as an

integral part of hydrodynamic slamming studies. Some efforts at tests with real vessels have been presented during the past decades, but this type of testing has not been overly comprehensive and remains an open area today.

Experiments performed by Battley have made use of a Servo-hydraulic Slamming Testing System (SSTS) to allow for tests with control of panel velocity profiles. Experiments have been conducted for a variety of deadrise angles, velocity profiles, and panel construction. Panels have been tested that range from extremely soft to effectively rigid.

Stenius identified a dynamic hydroelastic parameter to characterize the relation between the loading rate and wetted natural frequency of a panel. Impacts with a loading rate lower than the wetted natural frequency are expected to result in a quasi-static response while impacts with a greater loading rate show hydroelastic effects. Simulations and experiments on the SSTS have demonstrated the increasing role of these hydroelastic effects at high loading rates. These efforts have been successful in characterizing the behavior of panels subjected to simulated slamming loads but it is unclear if these loads provide a complete and representative spectrum of real vessel slamming.

Lv and Grenestedt have recently completed an analytical study of the response of hull bottom panels to slamming loads. Slamming loads were modelled as a high intensity peak followed by a lower intensity residual pressure moving across the panel at a constant speed. Hydroelastic effects were ignored, or included only as a constant added

mass term. The structural response during the initial loading phase and a later vibration phase were investigated for a variety of loads and panel properties. Lv and Grenestedt identify a critical range of non-dimension loading rates where the structural response is greatest.

In order to accumulate valuable test data to describe the characteristics of vessel water slamming and investigate this phenomenon more comprehensively, an instrumented slamming load test facility was designed, built and tested in a variety of sea states. Strain data from strain gages embedded in bottom composite sandwich panels and on the ship's steel frame were collected by an onboard data acquisition system. Together with video and acceleration data recorded during testing, the strain data is analyzed in this paper.

4.2 Instrumented Slamming Load Test Facility

A 9 meter long, 1.9 meter wide hybrid slamming load test facility boat was designed and manufactured by Grenestedt, Figure 4-1. This hybrid boat was made with a welded non-magnetic AL-6XN stainless steel frame and composite sandwich panels. The stainless steel used is 2mm thick. The composite panels including 10 bottom panels, 10 side panels, 5 deck panels, 16 bulkhead panels and 4 hatches were manufactured with the vacuum infusion method. Carbon fiber, glass fiber, PVC foam core, epoxy and vinyl ester resin were used during the panel manufacturing process.



Figure 4-1: Slamming load test facility boat

All side panels share a common layup. The outer skin consists of one layer of TC-18-N carbon fiber (0° , 90°) by JB Martin and one layer of Hexcel 7725 glass fiber ($\pm 45^\circ$). The foam core is Divinycell H80 with a thickness of 12.7mm. The inner skin of these panels was made from one layer of DB240 glass fiber ($\pm 45^\circ$). The 0° direction of all fabrics was parallel with the keel of the boat. On the top of the inner skin, two layers of DB240 reinforcement strips were laid along the edges of the foam. The layup of every bottom panel was different to allow for comparison and better understanding of stiffness effects on slamming. More details are presented in the following section. All composite panels were bonded to the steel frame with Proset 176/276 epoxy. The bonding area on the outside steel frame is approximately 40mm wide. Bonded specimen tensile tests

showed that the bonding shear strength completely fulfilled the design requirements. Operation has also proven this.

This test boat can accommodate two passengers and has a full load displacement of 2450kg. The top speed achieved during the tests with the installed 425 HP Mercury V8 engine was 27 m/s. After well over 30 hours of running in a variety of sea conditions, the structural integrity was maintained. No damage or plastic deformation was found. The data acquisition system functioned normally and a large accumulation of test data was acquired.

4.3 Bottom Construction

The bottom panels are Fiber-reinforced plastic (FRP) sandwich panels manufactured by vacuum infusing Ashland 8084 vinyl ester resin into thin glass fiber or carbon fiber skins on each side of a polymer foam core. All foam cores of the bottom panels are 18-mm-thick Divinycell H250 foam with infusion grooves on both sides. The foam cores were routed slightly smaller than the opening in the steel frame and the edges were beveled 30°. The skins come together at the end of the foam core where the panel was bonded to the steel frame.

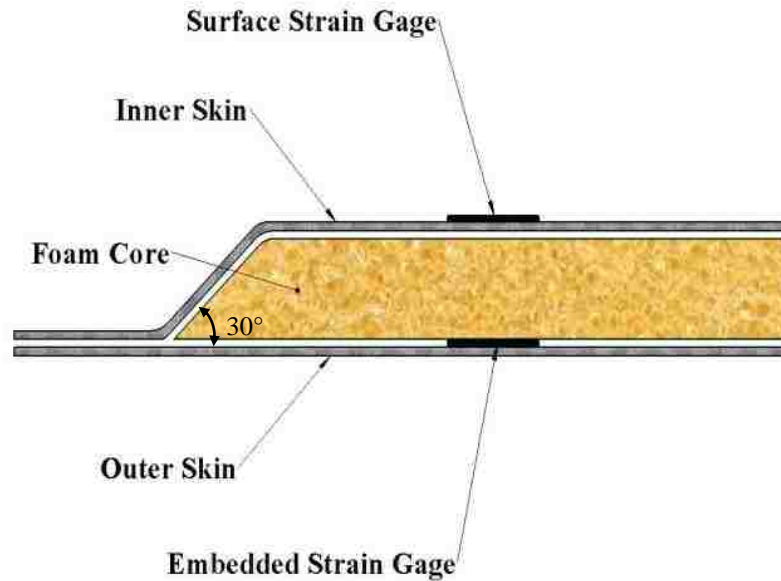


Figure 4-2: Composite sandwich panel with strain gages

In the present research, the strains on the outer skin of the bottom panels were measured. The strain gages could not be attached to the outer skin using traditional methods due to the harsh environment and the requirement that the hull be hydrodynamic smooth, so foil strain gages were embedded in the bottom panels, Figure 4-2. Foil strain gages by Vishay Inc. were located on the outer surface of the foam core. The strain gages were bonded to flat thin fiberglass plates. The plates were made of a single layer of Hexcel 7725 glass fiber fabric infused with vinyl ester, and cut into Paddle-like shapes. Figure 4-3 shows the paddle bonded to the foam core. The leads of the strain gages were set in a zigzag pattern to protect them from potential damage under high strains. The paddles were aligned and bonded in place using 3M's DP 125 two part epoxy. Signal wires connecting the strain gages with the data acquisition

system were run through 6.4mm wide channels machined in the foam core from the strain gages to the edge of the panel. The wires exited the foam core through protective silicone tubing. The channels were routed at a depth near the neutral axis of the sandwich panel to reduce strain in the wires during panel bending. Once the wires were positioned, all channels were covered with filler pieces routed out of the same H250 foam. The wires, filler pieces and tubing were bonded to the core with the wires running out of the corner of the foam core.

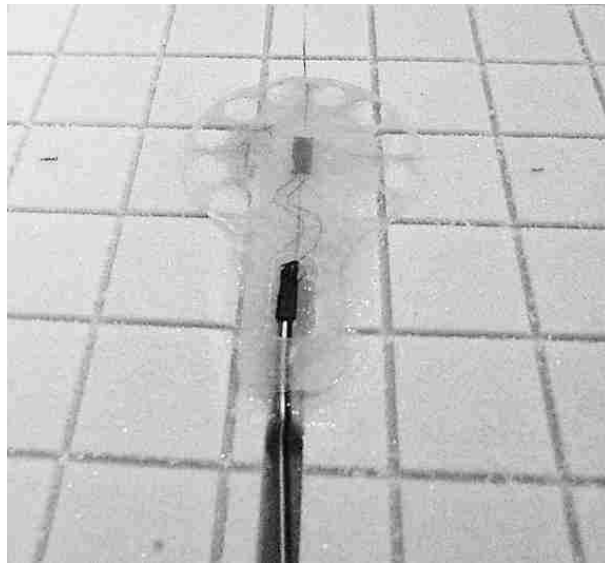


Figure 4-3: Strain gage paddles bonded to PVC foam core

All bottom sandwich panels were manufactured on curved-surface molds, which were lightweight, inexpensive and compatible with vinyl ester. These molds were manufactured using a CNC router to cut Styrofoam billets undersized, which were then coated with epoxy tooling paste and CNC routed when cured. The finished surfaces of

tooling paste on the mold were sealed with a very thin coat of epoxy and the sandwich panels were laid up.

To allow for analysis and comparison of bottom panel layups, a variety of layups were used on the 10 panels, Table 4-1. These panels differed in material, layer count and fiber orientation. For example the port bottom panel in Bay 1 was manufactured as follows. Three layers of DB240 glass fiber reinforcement for the outer (flat) sandwich skin were placed on the mold. All fibers were laid at $\pm 45^\circ$, where the 0° direction was parallel with the keel of the boat. The foam was placed on the fiber reinforcements with the beveled side up. Two layers of DB240 were laid on top of the foam with the same layup orientation as the first three layers. Two layers of DB240 reinforcement strips were laid along the four edges of the foam, also with the fibers at $\pm 45^\circ$. All panels were vacuum infused with vinyl ester resin and left under vacuum to cure at room temperature for 24 hours before demolding.

Table 4-1: Bottom panel layup details

	Port	Starboard
Bay 1	DB240 ($\pm 45^\circ$) 2 top layers Foam core 3 bottom layers 0° parallel	DB240 ($\pm 45^\circ$) 2 top layers Foam core 3 bottom layers 0° parallel
Bay 2	DBL700(0°, $\pm 45^\circ$) 2 top layers Foam core 3 bottom layers 1 layer L(X) 440-C10 (0°) 0° perpendicular	DBL700(0°, $\pm 45^\circ$) 2 top layers Foam core 3 bottom layers 1 layer L(X) 440-C10 (0°) 0° parallel
Bay 3	DBL700 (0°, $\pm 45^\circ$) 2 top layers Foam core 3 bottom layers 1 layer L(X) 440-C10 (0°) 0° perpendicular	DB240 ($\pm 45^\circ$) 2 top layers Foam core 3 bottom layers 1 layer L(X) 440-C10 (0°) 0° parallel
Bay 4	DBL700(0°, $\pm 45^\circ$) 2 top layers Foam core 3 bottom layers 1 layer L(X) 440-C10 (0°) 0° parallel	DBL700(0°, $\pm 45^\circ$) 2 top layers Foam core 3 bottom layers 1 layer L(X) 440-C10 (0°) 0° perpendicular
Bay 5	DBL700(0°, $\pm 45^\circ$) 2 top layers Foam core 3 bottom layers 0° perpendicular	DBL700(0°, $\pm 45^\circ$) 2 top layers Foam core 3 bottom layers 0° parallel

4.4 Instrumentation and Data Acquisition

The composite bottom panels and stainless steel structure in bays 2, 3 and 4 of the slamming load test facility were instrumented with a total of 123 strain gages. The gages used were Vishay C2A-13-250LW-350, CEA-06-250UT-350/P2 or CEA-06-250UN-350/P2. On the bottom panels gages were installed on both the inner skins and embedded on the outer skins. On bay 2 bottom panels all gages were linear (single axis) type oriented in the transverse direction. On bay 3 and 4 bottom panels a combination of linear and t-rosette gages were used where all linear gages were oriented transverse and t-rosettes oriented to give transverse and longitudinal strain. The gages on the steel structure in bays 2, 3, and 4 were all linear oriented longitudinally (parallel to the keel). These gages were installed on the keel, chine longerons, deck longerons and the top and bottom flange of the main longerons. Figure 4-4 shows the locations and orientations of gages on the bottom panels. Figure 4-5 shows the locations of gages on the steel structure.

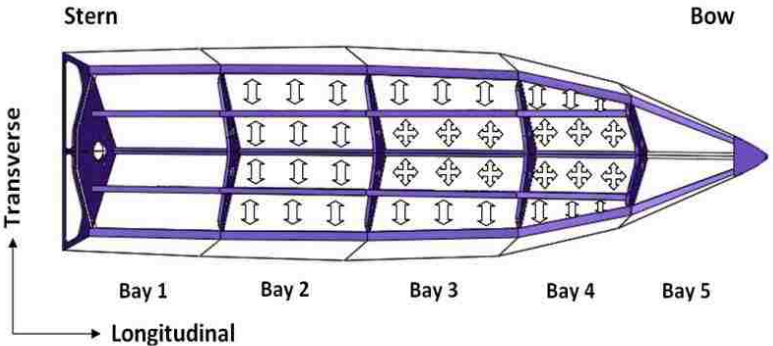


Figure 4-4: Bottom panel strain gage locations and orientations

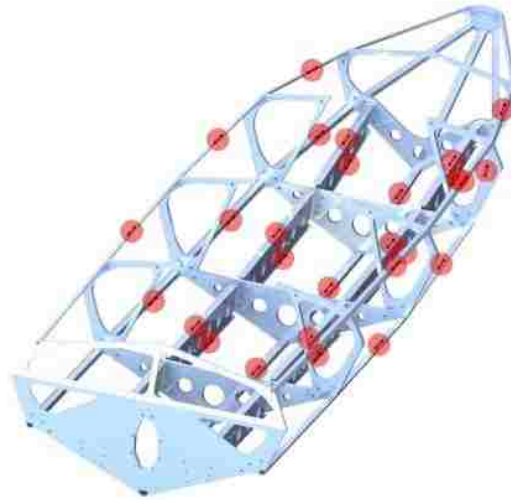


Figure 4-5: Steel structure strain gage locations

Strain gage signal conditioning was performed by National Instruments 9237 4 channel compact DAQ modules. A total of 39 modules were installed in five compact DAQ chassis. This allows for up to 156 strain channels to be simultaneously sampled at up to 50 kHz per channel with 24 bit precision. Accelerometer signal conditioning includes three National Instruments PXI-4472B modules to simultaneously measure up to 24 channels of IEPE type accelerometers at up to 102.4 kHz per channel with 24 bit resolution.

A compact DAQ 9401 digital I/O module was used as a master timing controller to synchronize the five compact DAQ chassis and the PXI chassis. A National Instruments PXI-8110 controller running a custom labview program was used to record the data onto solid state disks. Inertial data from a VectorNav VN-200 inertial navigation system

synchronized to the PXI and compact DAQ system was also recorded. Figure 4-6 shows the enclosure housing the PXI instruments, and Figure 4-7 shows the enclosure housing the compact DAQ instruments.



Figure 4-6: PXI Instrumentation

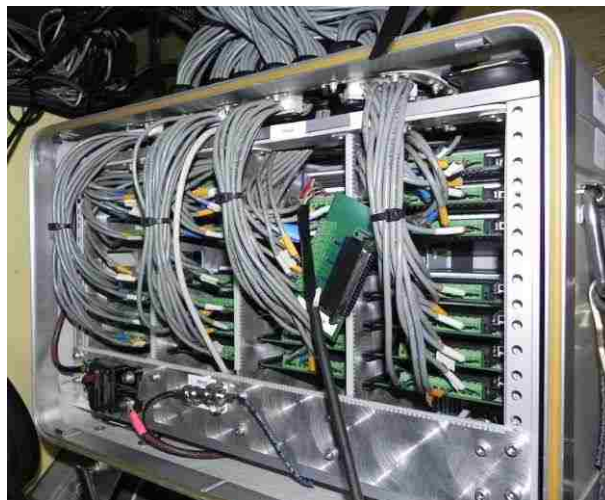


Figure 4-7: Compact DAQ Instrumentation

4.5 Experimental Methodology

Static Panel Stiffness Testing

Tests were performed in the lab to determine the displacement of the various bottom panels to known loads. A fixture was created consisting of an aluminum beam with a sliding carriage mounted to a Transducer Techniques LPU-1k load cell. The fixture is shown in Figure 4-8. The load cell is mounted on a spherical bearing and has a 76mm diameter pad attached to the load button. Load was introduced to the bottom panel through the pad by applying a force to the aluminum beam. Displacement at the inner skin of the panel was measured with six Omega LD320-15 LVDTs mounted to a frame between the keel and main longeron as shown in Figure 4-9. Load was introduced at a number of points on the bottom panels as defined by the grid shown in Figure 4-10. Load was applied gradually until a maximum of approximately 1000 Newtons was reached, then slowly released. Data was sampled at 1667 Hz, the minimum supported by the NI-9237 module used for load cell signal conditioning.



Figure 4-8: Static load test fixture



Figure 4-9: LVDTs mounted for static load tests

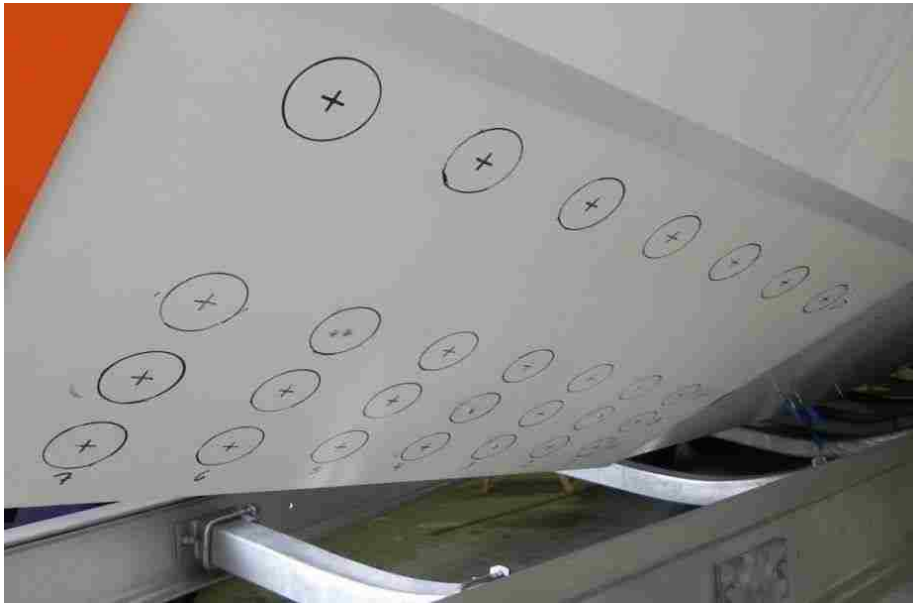


Figure 4-10: Static load test grid

Dry Modal Testing

In order to determine the resonant frequencies of the bottom panels, a test was devised to excite the panels and measure their response. The panel of interest was instrumented on the inner skin with a PCB Piezotronics model 352c04 +/- 500g accelerometer with a -3 dB frequency range of 0.5 Hz to 10 kHz. The accelerometer was screw mounted to an aluminum base bonded to the inner surface of the panel with a cyanoacrylate adhesive. A PCB piezotronics 086D05 22kN (5klbf) peak force impact hammer equipped with a medium stiffness impact cap (white) and vinyl cover was used to excite the structure and record the load spectra. Accelerations and load were recorded at 5 kHz per channel with a PXI-4472B module signal conditioner.

Sea Trials

The data presented here was collected on September 24, 2013 off the coast of Point Barnegat Light, NJ. The closest wave buoy was the National Oceanic and Atmospheric Administration's NDBC Station 44066. At the time of the test, the significant wave height was 0.6m indicating sea state 3 conditions. Figure 4-11 shows a view of the sea conditions during testing.



Figure 4-11: Sea conditions encountered during Atlantic tests

The test procedure involved performing 5-10 minute long sustained data logging sessions at speeds up to 27 m/s. Data from 110 strain channels and 22 acceleration channels were recorded at 50 kHz per channel, while inertial navigation solutions were recorded at 40 Hz. Strain gages were located on the steel frame structure and the

composite bottom panels. PCB 354C03 +/-50g triaxial accelerometers were fixed to the steel structure at bulkhead 2 and 5 to capture rigid body motion. Higher range PCB 352C04 +/-500g single axis accelerometers were located on composite bottom panels. At the start of each test, the strain signals were zeroed while the boat was stopped. After logging was started the boat accelerated to the maximum safe speed in a head sea and then slowly turned to ultimately make a full orbit and return to the starting location. Effort was made to maintain a neutral roll angle for the duration of the test.

4.6 Data Analysis

Static Panel Stiffness Testing

Static displacement data was collected for each of the boat bottom panels. Load was applied at 21 locations on each panel, with the resulting displacement recorded at six different locations along with the load. Linear regression was performed between each displacement and the load to produce a function expressing the displacement at a given location per unit load applied at each of the 21 grid points. Linear combinations of the resulting functions can be used to estimate the displacement due to a distributed load over the panel. The linear combination of all 21 grid points was taken to approximate a hydrostatic pressure on the panel. The result of this data reduction is a value for displacement at each of the 6 LVDT locations for an evenly distributed pressure on the panel. By taking the ratio of these displacements between a starboard and port panel, the relative stiffness of the panels was determined.

Dry Eigenfrequency Identification

The least squares complex exponential modal analysis method was used to identify the panel modes from experimental data. Each panel was excited in multiple locations by the impact hammer and the response recorded by an accelerometer at a fixed location. See Appendix D for more details on the least squares method.

Sea Trials

A variety of methods were used to reduce the data from the sea trials. The first efforts made were to characterize the slamming events from strain response in the time domain. The slamming rise time was determined by calculating the time between zero strain and maximum strain during a slamming event. Additionally, the frequency of wave impacts was found by calculating the time between slamming events.

In order to compare the effect of different stiffnesses between the panels, two dimensional histogram plots were generated. The intensity of the color at a given position in the plot relates the probability of the corresponding strain levels in the port and starboard panels. Additionally, histograms were produced that indicate the probability of the indicated strain ratio between left and right panels from the experimental data.

Another method used to evaluate the relative response of the panels is calculation of a frequency quotient function. This function relates the Fourier transform of two signals.

These strain frequency quotient functions are generated using a method similar to those from modal testing. The H_1 , H_2 and H_v functions are defined below.

$$H_{x_1}(\omega) = \frac{S_{x_1}(\omega)}{S_{x_1}(\omega)}$$

$$H_{x_2}(\omega) = \frac{S_{x_2}(\omega)}{S_{x_2}(\omega)}$$

$$H_v(\omega) = \sqrt{H_{x_1}(\omega) H_{x_2}(\omega)}$$

Where $S_{x_1}(\omega)$ is the autospectral density function of x and $S_{x_2}(\omega)$ is the cross power spectral density of $x(t)$ and $y(t)$.

The coherence function between two signals is an indicator of their correlation. A perfect coherence of 1 at a given frequency indicates there is a linear relation between the two at the indicated frequency whereas a coherence of zero indicates they are not correlated. The coherence function is defined below.

$$C_{xy}(\omega) = \frac{|S_{xy}(\omega)|^2}{S_{xx}(\omega) S_{yy}(\omega)}$$

The Hv frequency response function estimator is used for comparing strain signals because the two signals being related are of similar magnitude and noise content.

Wetted Eigenfrequency identification

The dynamic hydroelastic characterization factor used by Battley and Stenius is given as

$$M^* = \frac{4L}{\pi} \left(\frac{D}{\rho_w V} \right)^{1/2} \sqrt{1 + \frac{D}{\rho_w V} \frac{1}{b^2} \left(\frac{2\pi n L}{\omega} \right)^2}$$

where L is the deadrise, D is bending stiffness, ρ_w is water density, V is impact velocity, b is panel width, and α_n is a parameter related to the boundary conditions given as $\alpha_n = 1.875$ for simply supported boundaries and $\alpha_n = 4.730$ for clamped boundaries. Further, the first wetted natural period is given as

$$T_{w1} = \frac{2L}{\sqrt{D/m^*}} \sqrt{(1 + m^*/m)^{-1}}$$

Here m is the structural mass per unit length of the panel and m^* is added mass due to coupling of water. m^* is given as

$$\omega_{w,nc} = \sqrt{\frac{EI}{\mu_{w,nc}} \left(\frac{\pi}{L} \right)^2}$$

The factor $\mu_{w,nc}$ is an added mass scaling factor, $\mu_{w,c} = 1$ is used. An alternative approximation of the wetted natural frequencies is given by Lv as

$$\omega_{w,c} = \sqrt{\frac{EI}{\mu_{w,c}} \left(\frac{\pi}{L} \right)^2}$$

Where L is panel width, EI is the bending stiffness integrated over the panel cross section, and $\mu_{w,c}$ is mass per unit length of the panel including added water mass given as

$$\mu_{w,c} = \mu \left(1 + \frac{D}{EI} \right)$$

Here μ is the mass per unit length of just the panel, d is the panel width and k is a factor describing the degree of wetting of the panel ranging from $k=0$ (dry) to $k=1$ (fully submerged).

In both cases, the panel bending stiffness EI and D were chosen such that with no added water mass the first modal frequency matched the mode 1 results from the dry modal test experiments.

4.7 Results and Discussions

The results presented here are limited to data collected from the bottom panels in bay 3 and bay 4. The bay 4 panels are identical with exception of the orientation of the DBL700 carbon fiber reinforcement. In bay 3, the panels differ in the use of DB240 glass fiber on the starboard panel in place of DBL700 carbon on the port panel.

Static Panel Stiffness Tests

The ratios of displacements to static load between the port and starboard panels in bay 4 are shown in Figure 4-12. This figure shows the shape of the bay 4 panels and the location of relevant structure including the keel, chine, main longeron and bulkheads. The locations where displacements were measured and the displacement ratios between port and starboard are indicated by the arrows. The static displacement testing shows a consistent trend between the port and starboard panels in bay 4. The measurements from the six LVDT's at different locations indicate that the port panel displacement to a given load is on average 1.6 times that of the starboard panel. The lower stiffness in the port panel is anticipated due to the fiber orientation and panel shape. The section of the bay 4 panel between the keel and longeron is long and narrow, approximately 1400mm in length and 400mm wide. The 0 degree fibers are parallel to the keel in the port panel and perpendicular to the keel in the starboard panel. The fiber spanning the narrow width of the starboard panel results in high stiffness.

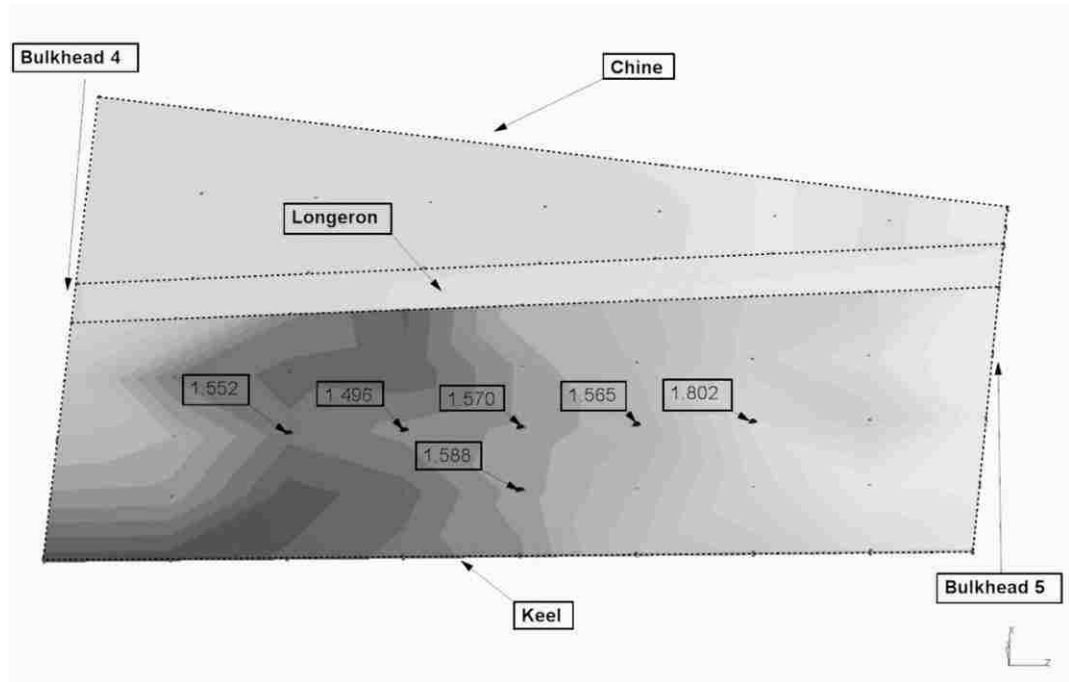


Figure 4-12: Bay 4 panel static stiffness ratios port/starboard

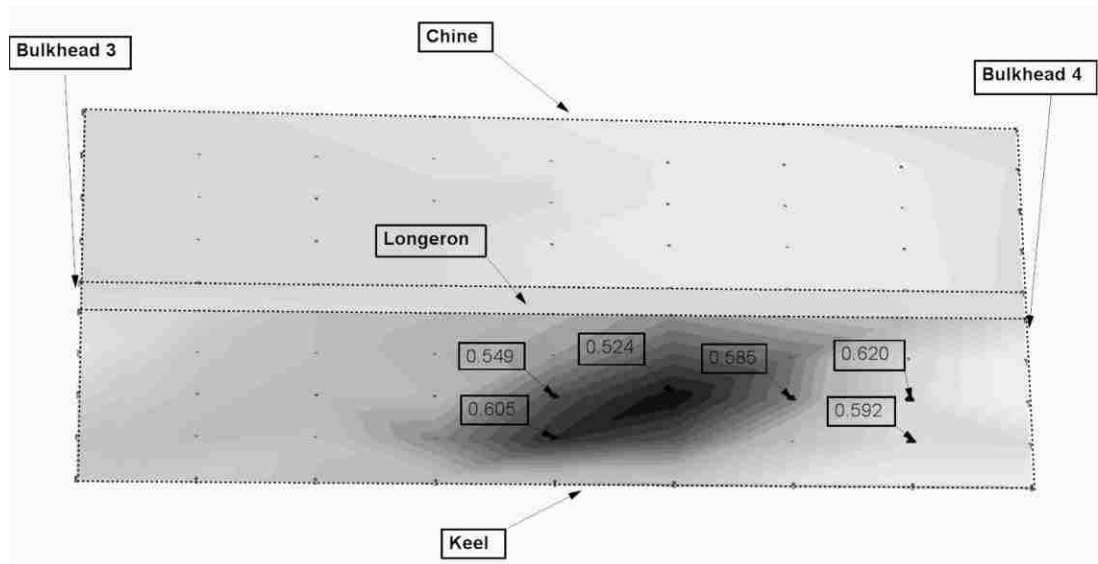


Figure 4-13: Bay 3 panel static stiffness ratios port/starboard

The results for static load testing of bay 3 are shown in Figure 4-13. These results indicate an average displacement ratio of 0.58 between the port and starboard panels. This is also an expected result due to the stiffer DBL700 triaxial carbon reinforcements in the port panel and the more compliant biaxial DB240 glass reinforcement in the starboard panel.

Dry Eigenfrequency Identification

Typical accelerance frequency response functions from experimental modal analysis for the port and starboard bay 4 panels are shown in figures Figure 4-14 and Figure 4-15. Synthesized FRFs from identified modes are also plotted.

The first mode of vibration is a longitudinal half sine wave deflection of the panel and longeron and quarter sine wave in the transverse direction. The next three modes are purely panel modes with no deflection of the main longeron. These modes have a single transverse half sine bending wave and one, two and three longitudinal bending half-waves respectively. Mode 4 consists of two transverse half sine waves and a single longitudinal bending wave. Table 4-2 summarizes the frequencies of these modes for the bay 4 panels.

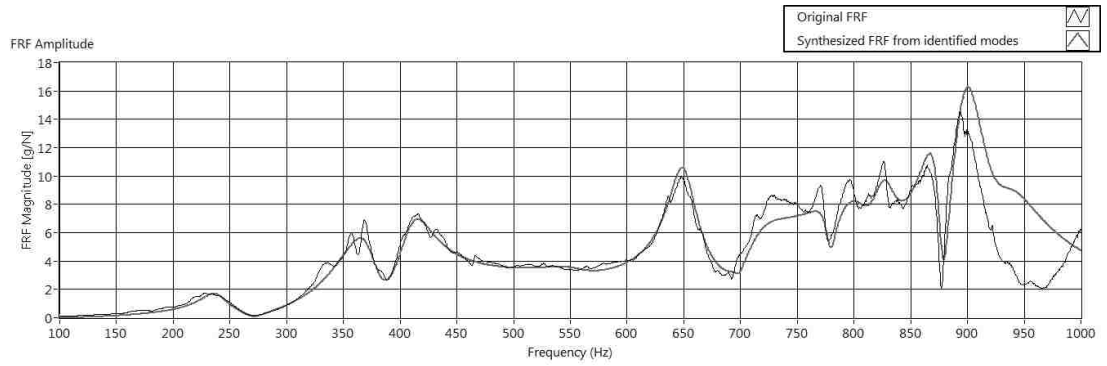


Figure 4-14: Bay 4 port acceleration FRF

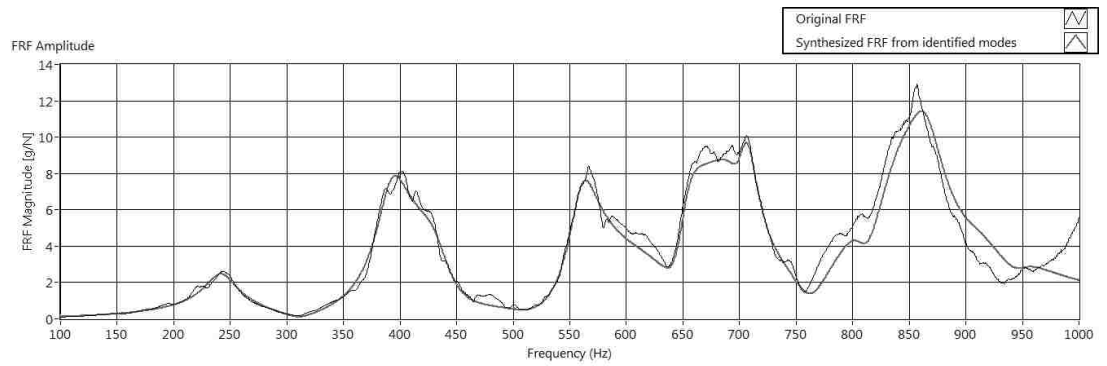


Figure 4-15: Bay 4 Starboard acceleration FRF

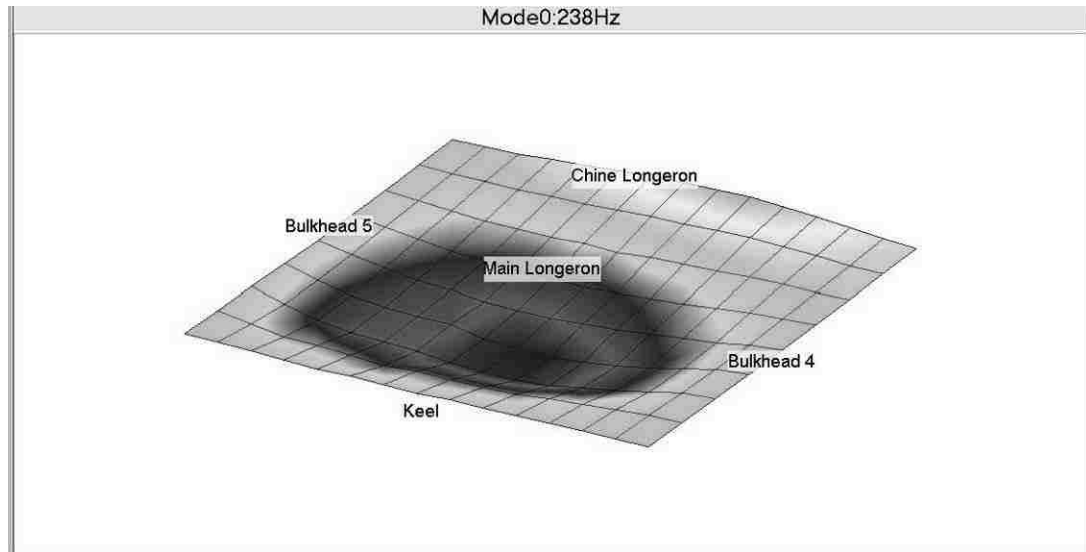


Figure 4-16: Bay 4 port panel mode 0

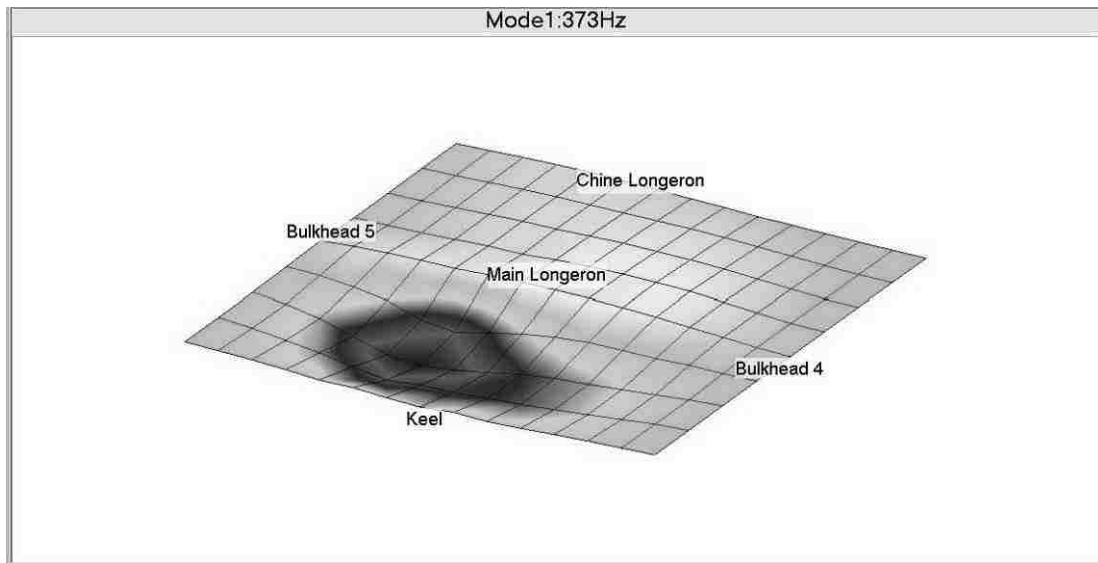


Figure 4-17: Bay 4 port panel mode 1

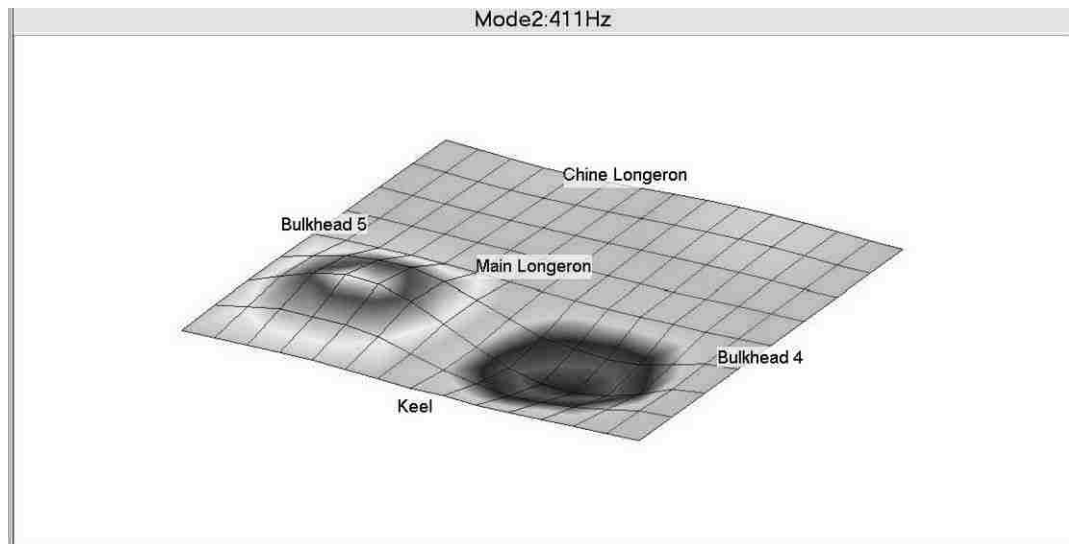


Figure 4-18: Bay 4 port panel mode 2

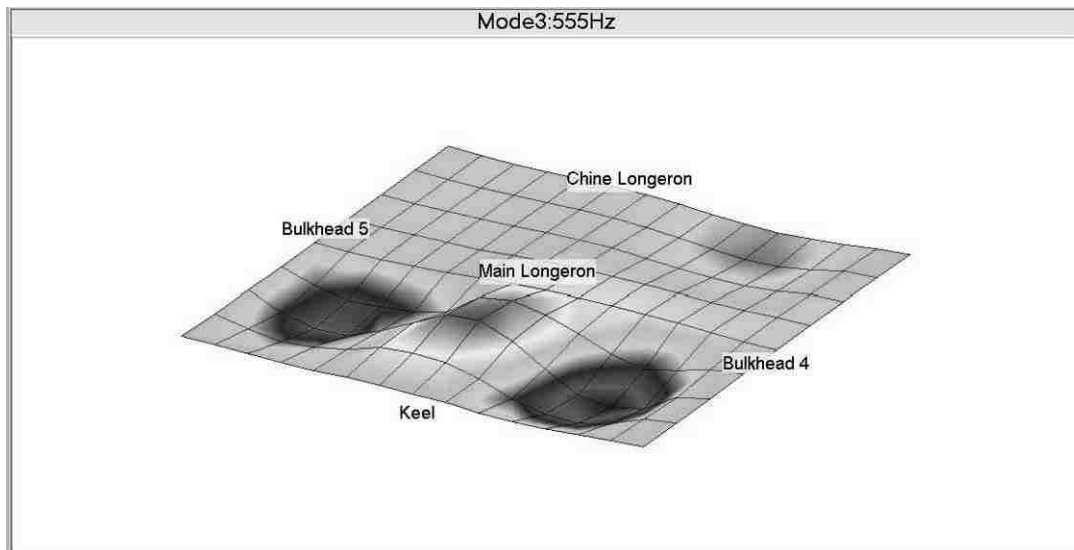


Figure 4-19: Bay 4 port panel mode 3

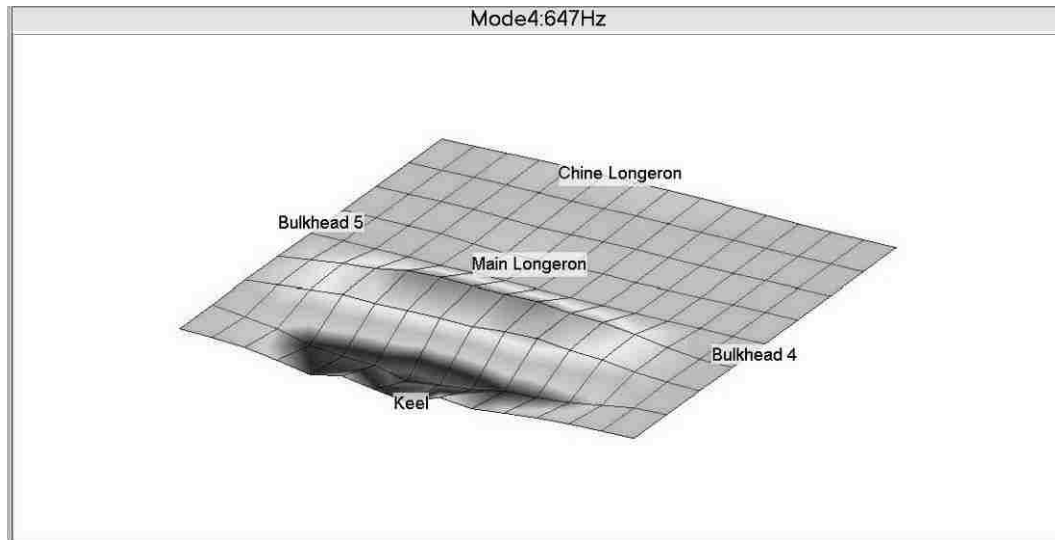


Figure 4-20: Bay 4 Port panel mode 4

Table 4-2: Bay 4 panel eigenfrequencies

	Bay 4 Port Panel	Bay 4 Starboard Panel
Mode 0 Frequency (Hz)	238	246
Mode 1 Frequency (Hz)	373	394
Mode 2 Frequency (Hz)	411	437
Mode 3 Frequency (Hz)	555	561
Mode 4 Frequency (Hz)	647	650

Sea Trial Testing Slamming Characterization

A typical strain gage time history from sea trials is shown in Figure 4-21. The peaks seen in the time history are individual slamming events. The time between these events is approximately 0.5-2.0 seconds.

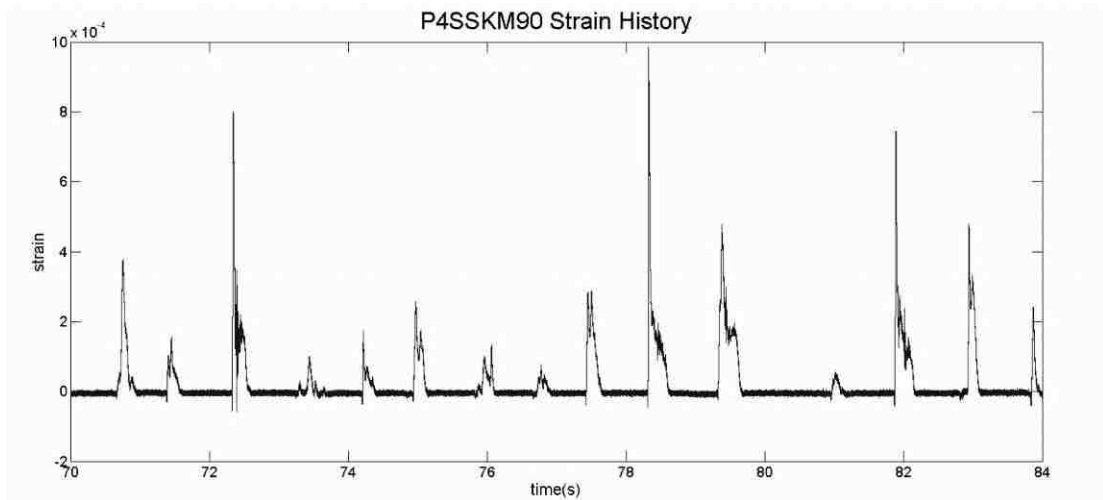


Figure 4-21: Typical strain gage time history for sea testing

An isolated slamming event is shown in Figure 4-22. The top plot shows 90 and 0 degree strain signals for the inner and outer skins on the port panel, while the bottom shows the response for the starboard panel. The strains on the inner skin are in tension, while the outer skin is in compression. The largest magnitude strains are seen on the inner skin in the 90 degree direction, followed by the outer skin 90 degree. The strains in the 0 degree direction are small compared to 90 degree strains and many of these results presented will focus on the behavior of the gages oriented in the 90 degree (transverse) direction.

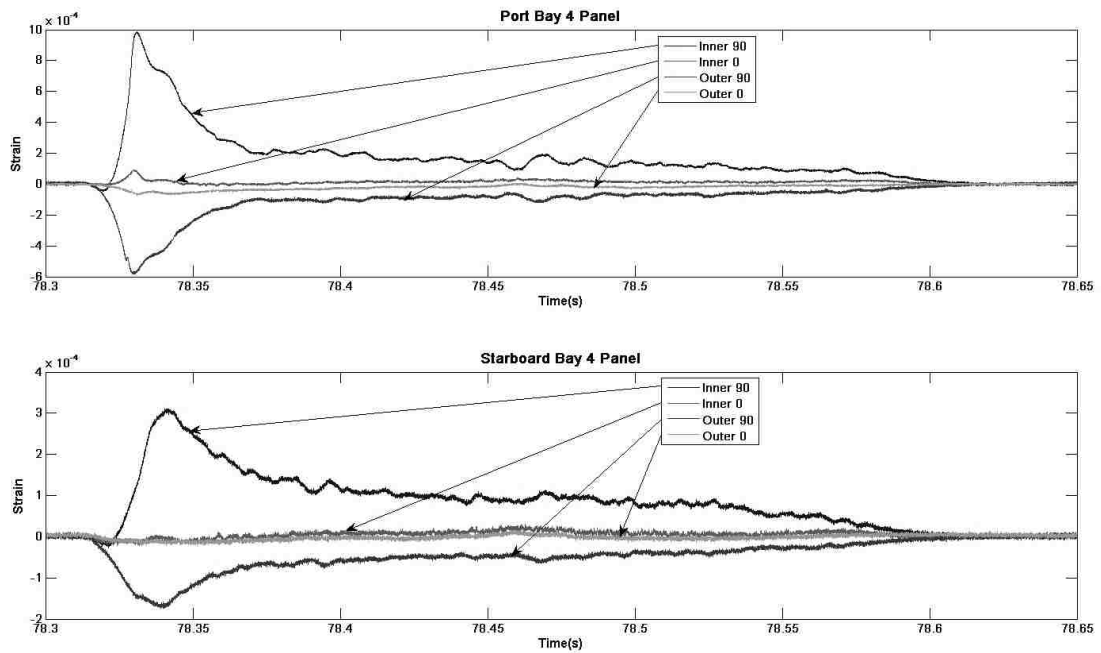


Figure 4-22: Strain response to single slamming event

These slamming events are characterized by a sharp rise to peak strain, then strain quickly drops off to a residual level and slowly decays to zero. In this case the initial rise time for the response is 10 ms, initial drop off takes 50ms after peak strain, and the duration of the decay to zero strain is an additional 200ms.

Figure 4-23 shows the ratio of strains between the port and starboard panels with time for this slamming event. At the time of the initial slamming peak the port panel has roughly three times the strain, but this quickly falls until the port strain is only 1.5 to 2 times the starboard strain.

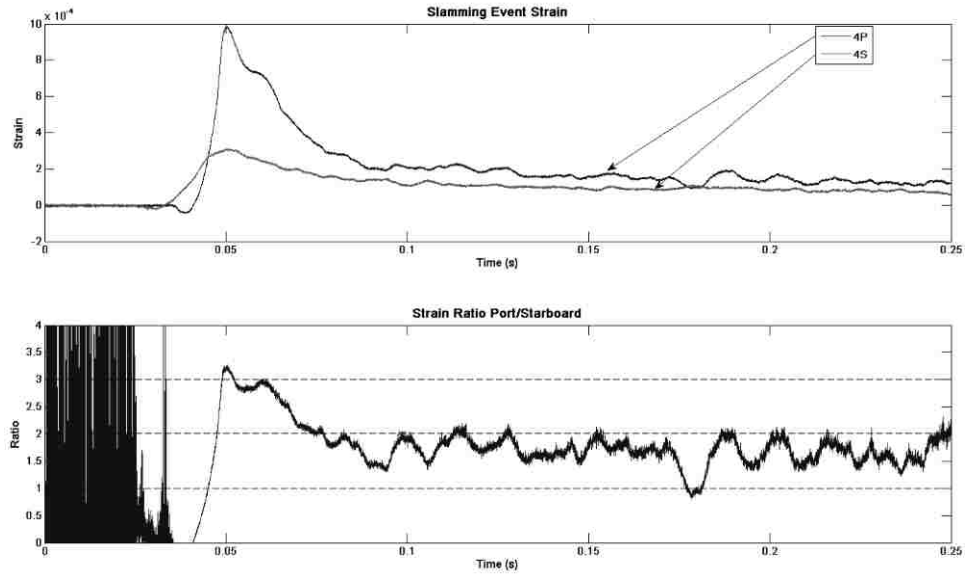


Figure 4-23: Slamming event bay 4 90 degree strains and port/starboard strain ratio

Peak Strains

Figure 4-24 and Figure 4-25 show strain peaks sorted from smallest to largest for port and starboard gages in bays 4 and 3 respectively. Peak strains were identified by searching for local maxima in a 300 second test period, with the maxima separated by a minimum of 0.5 seconds and amplitude exceeding the rms value of strain for the test period. Strain peaks at lower levels in Figure 4-24 and Figure 4-25 show the trend expected from static testing: for the bay 4 panels strains are approximately 2-2.5 times greater in the port panel; while in the bay 3 panels, the ratio is 0.6-0.8. However the ratio at the highest strain levels is not as clear. In the case of the bay 3 panels, the maximum strains are higher in the stiffer port panel. This could indicate there was

excessive roll to the port side or that the path into the waves may have increased the severity of slamming on port panels.

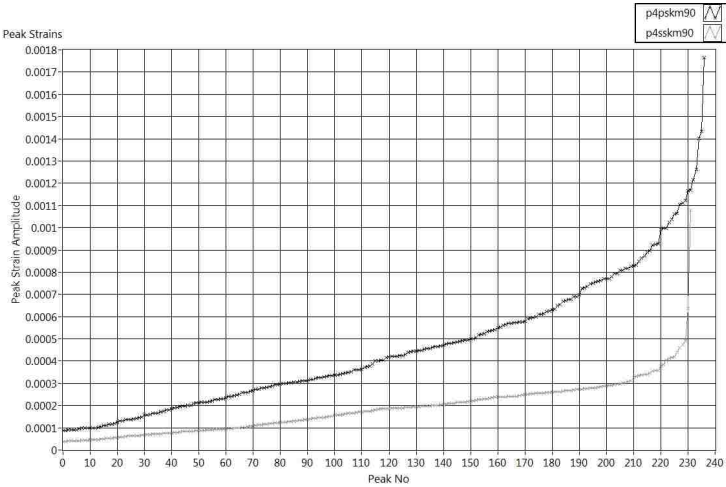


Figure 4-24: Sorted 90 degree peak strains in bay 4 port and starboard panels for a 300 second duration test

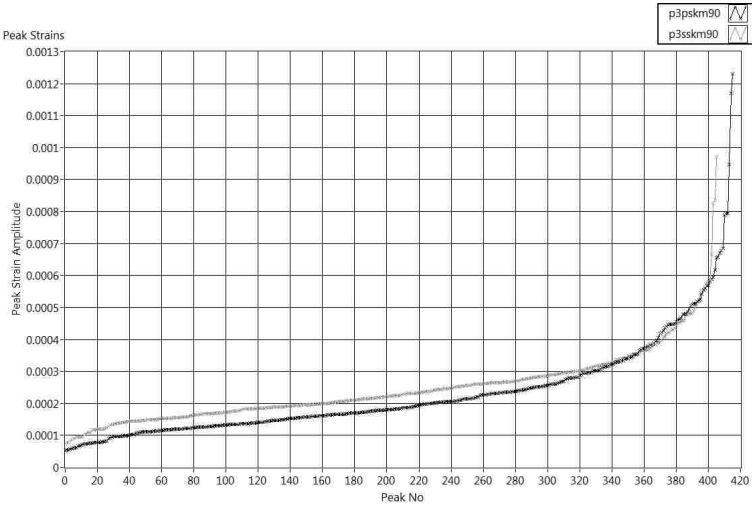


Figure 4-25: Sorted 90 degree peak strains in bay 3 port and starboard panels for a 300 second duration test

The following figures show relationships between strain peaks and forward speed, vertical velocity, and vertical acceleration. In these plots peak strains were identified for the port bay 4 panel as in previous plots, and then corresponding peaks for forward speed, vertical velocity and vertical acceleration were identified. In the case of vertical velocity, the greatest negative rigid body velocity in the 1 second period preceding the strain peak was selected. This value is the maximum “free fall” speed before a slamming impact. In the case of the vertical acceleration, the maximum rigid body vertical acceleration within 0.5 seconds of the peak strain was selected. These time ranges were selected based on observation of numerous slamming events. Figure 4-29 shows an example of strain, acceleration and velocity peaks identified for a typical slamming event.

These strain peak plots suggest that there is no simple correlation between forward speed and panel strain, rigid body acceleration and panel strain or free fall velocity and panel strain. This suggests that the peak strains are more complex to predict and are related to a combination of vertical velocity, forward velocity and factors such as roll angle, wave geometry or other specifics of wave encounters.

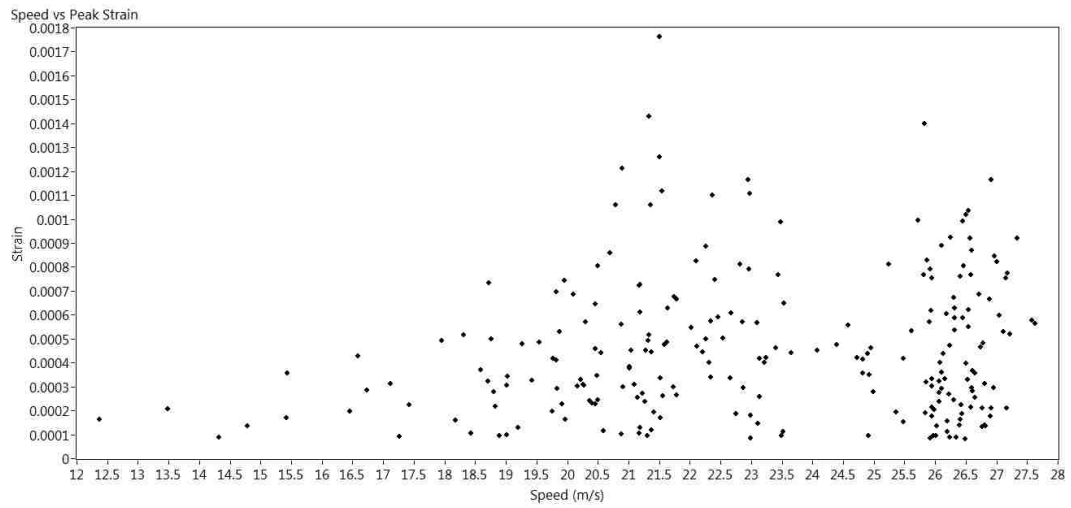


Figure 4-26: Forward speed vs peak 90 degree strain for bay 4 panel

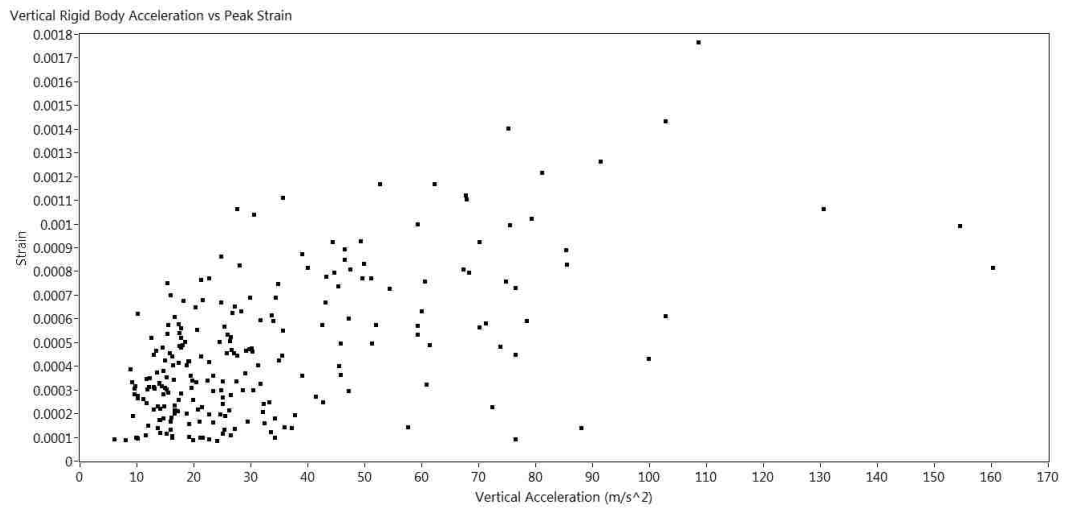


Figure 4-27: Vertical rigid body acceleration vs peak 90 degree strain for bay 4 panel

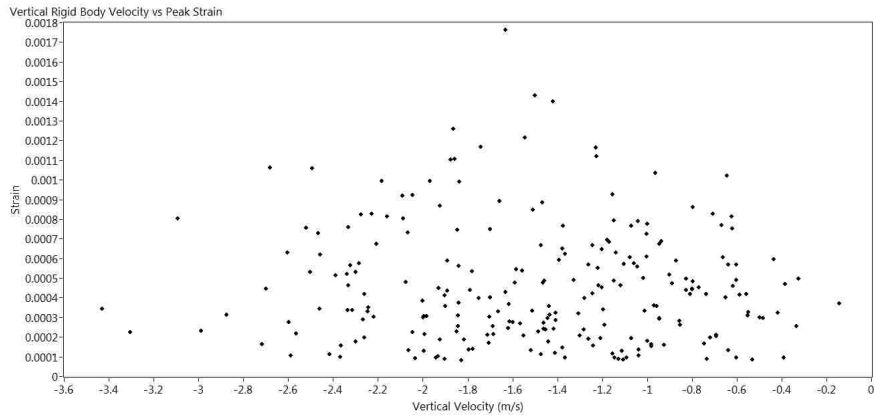


Figure 4-28: Vertical rigid body velocity vs peak 90 degree strain for bay 4 panel

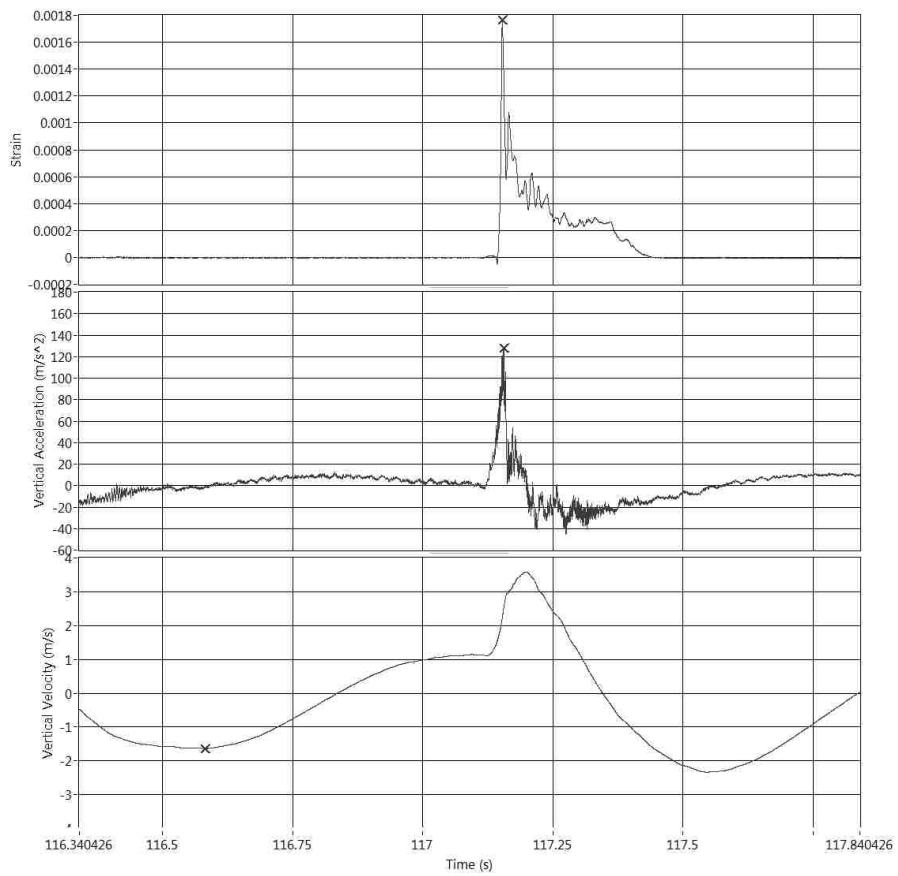


Figure 4-29: Peak strain, rigid body acceleration and rigid body velocity identification

Relative panel response

Histograms demonstrating the strain ratio in the left and right panels are shown in Figure 4-30 for bay 4 and Figure 4-31 for bay 3. These plots express the number of times a specific ratio of port and starboard strain occurred during a 300 second duration test. Strains are from gages oriented transversely in the middle of inner skins of each panel. The histograms indicate that the strain ratios are centered at 1.845:1 in the port panel and 0.565:1 in the starboard panel. Figure 4-32 and Figure 4-23 show these histograms as a function of strain, where a darker color at a point indicates a higher rate of incidence of that combination of strains. The straight lines are references of the ratios from the histograms. At low to moderate strain these ratios do appear to accurately describe the trend. At high strain it is not clear what the relationship is between the port and starboard strains.

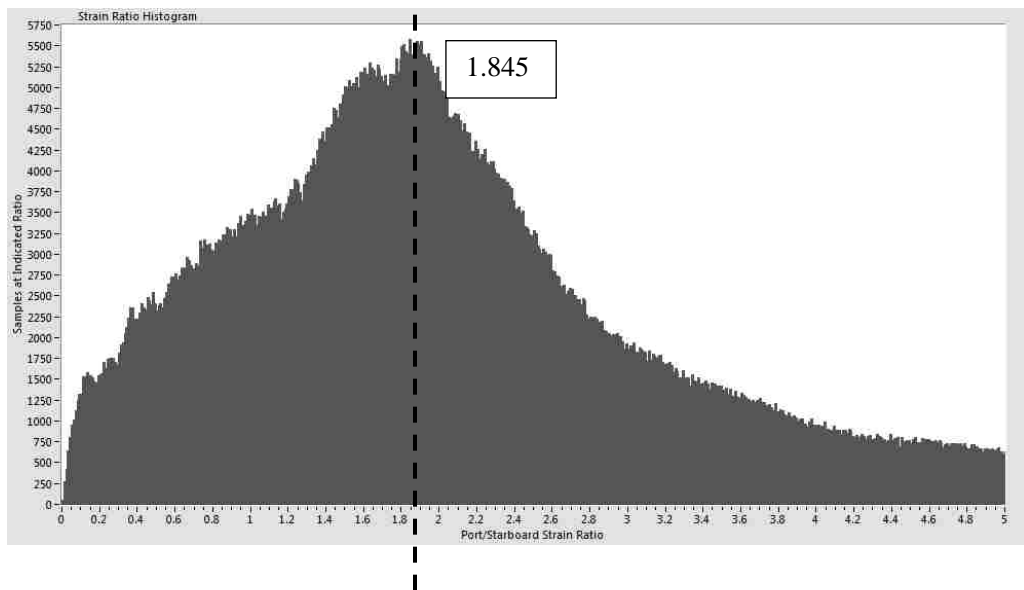


Figure 4-30: Bay 4 port/starboard 90 degree strain ratio histogram

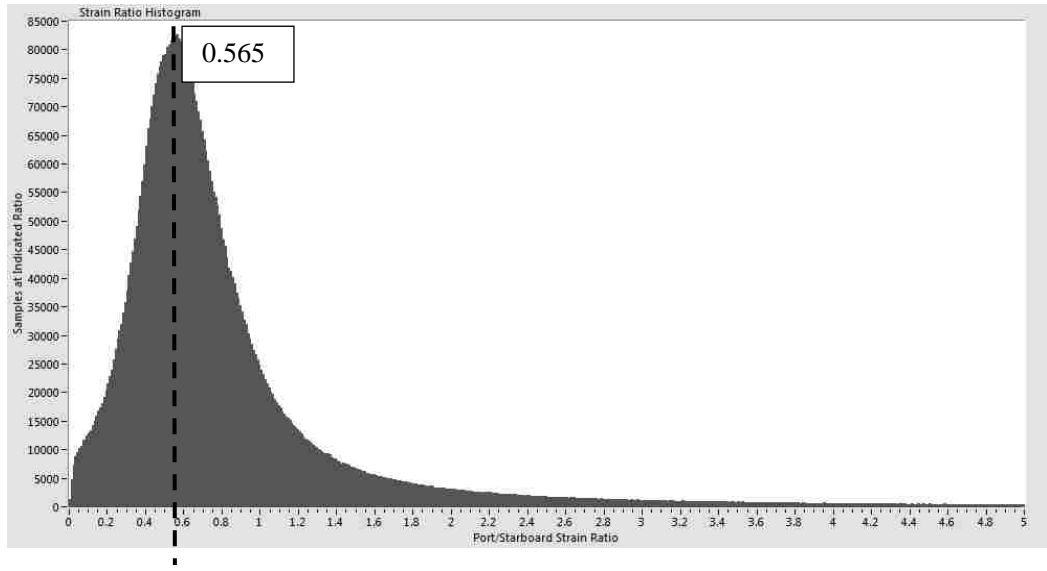


Figure 4-31: Bay 3 port/starboard 90 degree strain ratio histogram

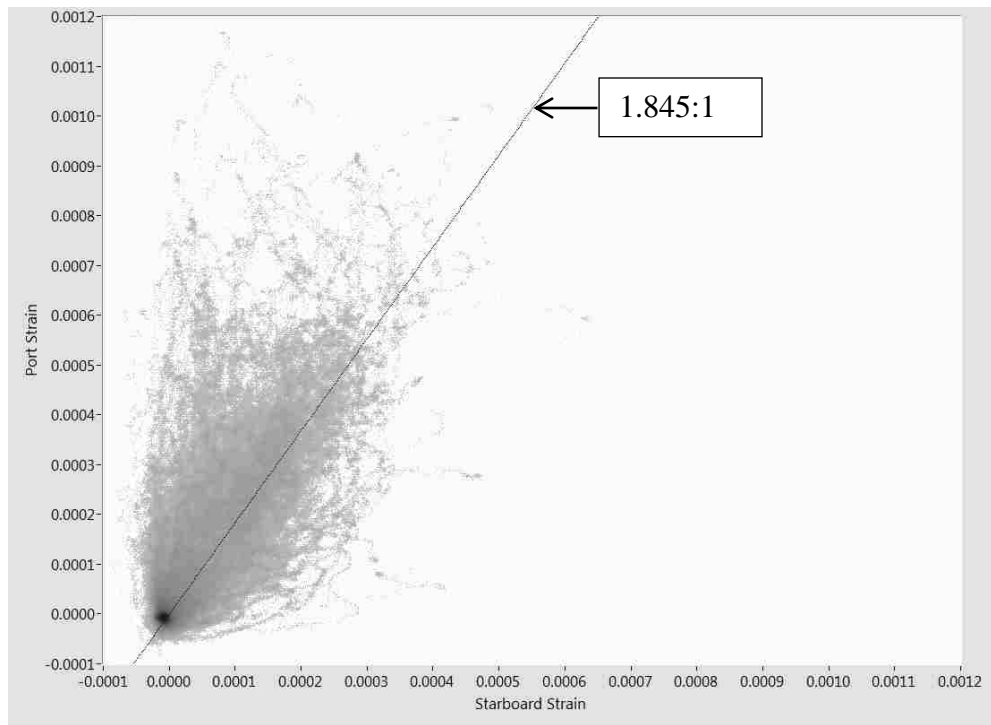


Figure 4-32: Bay 4 Starboard 90 degree strain vs Port 90 degree strain histogram

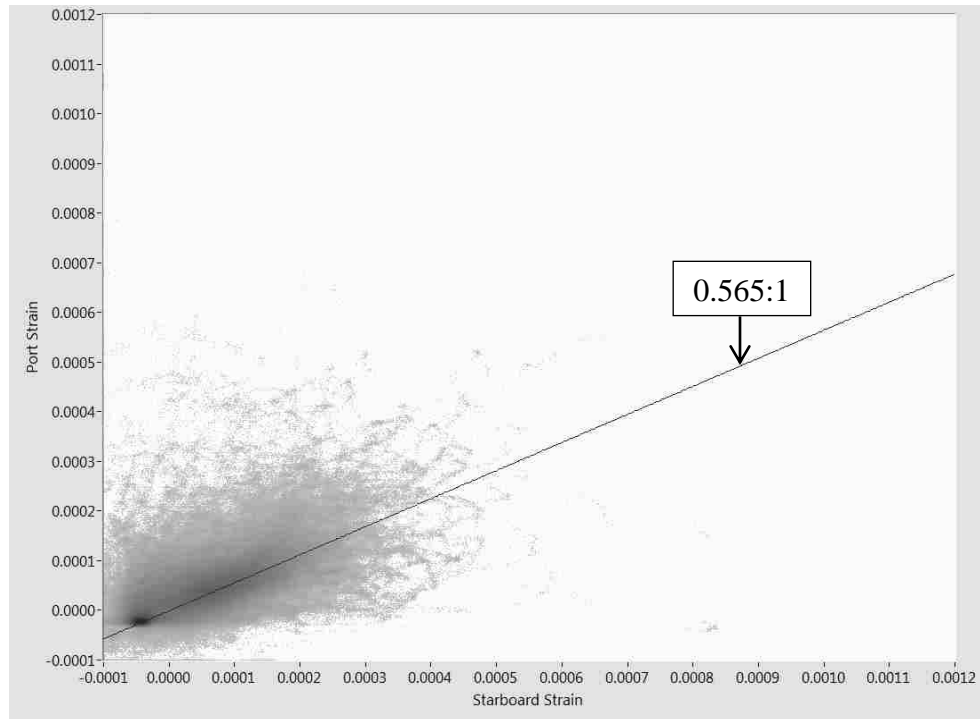


Figure 4-33: Bay 3 Starboard 90 degree strain vs Port 90 degree strain histogram

Panel Response in frequency domain

Fast fourier transforms (FFT) of bay 4 bottom panel 90 degree strains from sea trials are given in Figure 4-34. These are 2 second FFTs averaged over the duration of the 300 second test. The strain magnitude reaches a noise floor at roughly 1 kHz. The engine speed was approximately 4400 rpm for this test, the first three multiples of the engine half speed (37 Hz) are indicated on the plot.

The second set of FFT plots are zoomed in on the frequency range of 100-1000hz, the order of the lowest dry panel eigenfrequencies. The first dry eigenfrequencies are

indicated on this plot. There is no clear correlation between peaks in the panel response FFT and the dry eigenfrequencies.

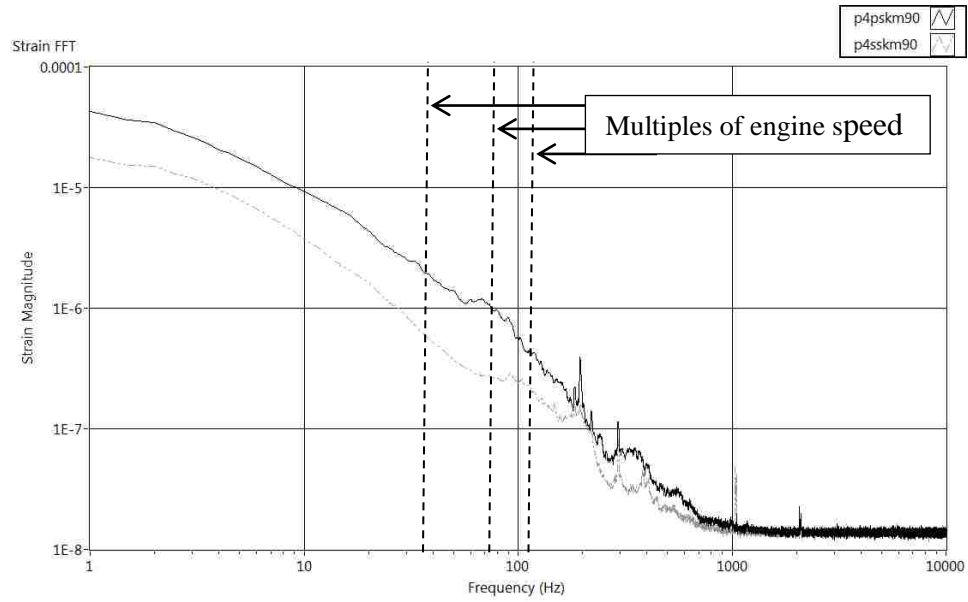


Figure 4-34: Bay 4 90 degree strain FFT

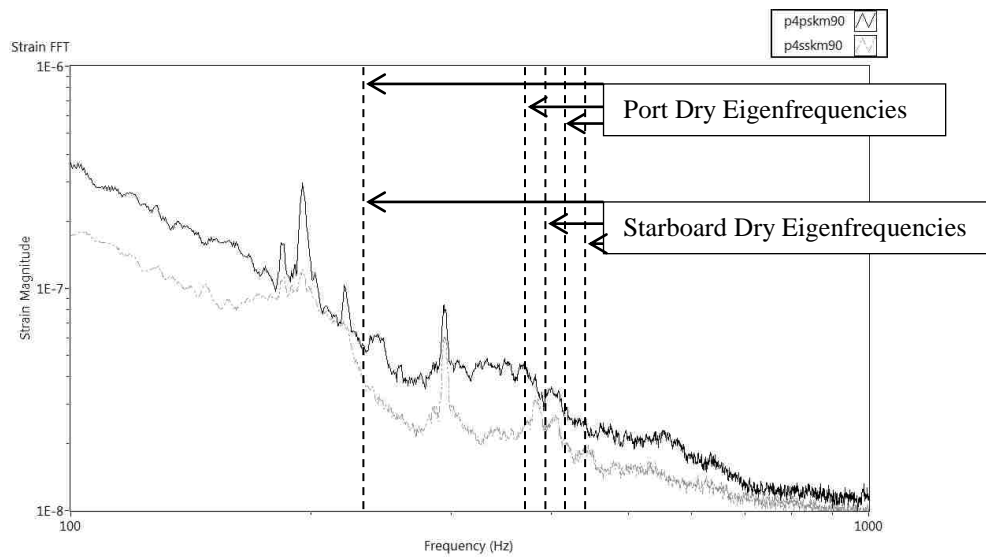


Figure 4-35: Bay 4 90 degree strain FFT 100-1000Hz

Relative panel response in the frequency domain

The Hv frequency quotient relating the strain amplitudes of the starboard and port panels in bay 4 as a function of frequency is shown in Figure 4-36. The coherence estimate for the frequency response functions is shown in Figure 4-37. The FRF was generated from the same 300 second data record as the strain peak charts and histograms. At low frequency the strain ratio in bay 4 is approximately 2. Above 10Hz this ratio increases until 70Hz where it reaches a peak of over 4. However, the coherence plot for this frequency response function indicates that above 10Hz the coherence is very poor. This indicates that there is a coherent linear relationship in strains at low frequency, but at high frequency the behavior is more complex.

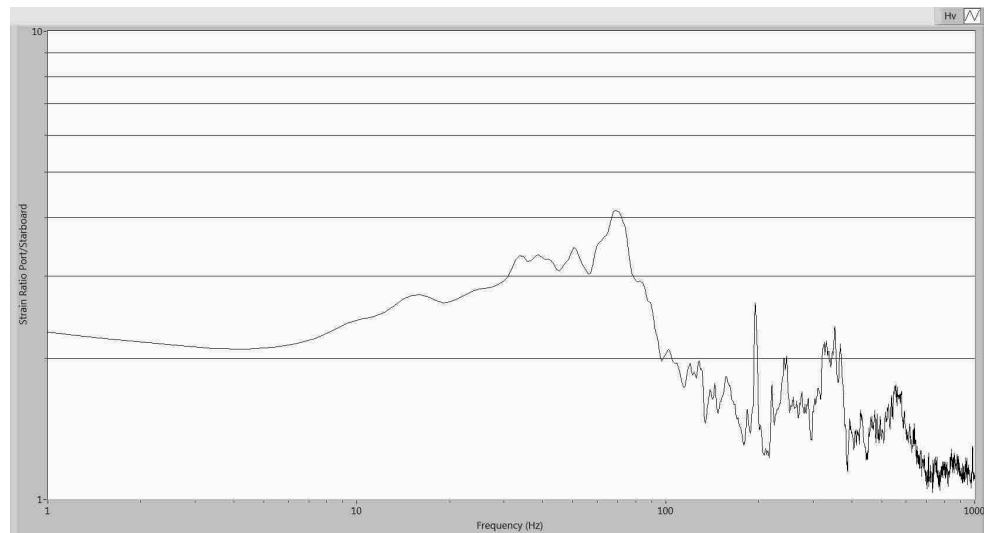


Figure 4-36: Bay 4 Port/Starboard 90 degree strain Hv FRF

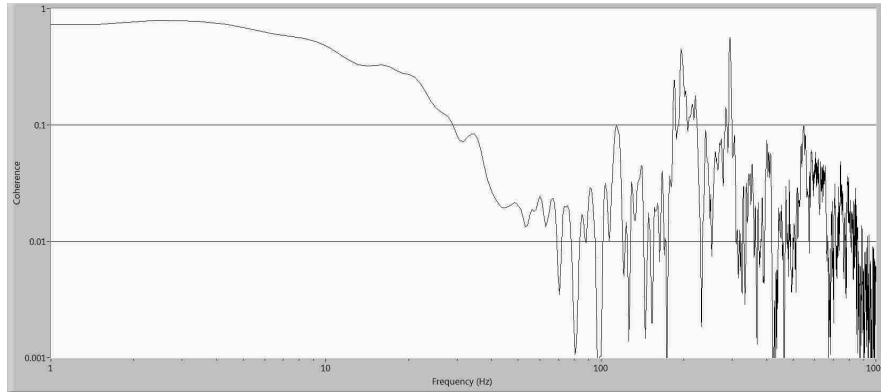


Figure 4-37: Bay 4 Port/Starboard 90 degree strain FRF coherence

The H1 and H2 FRFs serve as upper and lower bounds of the true response and when plotted give a visual indication of the range of the frequency response function. Figure 4-38 shows the H1 and H2 functions plotted for the bay 4 panels. As the coherence function suggests, at low frequency the FRF is a good estimate, while at high frequency the H1 and H2 approximations diverge.

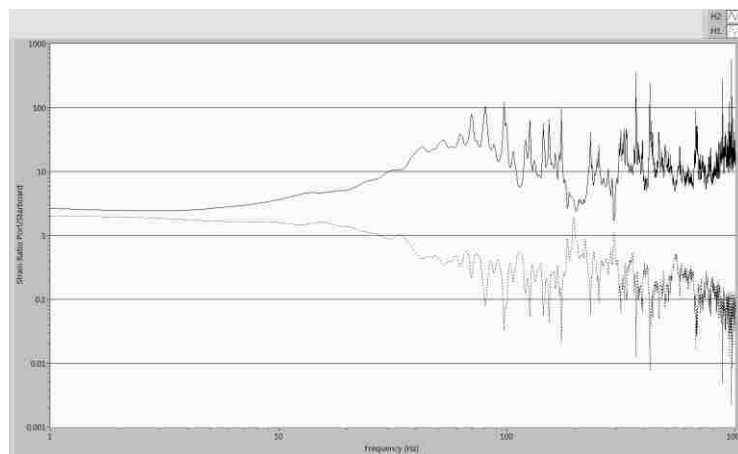


Figure 4-38: Bay 4 Port/Starboard 90 degree strain H1 and H2 FRF showing estimated upper and lower FRF bounds

One potential cause of the poor coherence demonstrated is non-stationarity. A non-stationary deterministic system is a system that would be periodic under periodic conditions but is non periodic when conditions are random. During slamming, panel excitation and the coupling of water mass with panels are time varying conditions that influence panel motion. Two traditional measures of stationarity are mean and variance. The plots below show the mean and variance of the bay 4 port strain signal for a 1 second time window as a function of time.

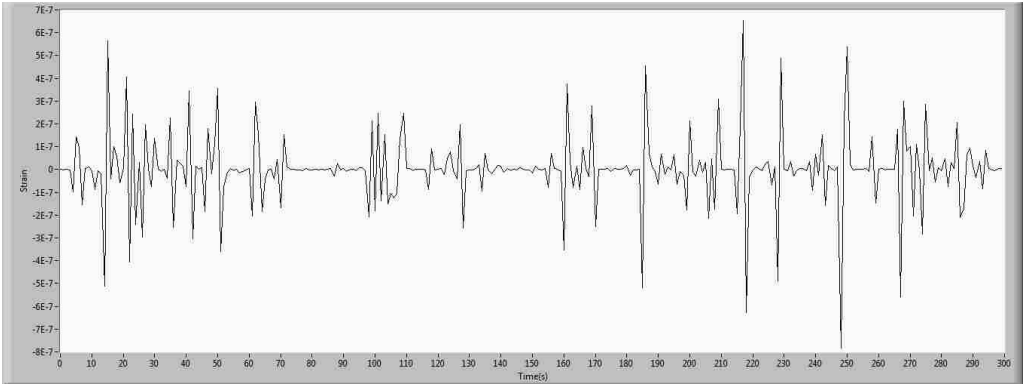


Figure 4-39: Bay 4 port mean 90 degree strain (1s window) vs time

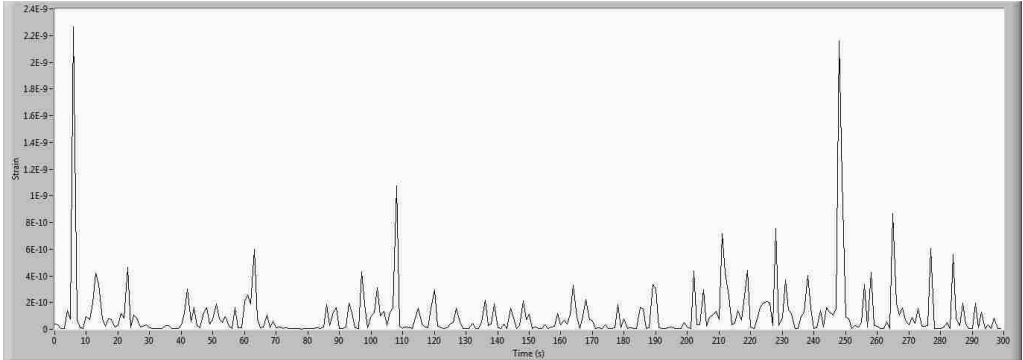


Figure 4-40: Bay 4 port 90 degree strain variance (1s window) vs time

The mean and variance plots show significant non-stationarity. As a result, a method is needed to quantify the change in spectrum with time. The short time fast fourier transform (STFFT) is one such method.

Accelerometer Spectrographs

Figure 4-41 and Figure 4-42 show short time Fast Fourier Transforms for accelerometers mounted on the port and starboard bay 4 panels during a 1 second time period. The rigid body component of the acceleration was removed by subtracting the acceleration measured at the transverse bulkhead just ahead of the panel accelerometer. A 0.2 second blackman window was incremented at 0.010 second steps through the time period during which a single slamming event occurs. This slam occurred when the boat was at a neutral roll angle. The forward speed was 22.2 m/s and peak vertical rigid body velocity prior to the impact was -2.7 m/s.

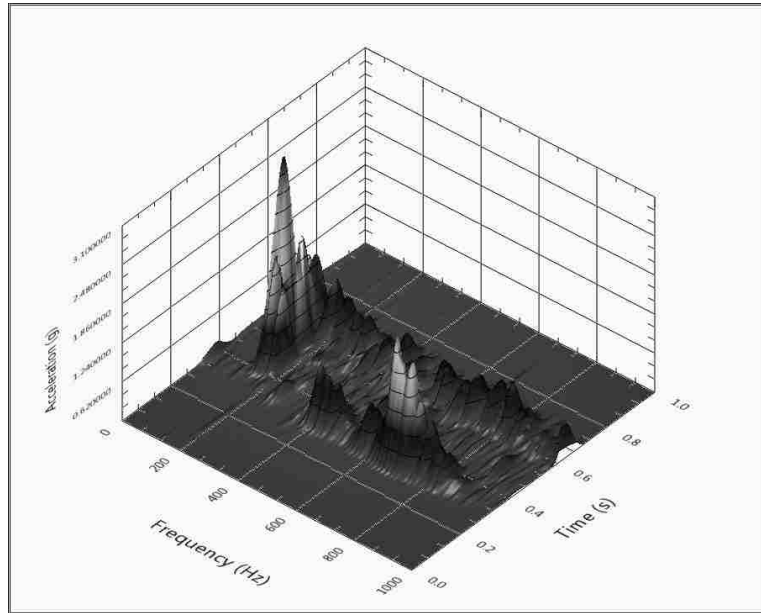


Figure 4-41: Bay 4 port panel mounted accelerometer STFFT

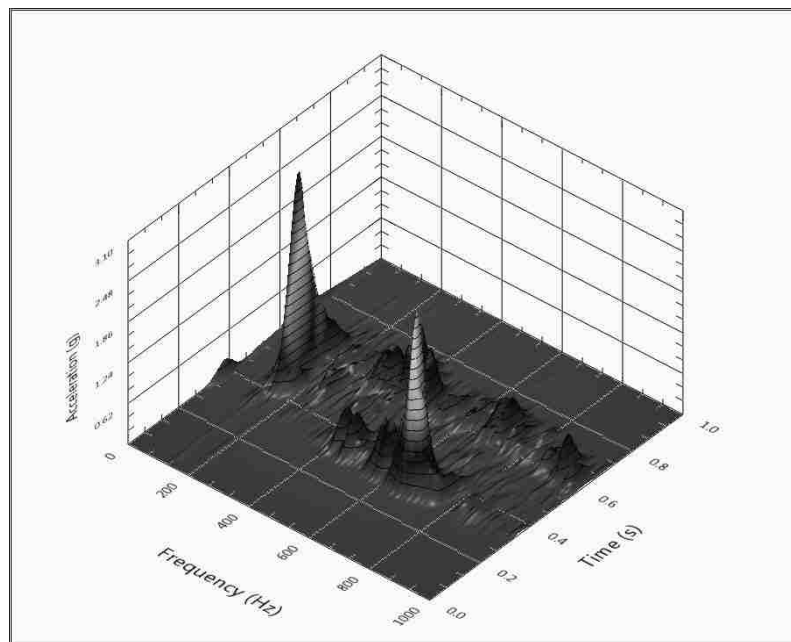


Figure 4-42: Bay 4 starboard panel mounted accelerometer STFFT

These spectrographs show some important features of the panel response during slamming. In the initial phase, several peaks can be seen between 350 and 700 Hz. In both the port and starboard panels these peaks cover the range of the first five dry eigenfrequencies. The largest component for both panels is at approximately 650 Hz, the mode with two transverse bending waves. This initial dry vibration phase is very short. This phase is followed by a longer duration phase composed primarily of lower frequency vibration. In the port panel, the primary component is 130 Hz and in the starboard panel 145 Hz. Toward the end of this phase, higher frequency vibrations begin to re-appear. Note that due to the tradeoffs in temporal resolution and frequency resolution in the short time FFT, the use of a 0.2s window results in a frequency resolution of only 5 Hz. The use of a longer window would improve resolution of frequency components, but obscure the time varying nature of the spectrum.

Figure 4-43 and Figure 4-44 show the short time FFT of 90 degree strains on the inner panel skins for the same slamming event with the use of the same 0.2s Blackman window. These figures are dominated by a low frequency component. Figure 4-45 and Figure 4-46 show the same short time FFT for the 50-1000 Hz range. These plots show the vibration at 130-145 Hz is present in the strain as well.

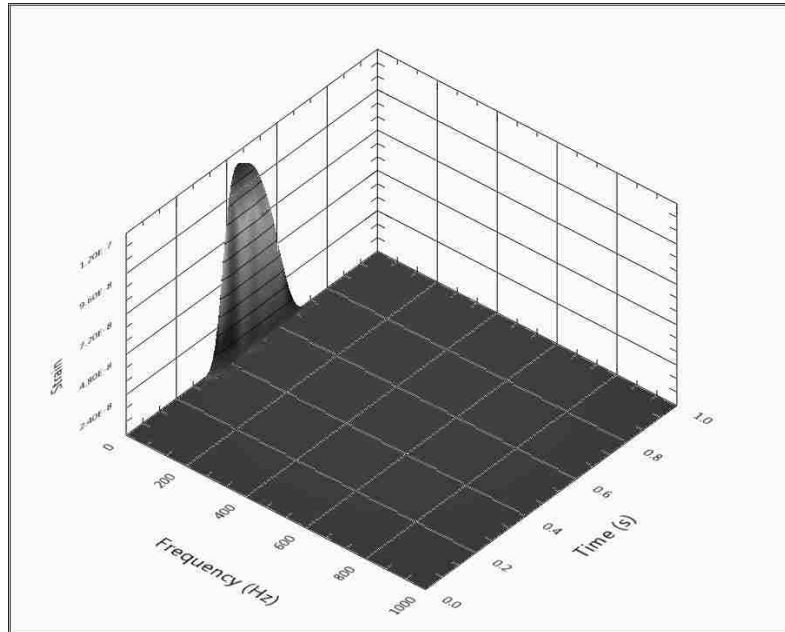


Figure 4-43: Bay 4 Port 90 degree strain STFFT

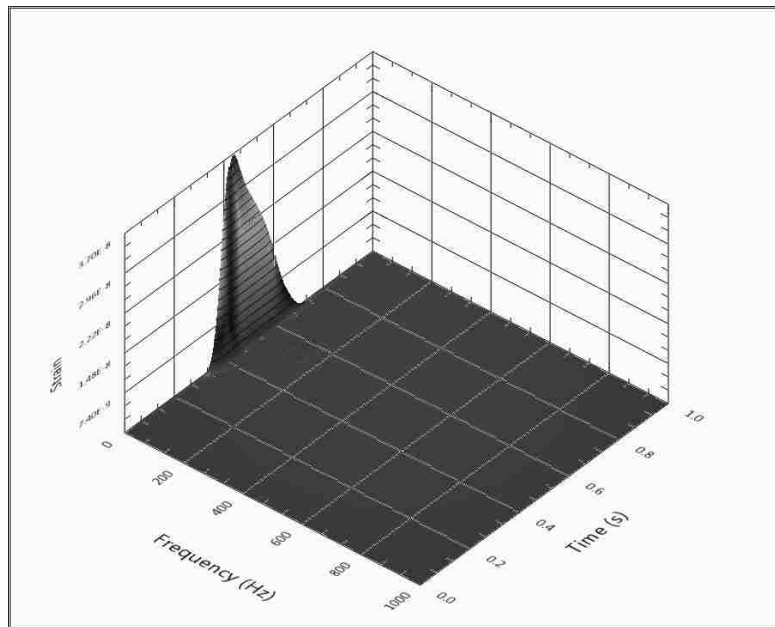


Figure 4-44: Bay 4 Starboard 90 degree strain STFFT

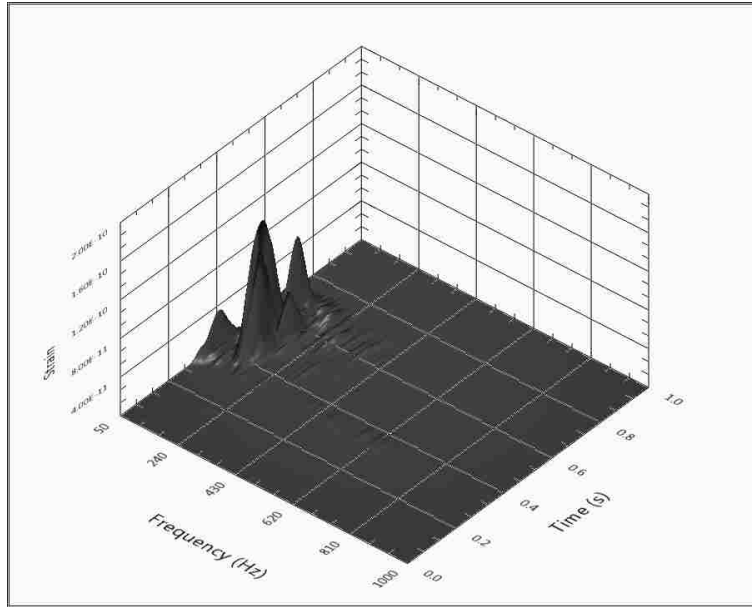


Figure 4-45: Bay 4 Port 90 degree strain short time FFT > 50Hz

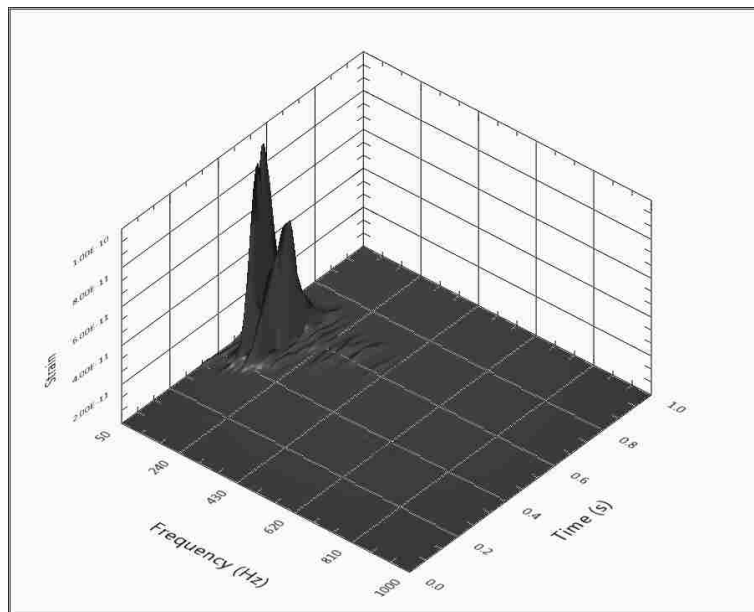


Figure 4-46: Bay 4 Starboard 90 degree strain short time FFT >50 Hz

The strain time histories in Figure 4-47 and Figure 4-48 show the large magnitude low frequency strain component of ~ 1.5 Hz as well as a smaller magnitude oscillation of ~ 125 Hz.

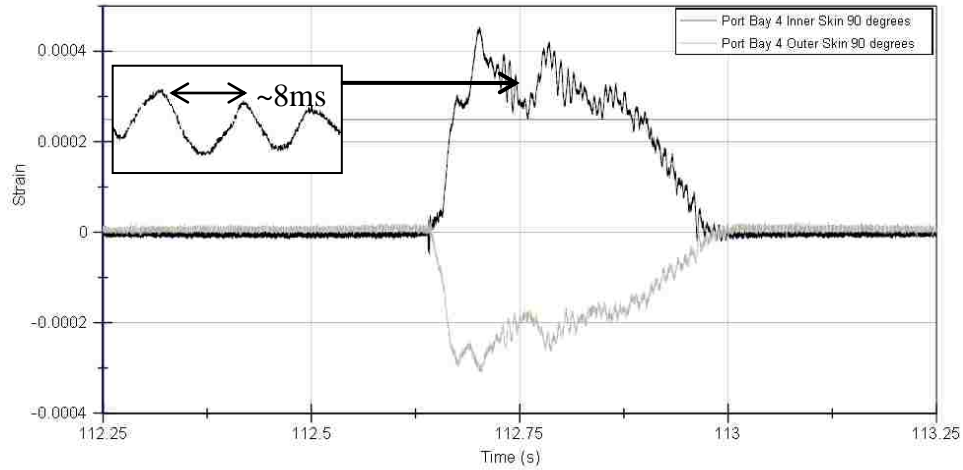


Figure 4-47: Bay 4 Port 90 degree strain time history

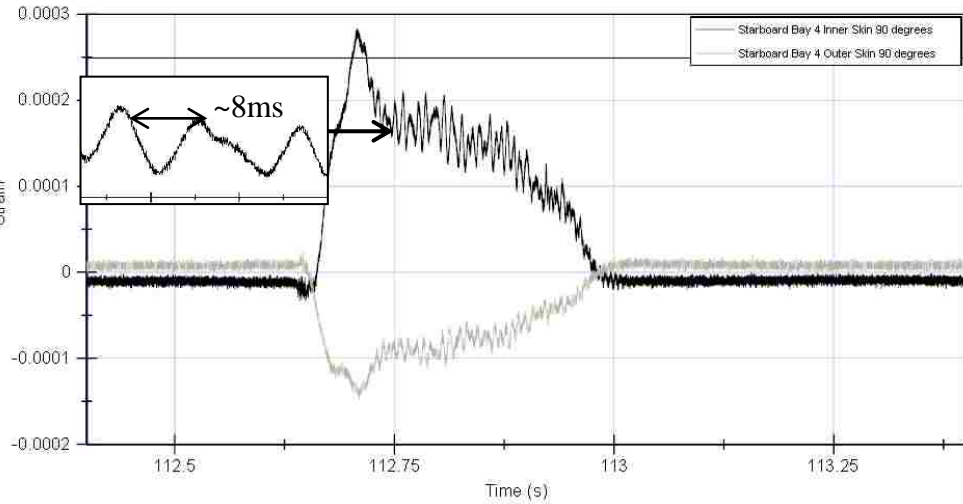


Figure 4-48: Bay 4 Starboard 90 degree strain time history

The accelerometer STFFT and strain time histories for the bay 4 port panel subject to a second slamming event are shown in Figure 4-49 and Figure 4-50. In this slamming event, the boat is at an extreme roll angle of 23 degrees to the port side, resulting in a near zero effective deadrise angle on the port bay 4 panel. The slam occurred while the boat was travelling at 22.8 m/s and the peak vertical velocity prior to the impact was -2.2 m/s. A comparison of the front camera view at the previously presented neutral roll slam and this high roll slam is shown in Figure 4-51. The STFFT shows brief excitation of the lowest dry panel modes followed by lower frequency vibration, primarily at approximately 80 Hz.

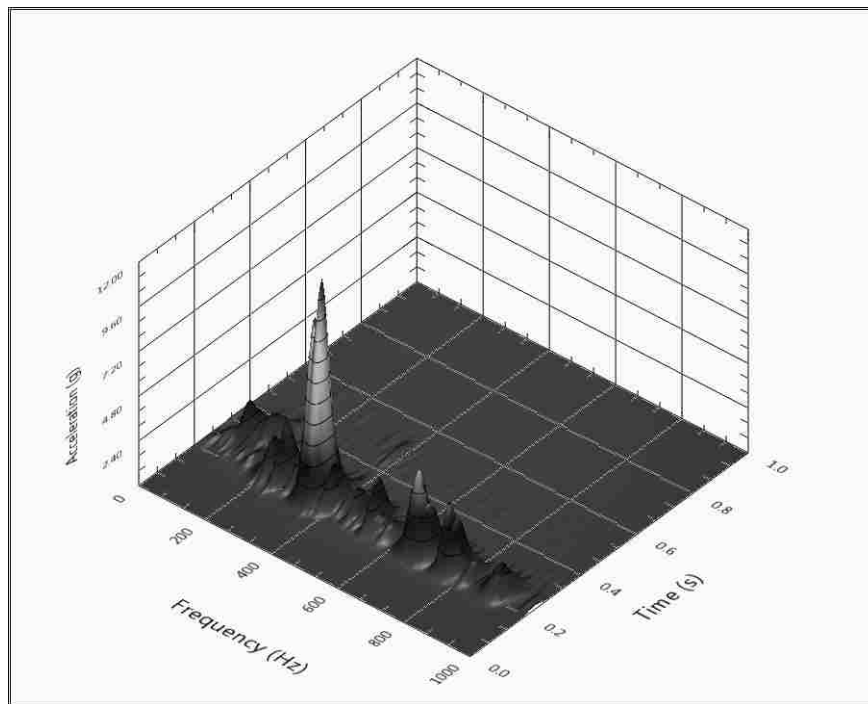


Figure 4-49: High Roll Angle Slam Port Bay 4 Panel Acceleration

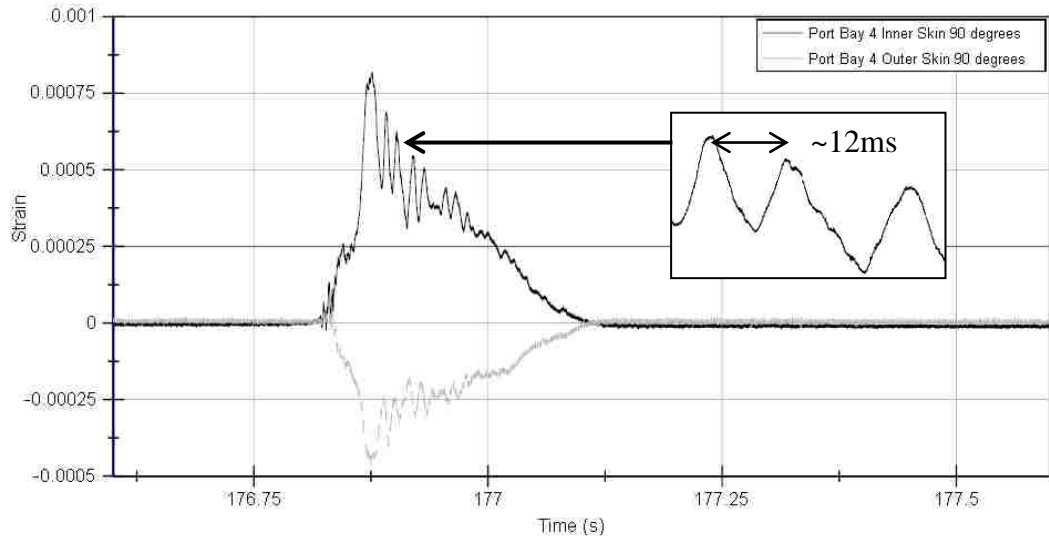


Figure 4-50: High Roll Angle Slam Port Bay 4 Strain Time History



Figure 4-51: Neutral and High Roll Slamming Event Comparison

Table 4-3 **Error! Reference source not found.** gives a comparison of the vibration frequencies observed in the port bay 4 panel under the neutral and high roll slams and the wet eigenfrequencies predicted by the methods from Lv and Stenius. The panel was assumed to be fully submerged for the Lv estimate ($k=1$) and the deadrise angle was

calculated for both zero and the local deadrise angle $\beta = 28^\circ$. The dynamic hydroelastic parameter R was calculated for the two slamming events and is given in Table 4-4. For these calculations it is unclear what the relevant impact velocity is for calculation of the hydroelastic dynamic parameter. In Battley eg, the vertical velocity of the SSTS is used, but for the test of a real vessel forward velocity is a factor as well. The hydroelastic dynamic parameter has been calculated using just the vertical component as well as the total velocity magnitude. These may in some sense serve as upper and lower bounds of this parameter.

Table 4-3: Comparison of Observed and Calculated Panel Vibration Frequencies for Bay 4 Port Panel



	Frequency (Hz)
Neutral Roll Slam	130
High Roll Slam	80
Lv Wet Frequency (k=1)	90
Stenius Wet Frequency 	65
Stenius Wet Frequency 	73

Table 4-4: Hydroelastic Dynamic Parameter

	R (Vertical velocity)	R (Total rigid body velocity)
Neutral Roll Slam	6.6	0.80
High Roll Slam	8.1	0.78

The high roll slam case results in panel vibration frequency on the order of the wetted natural frequency predicted by both Lv and Stenius for a fully submerged panel. The neutral roll slam case results in a higher frequency perhaps due to incomplete submersion of the panel. The hydroelastic dynamic parameter indicates that hydroelastic effects are significant for both the high roll and neutral roll slam if the impact velocity is taken as total rigid body velocity. However, if only the vertical component is considered the impact would be considered quasi static by this metric.

4.8 Conclusion

Operation of the Slamming Load Test Facility has resulted in the collection of a wealth of slamming data. Subject to low to moderate slamming loads the strain response in the bottom panels have reflected the static behavior of the panels: a panel twice as stiff will have half the strain. However at the highest slamming loads, the relationship is less clear. The conditions that result in the highest peak strains do not have an obvious direct correlation to the vessel's speed, roll angle or vertical velocity. Future tests will see the addition of displacement and pressure transducers that, together with cameras

directed toward oncoming waves will aid in identifying the key parameters that lead to the highest strain slamming.

Efforts to characterize the frequency domain response of the panels highlight the non-stationary nature of panel response. An investigation into two specific slamming events using short time Fourier transforms shows that factors such as roll angle can change the frequency response of the panels, potentially as a result of the variation in water mass-panel coupling. The high roll angle event in which the panel is assumed to be fully submerged shows a vibratory frequency similar to the “wetted natural frequencies” predicted by Stenius et al and Lv and Grenestedt. The neutral roll angle event in which the degree of panel submersion is not known resulted in a higher frequency vibration, but still below the lowest dry eigenfrequency. The characteristic loading rate for the observed slamming impacts may or may not be in the region where significant hydroelastic effects are expected, depending on how the impact velocity is calculated.

The simultaneous need for localization in both time and frequency demanded by a non-stationary process like slamming necessitates an improvement on the short time Fourier transform. Future work will investigate the use of wavelet analysis methods to more precisely characterize the evolution of the strain and acceleration frequency spectra during the highly dynamic slamming events.

4.9 Acknowledgement

Funding for developing and testing the slamming load facility was provided by ONR (awards N00014-08-1-0203, N00014-08-1-0227, N00014-08-1-0228, N000141-01-07-6-7). The program monitor, Dr. Roshdy Barsoum, is gratefully acknowledged for his support.

Chapter 5. Conclusions and Future Work

This dissertation work has focused on the important slamming phenomenon in high-speed craft and ocean engineering. In this final chapter, we summarize our research work and briefly describe some areas that merit future research.

5.1 Contributions of the Dissertation

Slamming loads are important in the structural design of all high-speed crafts. The structural engineer often wants a design pressure from the hydrodynamicist. When the problem is strongly hydroelastic, this has no physical meaning. One can, of course, define an equivalent pressure load that causes the same maximum strain in the structure. This may be convenient, but it is artificial. The equivalent pressure load would be an order of magnitude smaller than the maximum physical pressure. Since many physical effects will occur during slamming, the hydrodynamicist may analyze problems on a time scale that is irrelevant for maximum structural response. The problem must be analyzed analytically from a structural point of view. The first two Chapters of this dissertation attempt to shed some light on this complex V-shaped bottom slamming problem from a structural point of view. By analytically studying a simplified model of a bottom panel subjected to a non-uniform pressure distribution traveling at various speeds across the bottom, bottom panel deflections and bending moments due to water slamming during both the initial structural inertia phase and the subsequent free vibration phase were calculated. Important conclusions were drawn from the work done

in first two chapters. The lowest natural frequency of the bottom panel plays a key role in the structural response. If the time it takes for the slamming load to traverse the bottom panel is near the period of the lowest eigenfrequency, then the structural response (deflection, bending moment) is large. It indicates that it may be possible to tailor bottom panels to avoid large deflections and bending moments. The maximum structural responses occur during the slamming load initial phase when the slamming load travelling speed is under a certain speed in the neighborhood of the first characteristic speed. At higher speeds of the load, the maximum occurs during the vibration phase. And a large peak pressure does not necessarily mean large stresses in the structure and very large pressure peaks of a traveling slamming load may be too concentrated in space and time to have a considerable influence on the maximum bending stresses.

In order to investigate the response of bottom panels to real slamming conditions, a Slamming Load Test Facility, Numerette, was developed. The hull was designed using a steel / composite hybrid concept. The truss was made of stainless steel and closed out with composite sandwich panels. The panel manufacturing process is challenging. As previously mentioned, the boat consists of 50 composite panels, including 10 bottom panels, 10 side panels, 7 deck panels, 19 bulkhead panels and 4 hatches. All composite panels were made by 5-axis CNC routing of foam cores, and vacuum infusing vinyl ester resin into glass or carbon fiber skins onto foam cores. The unique bottom sandwich panels with embedded strain gages were designed and manufactured also. After all composite panels were bonded to the steel truss and the cockpit installation

was finished, the main hull structure of the steel/composite hybrid slamming test boat was accomplished. Accordingly, the creative concept of steel/composite hybrid hull structure was realized with inventive boat building method.

In Chapter 4, experimental tests of the steel/composite hybrid boat have been performed to evaluate the structural design of the steel/composite hybrid hull concept, as well as to investigate the response of bottom structures of high speed craft under slamming loads. The hybrid structural integrity was maintained after well over 30 hours of running in a variety of sea conditions. The functions of all onboard equipment were verified. No damage or plastic deformation was found. Therefore, the feasibility of this new concept of building high-speed crafts with hybrid ship structures was confirmed.

The collected data during sea trials was synchronized and organized in a proper manner. By analyzing the data, typical strain and acceleration signals of bottom panels under real slamming loads were identified. And the bottom panel static stiffness tests were performed. The relative stiffness of the bottom panels was determined by tests. It makes the future analysis on the effects of panel stiffness on slamming responses of bottom panels possible.

5.2 Future Work

The analytical investigations will be verified against experimentally measured responses of bottom panels under real slamming loads. More advanced and

comprehensive data analyses both in time domain and in frequency domain are underway. Due to the randomness of slamming events in sea trials, the data will be analyzed statistically. More data acquisition devices will be installed on Lehigh's Slamming Load Test Facility, including pressure transducers, wave shape detectors, etc. High speed / high accuracy measurements will be made on water pressures, strains in the two skins of the bottom sandwich panels, and panel deflections. Deflections will be measured by installing high speed LVDT's and supporting lightweight stiff truss structures. The measured data will be compared with the results from the analytical model.

Appendix

Appendix A

Fourier sine integral transformation

Equation NO.	Original $f(x)$	Transform $F(j)$
A1	$\frac{d^4 f(x)}{dx^4} \text{ for}$ $f(0) = f(L) = f''(0) = f''(L) = 0$	$\frac{j^4 \pi^4}{L^4} F(j)$
A2	$\sum_{i=1}^n a_i f_i(x)$	$\sum_{i=1}^n a_i F_i(j)$
A3	$b[1 - H(x - a)]$	$\frac{bL}{j\pi} \left(1 - \cos \frac{j\pi a}{L} \right)$
A4	$\delta(x - a)$	$\sin \frac{j\pi a}{L}$

Appendix B

Laplace-Carson integral transformation

Equation NO.	Original $f(t)$	Transform $F(s)$
B1	$\frac{d^2 f(t)}{dt^2}$	$s^2 F(s) - s^2 f(0_+) - s \frac{df(0_+)}{dt}$
B2	$\sum_{i=1}^n a_i f_i(t)$	$\sum_{i=1}^n a_i F_i(s)$
B3	$1 - \cos at$	$\frac{a^2}{s^2 + a^2}$
B4	$\frac{1}{a^2 b^2} \left[1 + \frac{1}{a^2 - b^2} (b^2 \cos at - a^2 \cos bt) \right]$	$\frac{1}{(s^2 + a^2)(s^2 + b^2)}$
B5	$\frac{1}{a} \sin at$	$\frac{s}{s^2 + a^2}$

Appendix C

The dynamic moment is normalized by the maximum static moment. The maximum static moment within the beam depends on where the (slamming) load is applied. Introduce the distance a such that the right end of the load q_1 in Figure 1-1 is located at $x=a$. In the dynamic case $a=ct$. The maximum static bending moment cannot occur for $a < l_1$ since additional load will increase the maximum moment. For $a > l_1$ the bending moment in a beam that is statically loaded as in Figure 1-1 is

$$M = \begin{cases} -\frac{q_2 x^2}{2} + \frac{(l_1^2 q_1 - 2al_1 q_1 + 2Ll_1 q_1 - a^2 q_2 + 2al_1 q_2 - l_1^2 q_2 + 2Laq_2 - 2Ll_1 q_2)x}{2L}, & 0 < x \leq a - l_1 \\ -\frac{q_1 x^2}{2} + \frac{(l_1^2 q_1 - 2al_1 q_1 + 2Laq_1 - a^2 q_2 + 2al_1 q_2 - l_1^2 q_2)x}{2L} - \frac{(a - l_1)^2 (q_1 - q_2)}{2}, & a - l_1 < x \leq a \\ \frac{(l_1^2 q_1 - 2al_1 q_1 - a^2 q_2 + 2al_1 q_2 - l_1^2 q_2)x}{2L} - \frac{(l_1^2 q_1 - 2al_1 q_1 - a^2 q_2 + 2al_1 q_2 - l_1^2 q_2)}{2}, & a < x \leq L \end{cases}$$

The maximum moment can occur either when $a=l_1$, when $a=L$, or when $l_1 < a < L$. In either case, since $M(0)=M(L)=0$ and M and its slope are continuous, the maximum moment will be found where $dM/dx=0$. The three different cases are:

Case 1, $a=l_1$

$$M^1 = \begin{cases} -\frac{q_1 x^2}{2} + \frac{(2Ll_1 - l_1^2)q_1 x}{2L}, & 0 < x < l_1 \\ -\frac{l_1^2 q_1 x}{2L} + \frac{l_1^2 q_1}{2}, & l_1 < x < L \end{cases}$$

The maximum moment for this case is

$$M_{\max}^1 = \frac{l_1^2(2L-l_1)^2 q_1}{8L^2}$$

Case 2, $l_1 < a < L$

The maximum will be in the range $0 < x < a$ since for $x > a$ the derivative dM/dx is never zero. The maximum moment will be found in the range $x < a - l_1$ if

$$l_1 < \bar{l}_1 \equiv \frac{aq_1 - Lq_1 - aq_2 + \sqrt{a^2 q_1^2 - 2aLq_1^2 + L^2 q_1^2 - a^2 q_1 q_2 + 2aLq_1 q_2}}{q_1 - q_2}$$

and otherwise in the range $a - l_1 < x < a$. The maximum moment is

$$M_{\max}^2 = \begin{cases} \frac{(-l_1(l_1 + 2L)(q_1 - q_2) + a^2 q_2 + 2a(l_1(q_1 - q_2) - Lq_2))^2}{8L^2 q_2} & \text{if } l_1 < \bar{l}_1 \\ \frac{(2al_1 q_1 - l_1^2 q_1 + a^2 q_2 - 2al_1 q_2 + l_1^2 q_2)(2al_1 q_1 - l_1^2 q_1 - 4aLq_1 + 4L^2 q_1 + a^2 q_2 - 2al_1 q_2 + l_1^2 q_2)}{8L^2 q_1} & \text{if } l_1 > \bar{l}_1 \end{cases}$$

Case 3, $a=L$

The moment is

$$M^3 = \begin{cases} -\frac{q_2 x^2}{2} + \frac{(l_1^2 q_1 - l_1^2 q_2 + L^2 q_2)x}{2L}, & 0 \leq x \leq L - l_1 \\ -\frac{q_1 x^2}{2} + \frac{(l_1^2 q_1 - 2Ll_1 q_1 + 2L^2 q_1 - L^2 q_2 + 2Ll_1 q_2 - l_1^2 q_2)x}{2L} - \frac{(L - l_1)^2 (q_1 - q_2)}{2}, & L - l_1 < x \leq L \end{cases}$$

The maximum moment will be found where $dM/dx=0$, which is in the range $x < L - l_1$ if

$$l_1 < \frac{L}{\sqrt{q_1/q_2} + 1}$$

and otherwise in the range $x > L - l_1$. The maximum moment is

$$M_{\max}^3 = \begin{cases} \frac{(l_1^2(q_1 - q_2) + L^2 q_2)^2}{8L^2 q_2} & \text{if } 0 < l_1 < \frac{L}{\sqrt{q_1/q_2} + 1} \\ \frac{((2Ll_1 - l_1^2)(q_1 - q_2) + L^2 q_2)^2}{8L^2 q_1} & \text{if } L > l_1 > \frac{L}{\sqrt{q_1/q_2} + 1} \end{cases}$$

Total

The maximum moment is the maximum of M^1 , M^2 , and M^3 ,

$$M_{ms} = \max[M_{\max}^1, M_{\max}^2, M_{\max}^3]$$

Appendix D

Least Squares complex Exponential method

A set of H_2 receptance frequency response functions can be generated from the force excitation $y(t)$ and displacement response $x(t)$.

$$H_{21}(\omega) = \frac{S_{xx}(\omega)}{S_{yy}(\omega)}$$

Where the autospectral density $S_{xx}(\omega)$ is defined as

$$S_{xx}(\omega) = \lim_{T \rightarrow \infty} \frac{1}{T} \int_{-T/2}^{T/2} x(t) x^*(t - \tau) e^{-j\omega\tau} d\tau$$

And the autocorrelation $R_{xx}(\tau)$ is

$$R_{xx}(\tau) = \lim_{T \rightarrow \infty} \frac{1}{T} \int_{-T/2}^{T/2 - \tau} x(t) x(t - \tau) dt$$

The cross spectral density $S_{xy}(\omega)$ is

$$H_{xy}(\omega) = \int_{-\infty}^{\infty} H_{xy}(t) e^{-j\omega t} dt$$

Where the cross correlation $H_{xy}(t)$ is

$$H_{xy}(t) = \lim_{T \rightarrow \infty} \frac{1}{T} \int_{-T/2}^{T/2} x(\tau) y(t - \tau) d\tau$$

The complex exponential method used assumes the receptance FRF or displacement at a point j due to a force at point k for a linear, viscous damped N degree of freedom system in the frequency domain can be represented as:

$$H_{jk}(\omega) = \sum_{r=1}^N \frac{A_{jk}^r}{\omega_r^2 + j(\omega - \omega_r^*) \zeta_r} \frac{A_{jk}^{r*}}{\omega_r^2 + j(\omega - \omega_r) \zeta_r}$$

where ω_r is natural frequency, ζ_r viscous damping factor and A_{jk}^r is the residue corresponding to each mode r and $*$ denotes complex conjugate. Alternatively:

$$H_{jk}(\omega) = \sum_{r=1}^N \frac{A_{jk}^r}{\omega_r^2 + j(\omega - \omega_r^*) \zeta_r}$$

where

$$X(\omega) = \sum_{n=0}^{L-1} x(n) e^{-j\omega n}$$

$$X(\omega) = \sum_{n=0}^{L-1} x(n) e^{-j\omega n}$$

$$X(\omega) = \sum_{n=0}^{L-1} x(n) e^{-j\omega n}$$

The impulse response function (IRF) is calculated from the inverse Fourier transform.

$$x(n) = \frac{1}{2\pi} \int_{-\pi}^{\pi} X(\omega) e^{j\omega n} d\omega$$

or

$$x(n) = \frac{1}{2\pi} \int_{-\pi}^{\pi} X(\omega) e^{j\omega n} d\omega$$

where $X(\omega) = \sum_{n=0}^{L-1} x(n) e^{-j\omega n}$

The time response at L time intervals n is thus

$$H_{11}(z) = \hat{h}(0) = \sum_{k=0}^{\infty} \hat{h}_k z^{-k}$$

$$H_{11}(z) = \hat{h}(0) = \sum_{k=0}^{\infty} \hat{h}_k z^{-k}$$

$$H_{11}(z) = \hat{h}(0) = \sum_{k=0}^{\infty} \hat{h}_k z^{-k}$$

Where $V_r = e^{S_r \Delta t}$

With the time domain impulse IRF $h(t)$ known from the inverse Fourier transform of the experimental H_2 receptance function, Prony's method can be used to solve for roots V_r . This allows calculation of the natural frequencies, damping factors, and ultimately residues. Modal constants and phase angles are derived from the residues. The method can be used with multiple IRF's to extend it to a global process.

Appendix E

STFT

The Fourier transform is most useful for understanding the global characteristics of a signal, averaged over all time. For a time varying signal $f(t)$, the time dependence of the signal is integrated out of the Fourier transform. The result $\hat{f}(s)$ reflects global frequency content.

$$\int_{-\infty}^{\infty} f(t) e^{-j2\pi st} dt = (f, e^{-j2\pi st})$$

Where the complex exponential $e^{-j2\pi st}$

If the frequency content localized in time is of interest a different approach is necessary. One such approach is the short time Fourier transform. This approach makes use of a window, or a function of mean square norm 1 that is concentrated in the locale of the time of interest. In this case, the windowed complex exponential is localized both at time t_0 and frequency s_0 and is given by:

$$e^{-j2\pi s(t-t_0)} w(t-t_0) = e^{-j2\pi s_0(t-t_0)} e^{-j2\pi (s-s_0)(t-t_0)} w(t-t_0)$$

Where the window $w_{\tau}(t) = w(t - \tau)$

The short time Fourier transform is thus given by as:

$$STFT_{\omega, \tau}(f(t)) = \int_{-\infty}^{\infty} f(t) w_{\tau}(t) e^{-j\omega t} dt$$

Bibliography

- [1] Odd M. Faltinsen, Hydroelastic slamming, *J. Mar. Sci. Tech.*, 5(2) (2000) 49-65.
- [2] Lewis, R.R., Sarkani, S., & Beach, J.E., A structural system-response approach for statistically estimating wave impact design pressures. ASNE Day 2006, Arlington, Virginia, 2006
- [3] Yamamoto, Y., Iida, K., Fukasawa, T., Murakami, T., Arai, M., Ando, A. Structural damage analysis of a fast ship due to bow flare slamming. *Int. Shipbuild. Progr.* 32, 124-136 (1985)
- [4] Greenhow, M., Lin, W., Non-linear Free Surface Effects: Experiments and Theory, Report No. 83-19, Dept. Ocean Engn., Cambridge, Mass: Mass. Inst. Technol. 1983
- [5] Battley, M., Allen, T., Pehrson, P., Stenius, I., Rosen, A., Effects of panel stiffness on slamming responses of composite hull panels, 17th International Conference on Composite Materials, Edinburgh International Convention Centre (EICC), Edinburgh, UK (2009).
- [6] Peseux, B., Gornet, L., Donguy, B., Hydrodynamic impact: Numerical and experimental investigations, *Journal of Fluids and Structures* 21, 277-303 (2005).
- [7] Battley, M., Allen, T., Servo-hydraulic system for controlled velocity water impact of marine sandwich panels, *Experimental Mechanics* 52, 95-106 (2012).
- [8] Portemont, G., Deletombe, E., Drazetic, P., Assessment of basic experimental impact simulations for coupled fluid/structure interactions modeling, *International journal of crash worthiness* Vol.9 No.4, 333-339 (2004).
- [9] Von Karman, The impact on seaplane floats during landing, Technical report 321,NACA, (1929).
- [10] Wagner H, Uber stoss und gleitvorgänge an der oberfläche von flüssigkeiten, *ZAMM* 12 (1932) 193-215.
- [11] Dobrovol'skaya, Z. N., On some problems of similarity flow of fluid with a free surface, *J. Fluid Mech.*, vol. 36, 805-929 (1969).
- [12] Zhao R., Odd M. Faltinsen, Water entry of two-dimensional bodies, *J. Fluid. Mech.* 246 (1993) 593-612.

- [13] Odd M. Faltinsen, Water entry of a wedge by hydroelastic orthotropic plate theory, *J. Ship Res.*, 43 (1999) 180-193.
- [14] Odd M. Faltinsen, *Hydrodynamics of High-Speed Marine Vehicles*, Cambridge University Press, New York, 2005, pp.308-309.
- [15] Mei X., Lui Y., Yue D. K. P., On the water impact of general two-dimensional sections, *Appl. Ocean Res.*, 21 (1999) 1-15.
- [16] Lu, C. H., He, Y. S., Wu, G. X., Coupled analysis of nonlinear interaction between fluid and structure during impact, *Journal of Fluids and Structures*, 14 (2000) 127-146.
- [17] Odd M. Faltinsen, The effect of hydroelasticity on ship slamming, *Phil. Trans. R. Soc. A.*, 355 (1997) 1-17.
- [18] Jan Kvalsvold, Odd M. Faltinsen, Hydroelastic modeling of wet deck slamming on multihull vessels, *Journal of Ship Research*, Vol. 39, No.3 (1995) 225-239
- [19] Det Norske Veritas (DNV), Rules for High Speed, Light Craft and Naval Surface Craft, Pt.3 Ch.1 Sec.2 pp. 14, July 2012.
- [20] American Bureau of Shipping (ABS), Rules for Building and Classing High-Speed Craft, Pt. 3 Ch.2 Sec.2 pp. 57, 2013.
- [21] Germanischer Lloyd (GL), Rules & Guidelines, I-Pt.3 Ch.1 pp. 3-17, 2012.
- [22] L. Fryba, *Vibration of Solids and Structures under Moving Loads*, 3rd edition, Telford, 1999.
- [23] Anders Rosen, Karl Garne, Jakob Kutenkeuler, Full-scale design evaluation of the Visby class corvette, Ninth International Conference on Fast Sea Transportation, Fast2007, Shanghai, China September 2007, 583-588
- [24] Mouritz AP, Gellert E, Burchill P, Challis K. Review of advanced composite structures for naval ships and submarines. *Composite Structures* 2001; 53(1): 21-41.
- [25] Barsoum R. The best of both worlds: hybrid ship hulls use composites and steel, *AMPTIAC Quarterly* 2003; 7(3):55-61
- [26] Barsoum R., Hybrid ship hull. US Patent 6, 386 1313; 14 May, 2002
- [27] Thompson, L., Walls, J., Caccese, V., Design and analysis of a hybrid composite/metal structural system for underwater lifting bodies, Project Report for the

Modular Advanced Composite Hull form (MACH) Technology Project. Report No. UM-MACH-RPT-01-08 (2005)

[28] Jun Cao, Joachim L. Grenestedt. Test of a redesigned glass-fiber reinforced vinyl ester to steel joint for use between a naval GRP superstructure and a steel hull, *Composite Structures* 60 (2003):439-445

[29] Cao J, Grenestedt JL. Design and testing of joints for composite sandwich/steel hybrid ship hulls, *Composites Part A* 35(2004): 1091-1105.

[30] Joachim L. Grenestedt, Jun Cao. Ship Hull Consisting of Vierendeel type Steel truss and composite panels, *Proc. Tenth International Conference on Marine Application of Composite Materials (MACM)*, Melbourne, FL, USA, 2004.

[31] Cao J, Grenestedt JL, Maroun WJ., Testing and Analysis of a 6-m Steel Truss/Composite Skin Hybrid Ship Hull Model. *Marine Structures* 19 (2006):23-32.

[32] Cao J., Grenestedt JL, Maroun WJ., Steel Truss/Composite Skin Hybrid Ship Hull, Part I: Design and Analysis. *Composites Part A*, 38(2007): 1755-1762.

[33] Maroun WJ, Cao J., Grenestedt JL., Steel truss/composite skin hybrid ship hull. Part II: Manufacturing and sagging testing, *Composites Part A*, 38(2007): 1763-1772.

[34] Grenestedt, J.L., Reany, J., Wrinkling of Corrugated Skin Sandwich Panels, *Composites Part A: Applied Science and Manufacturing*, Vol. 38, Iss. 2, 2007, pp. 576-589.

[35] Grenestedt JL, Cao J., Maroun WJ., Test of Extensively Damaged Hybrid Ship Hull, *Journal of Marine Science and Technology*, 13:1(2008): 63-70.

[36] Jack Reany, Corrugated skin composite sandwich panels, Ph. D. thesis, Dep. of Mechanical Engineering and Mechanics, Lehigh University, 2008

[37] Andrew Truxel, Composite sandwich panels, Ph. D. thesis, Dep. of Mechanical Engineering and Mechanics, Lehigh University, 2009

[38] Robert Thodal, Instrumentation and data acquisition system for slamming load test facility, M.sc. thesis, Dep. of Mechanical Engineering and Mechanics, Lehigh University, 2010

[39] Scott Shirey, Manufacturing of steel hybrid hull for slamming load test facility, M.sc. thesis, Dep. of Mechanical Engineering and Mechanics, Lehigh University, 2009

- [40] I. Stenius, A. Rosen, M. Battley, T. Allen, Experimental hydroelastic characterization of slamming loaded marine panels, *Ocean Engineering*, 74 (2013) 1-15
- [41] Jian Ly, Joachim L. Grenestedt, Some analytical results for the initial phase of bottom slamming, *Maine Structures* 34(2013) 88-104
- [42] G. K. Kapsenberg, Slamming of ships: where are we now?, *Phil. Trans. R. Soc. A* 369 (2011) 2892–2919.
- [43] Kvalsvold, J., Faltinsen, O.M., Slamming loads on wetdecks of multihull vessels. In *Proc. 1st Int. Conf. on Fast Sea Transportation (FAST)*, Sydney, 21-23 July 1997
- [44] Tveitnes, T., Fairlie-Clarke, A. C., Varyani, K., An experimental investigation into the constant velocity water entry of wedge-shaped sections. *Ocean Engineering*, 35 (2008) 1463–1478
- [45] De Backer, G., Vantorre, M., Beels, C., de Pre, J., Victor, S., de Rouck, J., Blommaert, C., Van Paepegem, W., Experimental investigation of water impact on axisymmetric bodies, *Appl. Ocean Res.* 31 (2009) 143-156
- [46] Battley, Mark, and Susan Lake, Designing composite structures for slamming loads, *2nd High Performance Yacht Design Conference*, Auckland, New Zealand. 177-84. 2006
- [47] Battley, Mark A., and Susan E. Lake, Dynamic performance of sandwich core materials, *16th International Conference on Composite Materials*, Kyoto, Japan. 1-10. 2008
- [48] Battley, Mark, Tom Allen, Jason Schierlink, Susan Lake, and Peter Pehrson, Hydroelastic behaviour of slam loaded composite hull panels, *3rd High Performance Yacht Design Conference*, Auckland, New Zealand. 37-46. 2008
- [49] Stenius, I., A. Rosen, M. Battley, T. Allen, and P. Pehrson, Hydroelastic effects in slamming loaded panels, *11th International Conference on Fast Sea Transportation*. Honolulu, Hawaii, USA. 644-52. 2011

Vita

Jian Lv was born on January 9, 1979 in Xining, Qinghai Province, China to his parents, Xian-Hui Lv and Pei-Hong Wang. In 1980 the family moved to Chongqing where Jian Lv attended primary school, middle school and high school. In September of 1998, Jian began his studies at Fudan University in Shanghai. He graduated in June 2002 with a Bachelor of Science Degree in Engineering Mechanics and was awarded with the honor of Excellent Undergraduate Student of Fudan University. He continued his studies as a recommended student for immediate admission to Graduate School of China Academy of Engineering Physics in September 2002 and graduated with a Master of Science Degree in Solid Mechanics in May 2005. After that, Jian worked as an engineer in China Academy of Engineering Physics. In January 2009, he started pursuing his PhD at Lehigh University in Mechanical Engineering while working as a research assistant in the Lehigh Composites Lab headed by Dr. Joachim L. Grenestedt.